A simulation study of the formation of tetrahedral inorganic and hybrid glasses

Wenlin Chen

Department of Physics

Aberystwyth University

This dissertation is submitted for the degree of

Doctor of Philosophy

May 2017

ACKNOWLEDGEMENTS

I would like to express my sincere gratitude to both my supervisor Edwin Flikkema and Prof. Neville Greaves for the continuous support of my Ph.D study and related research, for their patience, motivation, and immense knowledge. In particular, I would like to thank Edwin for his support on Chapter 2 and Prof. Neville's guidance on Chapter 4 and 5. Besides my advisor, I would like to thank Charles Lelosq from the Australian National University for his support and modelling for Chapter 3. Without their helps, the thesis could not have been successfully conducted.

I would also like to thank my family: my parents and to my brother for supporting me spiritually throughout writing this thesis and my life in general.

ABSTRACT

With modern high performance calculation, computer simulation provides us with a possible way to analyse and visualize the atoms and molecules of materials within nanometre scale and picoseconds which can not be simply achieved in real-life experiments. Therefore it is a great tool to study the nano-structure formation of materials including crystals as well as glasses.

In this thesis, alumino-silicates including nepheline and its compositional variations have been studied. Melts of them have been simulated and glasses have been derived by melt-quenching procedures. Static structures and dynamic properties have been studied. Specifically, the distribution of mobile metallic ions, which fundamentally affects the properties of glasses, has been simulated in this study to give a better understanding of the roles mobile ions play. In particular, we are interested in whether micro-segregation of metallic ions occurs as it does in silicates [1]. Molecular dynamics simulations of alumino-silicates nepheline ($K_X Na_{4-X} Al_4 Si_4 O_{16}$) have been performed to obtain first the structure of molten nepheline. Five different alkali ratios have been taken to explore the effect of ionic radius and field strength on segregation. Radial Distribution functions, REDOR second moments, Vibrational Densities of States and molecular structure snapshots reveal how alkali ions distribute non-randomly, form channels in between the framework atoms of both molten and glassy nepheline. This nanostructure of nepheline at Tg=1200K is virtually the same as the quenched structure at room temperature, confirmed by the snapshots. When K^+ replaces Na^+ in the system, it occupies more volume. Both melt viscosity and boson peak intensity in quenched glass showed dramatic increasing due to the percolation channels affected by K^+ concentration.

To replicate the dynamics properties of melts, three series of molecular dynamics simulations with varied alumino-silicate composition, each containing different ratios of Al/Si, have been performed including nepheline for which Al/Si = 1. Mean square displacements have been calculated from trajectories at 2000K to derive diffusion constant. The Einstein-Stokes equation and the Eyring equation were then used to derive the viscosity and compared. The Eyring results show a better replication of a fitted Adam-Gibbs model with measured viscosity values.

Contrasting to the melt-quenched glasses of nepheline, hybrid inorganic-organic glasses produced by pressure induced amorphization (PIA) of Zeolitic Imidazolate Frameworks (ZIFs) have also been simulated. ZIF8 is a porous hybrid material that is considered stable at ambient condition. However, under pressure the crystalline structure collapses and eventually glasses are formed. Molecular dynamics has been performed to obtain the crystalline structure as well as a low density amorphous (LDA) structure at 1.2 GPa. However, it is established that classical MD is insufficient for deriving structure beyond 1.2 GPa due to the restriction of bonding potential.

Instead, DFT calculation was performed at pressures ranging from 1 atm to 4 GPa. Molecular dynamics based on DFT revealed that while the volume decreases monotonically during compression, the compressibility does not. In fact, two phase transitions were observed. The first transition occurs between the crystal structure and the low density amorphous phase (LDA) at 1.2 GPa where the crystalline topology is retained. This is followed by a transition to a high density amorphous phase (HDA) at 2.4 GPa, where the ring topology of the crystal and LDA is completely lost. To confirm the phase transition, volume and compressibility versus pressure have been calculated and discussed. Radial distribution function, coordination number and vibrational density of states together with MD snapshots are analysed for understanding the structure and dynamics of each phase. Additionally, decompression simulations support the contention that these phase transitions are reversible. In particular, both LDA is restored from HDA and ZIF8 crystal is restored from LDA.

Finally, the pressure-induced amorphization of pure silica sodalite (SOD) has been studied. Crystalline structure of pure silica sodalite usually belongs to Im3m phase group which is highly incompressible. But in this study, evidence from angle distribution and compressibility suggest that the starting structure for the simulations belongs to a considerably compressible I43m space group. This is possibly due to an iso-symmetric transition that occurs near ambient pressure. Sharing similar β-cage topology with ZIF8, two phase transitions were also observed in the compression of SOD, qualitatively similar to what has been observed for ZIF8. They are SOD to LDA and LDA to HDA phase transitions. Further simulation of decompression reveals that these transition are reversible similar to ZIF8. However, because SOD has far greater rigidity than ZIF8, both phase transitions take place at considerably higher pressures (9.5 GPa and 12.5 GPa). Coordination number, compressibility, radial distribution function and vibrational density of states are used to demonstrate the structures and dynamics in each phase.

The two themes of melt-quenching and amorphization under pressure confirm the versatility of Molecular Dynamics modelling new structure and dynamic processes which are often precluded from experimental methods.

TABLE OF CONTENTS

CHAPTER 1

INTRODUCTION

Simulations, which usually are performed on computers, have become increasingly important in material science due to the possibility of modelling massive system with higher complexity brought by development of calculation facilities and improved simulation methods. Being able to probe the materials at an atomic level, the simulation provides us an immersed way to study the microscopic structures of materials and their relation to properties.

In this first chapter, crystal and glass, being two major states of condensed matter, are going to be introduced and discussed to provide a background for the thesis. In particular, three materials, alumino-silicates including nepheline, zeolitic imidazolite frameworks (ZIFs) and pure silica sodalite (SOD), all having huge potential in producing glasses, are going to be studied. Melt-quenching glasses from the simplest silicate glasses to alumino-silicate glasses with multi-cation, which relate to minerals like nepheline are going to be discussed. Besides, pressure induced amorphization of ZIF8 and pure silica sodalite (SOD) are also going to be investigated.

1.1 Crystal

Crystals, solids with ordered periodic arrangements of atoms or ions, which have been exploited and studied by mankind for thousands of years, is one of the fundamental subjects in Condensed Matter and Material Science. In nature, most of solids appear to be crystalline or polycrystalline. Examples of large crystals including sodium salt, snowflakes and quartz. In general, crystals are well known for their well defined geometrical shape. One of the great example is the snow flake which represents the ice crystal (figure 1.2).

Having amazing variety, crystals can be very distinctive in properties like hardness, density or transparency. Besides, each crystal can have an unique atomic structure. Atoms in the crystal are arranged in a highly ordered way, forming a periodic crystal

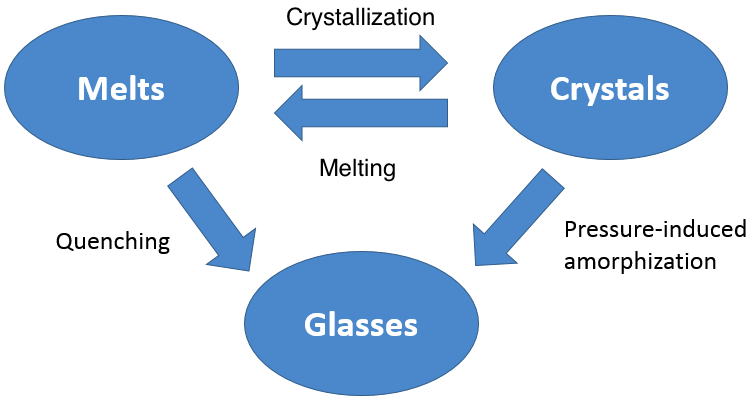

Fig. 1.1 Relations between the melts, crystals and glasses. The transferring process can be reversible in some condition.

Fig. 1.2 Snowflake is either a single ice crystal or an aggregation of ice crystals.[2]

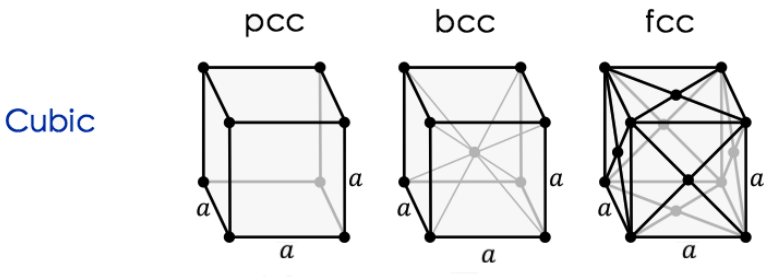

Fig. 1.3 Bravais lattice of cubic system.[3]

lattice in three dimensions. The minimum repeating unit of such periodic structure can be located in 14 Bravais lattices. An example of Bravais lattices are shown below as figure 1.3. In particular these relate to the crystallographic structures from which simulations have been performed.

Crystalline materials have a huge range of applications. Because of the geometrical shapes and appealing lustre, lots of crystals have been used in decoration including diamond. On the other hand, diamonds have been widely used for making drill coatings due to their superior hardness. Some of the crystal are extremely rare, considering the fact that obtaining a pure crystal from nature can be very difficult. Moreover, modern industry and science are not satisfied by just exploiting natural crystals. Because of the demand for purity of crystal, the natural exploitation has its own limitation. With developed technologies, the obstacles of obtaining many pure crystals have been largely overcome. In fact, crystals can be synthesised for higher purity than they could ever appear in nature. Those pure crystals, especially pure Silicon, have been widely used in the revolution of the communications industry such as making chips and LEDs.

1.1.1 Feldspar and nepheline

Making up 60% of the Earth's crust, feldspars are one of the most abundant rock forming minerals. They are framework alumino-silicates with a considerably wide range of chemical composition. They can be classified by the percentages of substitutional ions inside. In particular, three endmembers are used to express the major elements in common feldspar: Orthoclase (K-spar) $KAlSi_3O_8$, Albite $NaAlSi_3O_8$ and Anorthite $CaAl_2Si_2O_8$. A phase diagram below shows the variety of the minerals which constitute the feldspars, see figure 1.4.

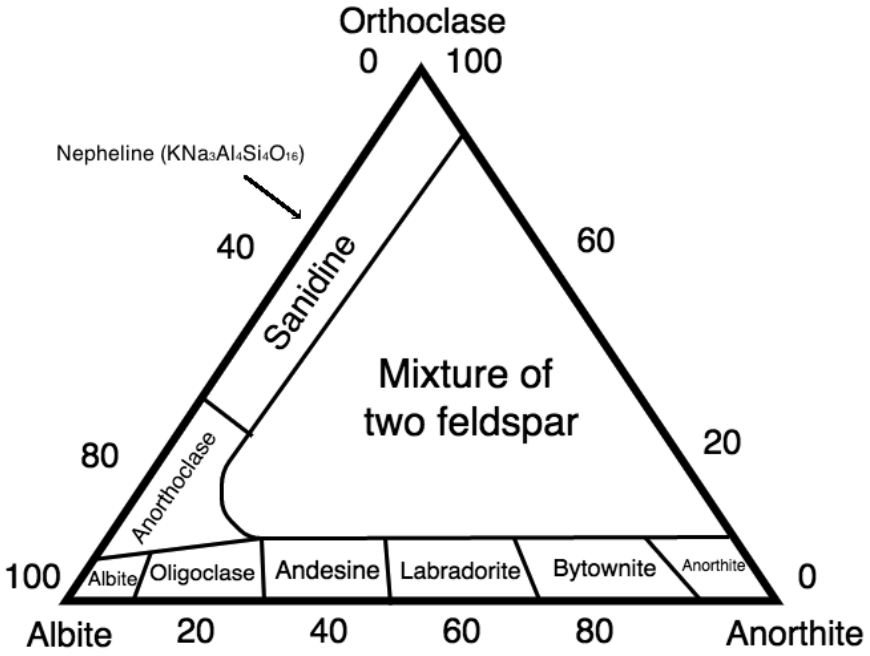

Fig. 1.4 Different minerals are marked on diagram based on the percentage of three endmembers: Orthoclase(Or), Albite(Ab) and Anorthite(An). Nepheline ($KNa_3Si_4Al_4O_{16}$) is marked by arrow. Diagram is adapted from [4]

Nepheline $KNa_3Si_4Al_4O_{16}$ is one of the minerals belonging to the feldspar group. It can be seen as a mixture of 25% Albite and 75% of Orthoclase.

1.1.2 Zeolites

The name of "zeolite" was first introduced by Swedish mineralogist Axel Fredrik Cronstedt in 1756. He observed that after rapidly heating the material stilbite, it would produce large amount of steam, which seems like boiling.

Zeolites have a wide range of application nowadays. There are 48 different types of zeolites that exist in nature [5]. Being rarely found in a pure form, they usually mix with many types of zeolites or minerals like quartz. Because of that, synthesising pure zeolites rather than obtaining from nature is preferred for commercial application as well as for academic research.

There are around 229 framework types of zeolites that have been identified by research up to this point [6]. Roughly, the structure of zeolites can be seen as atomic cages connected to each other. They are formed by TO_4 tetrahedral units, in which one Si or Al atom is at the centre surrounded by 4 oxygen atoms, see figure 1.5.

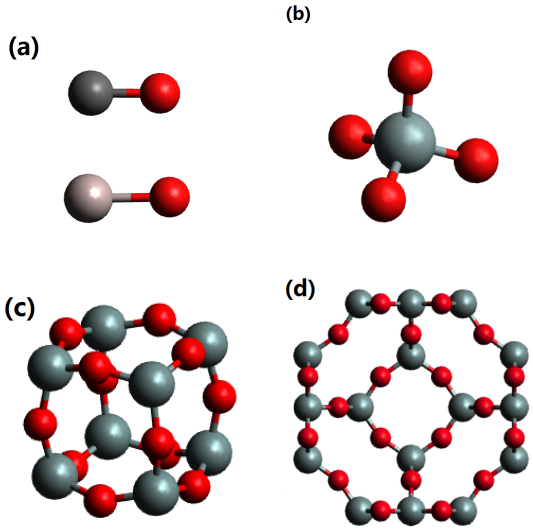

Fig. 1.5 (a) Si-O bond and Al-O bond. Bond lengths are 1.6 and 1.7 for Si-O and Al-O respectively. (b) A tetrahedral unit of zeolite in which one four oxygen (red) atoms are bonded to silicon(grey) atom, the central atom can be substituted with Al resulting one extra negative charge. (c) A double four ring cage of zeolite. (d) A $\beta-$cage in orthographic projection showing (001) face

The Lowenstein rule states that Al-O-Al connections are energetically forbidden in such aluminosilicate structure. Thus it should only contain Si-O-Si and Si-O-Al. Exceptionally, there is evidence in recent researches indicating that violation of such rule can happen[7] in melts and glasses. This Lowenstein rule disorder was also observed in this study and it is going to be discussed later. Constrained by the bonds lengths and angles within the tetrahedral units, the basic topology unit of feldspars and zeolites is limited in some specific forms. They are known as the secondary building units[8] (figure 1.6). In zeolites, those asymmetric topology units can be assembled into an microporous unit cell of low density. Therefore a perfect zeolite crystal can be described as an infinite repeating of such symmetric unit cell in three dimension of space. The porous nano-structure of it results in a extremely high ratio of surface area to volume. Therefore zeolites are widely used as absorbent in gas filtering and liquid purifying.

In general, zeolites contain pores or channels in one, two or all three dimension, with diameters varying between 5 to 10 Å. Framework type like LTA known as zeolite A and FAU known as zeolite Y, can have maximum pore diameter of 4.21 Å and 7.35 Å respectively in general[9][6]. Some of the diameters are large enough to be occupied by gas molecules such as helium and hydrogen [10]. Accordingly those zeolites can be used as a filter to separate mixed gases.

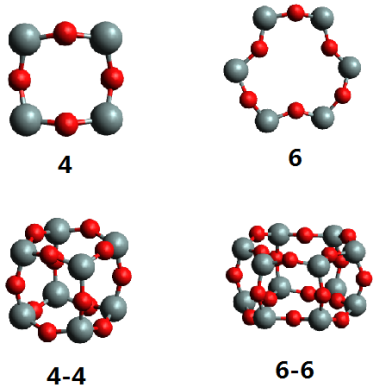

Fig. 1.6 Some examples of secondary building units (SBU) of zeolite that have been found including 4 fold ring, 6 fold ring, double 4 fold ring cage and double 6 fold ring cage.

Moreover, the pores can also be occupied by cations depending on the composition of zeolites. In pure silica zeolite, the number of oxygen atoms is twice the number of silicon, thus the system is charge balanced. In some zeolites the tetrahedral units centre can also be replace by Al atom. Because of the charge difference between Al^{3+} and Si^{4+}, cations like Na^{+} or K^{+} would appear inside the pores of zeolite to compensate the charges. During the pressure-induced amorphization or melt-quenching, those ions would then diffuse, creating the unique structure of alkali-silicate glasses. Details of the microscopic structures and the ion dynamics are going to be discussed in a later chapter.

1.1.3 MOF and ZIF

Apart from zeolites, there are also other porous materials could have similar potential for application. Discovered in the search of porous materials with larger pores and larger surface area than existing materials as well as the designable capability, the metal organic frameworks, known as MOFs, were firstly synthesized in the early 1990's.[11][12]

In particular, MOFs are micro-porous molecules composed of two major components: a cluster of metal ions and an organic molecule or ligand called linker. The variety of choices for metal and linker result in enormous numbers of potential structures of MOFs.

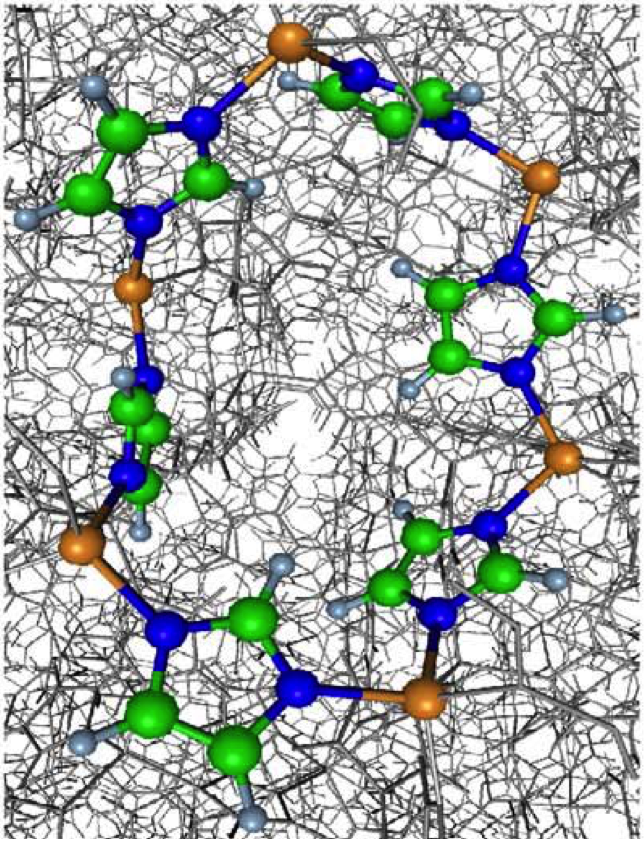

Fig. 1.7 A snapshots of a highlighted six-fold ring from ZIF-4. The bonding connection between linkers and transition metal ions as well as orientations of linkers are stable in ambient condition, resulting in an ordered topology. Yellow: zinc; grey: hydrogen; blue: Nitrogen; green: carbon

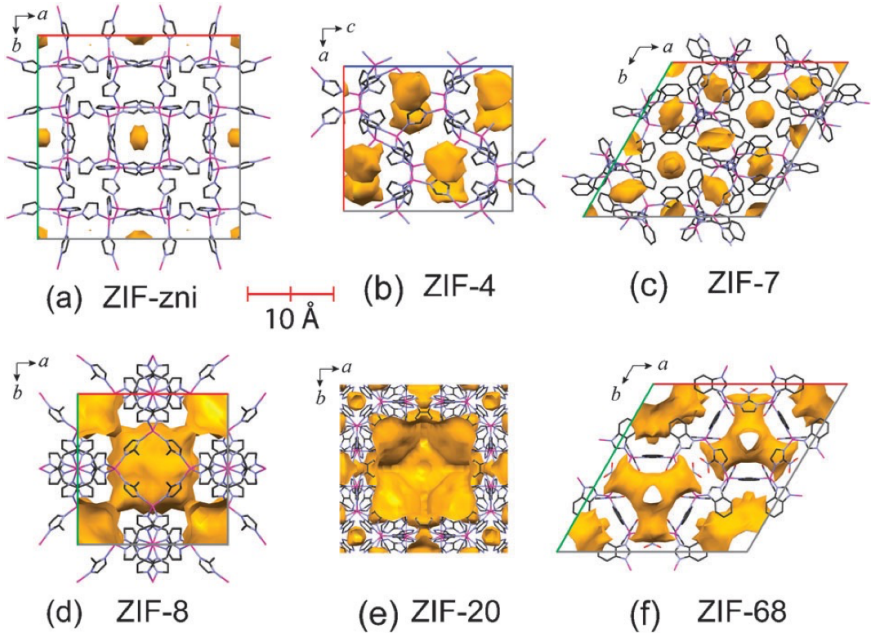

Fig. 1.8 Some topologies of different ZIFs. Orange surfaces map out the accessible volume. (a) ZIF-zni, (b) ZIF-4, (c) ZIF-7 (d) ZIF-8 (e) ZIF-20 and (f) ZIF68. Pink: zinc; gray: carbon; blue: nitrogen. Adapted from [15]

The properties of MOFs can be quite different from each other due to the variety of structures as well as the chemical compositions. In most cases, MOFs have a well defined porous structure, with pores of different size and shapes. Some of the MOFs can have extremely large pores of 25-30 Å diameters [13]. MOFs are also being widely used in gas separation and storage as well as waste encapsulation due to the flexibility of nano-pores[14]. Like zeolites, MOFs crystal can be unstable upon heating or pressure-induced compressing, resulting in an amorphous structure.

Zeolitic imidazolate frameworks (ZIFs) are a subclass of MOFs constructed by tetrahedral centre metal ions (eg. Zn or Co) bridged by imidazolate linkers (1.8). The organic ligands replace the bridging oxygen in conventional zeolite. Since the angle of metal-imidazolate-metal is around 145 ° , close to that in zeolites, the ZIFs can be directly compared to a certain zeolite topology (like SOD,LTA). The flexibility of ZIFs component units lead to the diversity of structure as shown in figure 1.8.

1.2 Glasses from melt-quenching

Generally, a solid material can be classified as crystalline or amorphous depending on whether it has disordered microscopic structure. Glass, an amorphous solid lacking the long-range order characteristic of crystal, is one of the most amazing materials to be investigated.

The history of glass-making can be traced back to 3500 BC in Mesopotamia, when glass items were regarded as a luxury because of their rarity. Since then, glasses have been widely produced and studied by mankind for centuries. As one of the oldest materials, glasses have a broad range of usage, from the traditional uses of windows and containers, to the optical fibre used in modern industry.

The most widely accepted and used method of forming the glasses is the melting and quenching technique. Commonly it can be done by rapidly cooling the molten state below melting temperature T_M of certain viscous glass-forming compositions without recrystallization. The structure of the supercooled liquid stays in the transformation to glass because of the rapid cooling. Different cooling rate result in different glass transition point T_g, which is also ascribed to fictive temperature T_f (figure 1.9). Higher T_f corresponds to the higher cooling rate. Another signature property that indicate the glass transition, is the changing of specific heat C_p. The C_p changes rapidly within a comparably narrow range around glass transition point.

There are lots of relations in science that can be interpreted using Arrhenius plot. In this case, the viscosity of glass forming liquid scales as a natural exponential function of $\frac{1}{T}$. The viscosity at the glass transition point T_g is defined to be $10^{12}\ Pa \cdot s$. In figure 1.10, log viscosity is plotted as a function of $\frac{T_g}{T}$. Defined by Austen Angell [17], a glass-forming liquid is called strong if its viscosity approximately obeys an Arrhenius law (SiO_2 in figure 1.10). On the other hand, viscosity follows a clearly non-Arrhenius behaviour in fragile glass-forming liquids (halide glasses in figure 1.10).

1.2.1 Silicate glass

Silicon dioxide, a major oxide in industries, is one of the simplest compositions to form glass on its own. Although there are several attempted theories for describing the structure of silica glass, the most widely accepted was proposed by Zachariasen[19] in

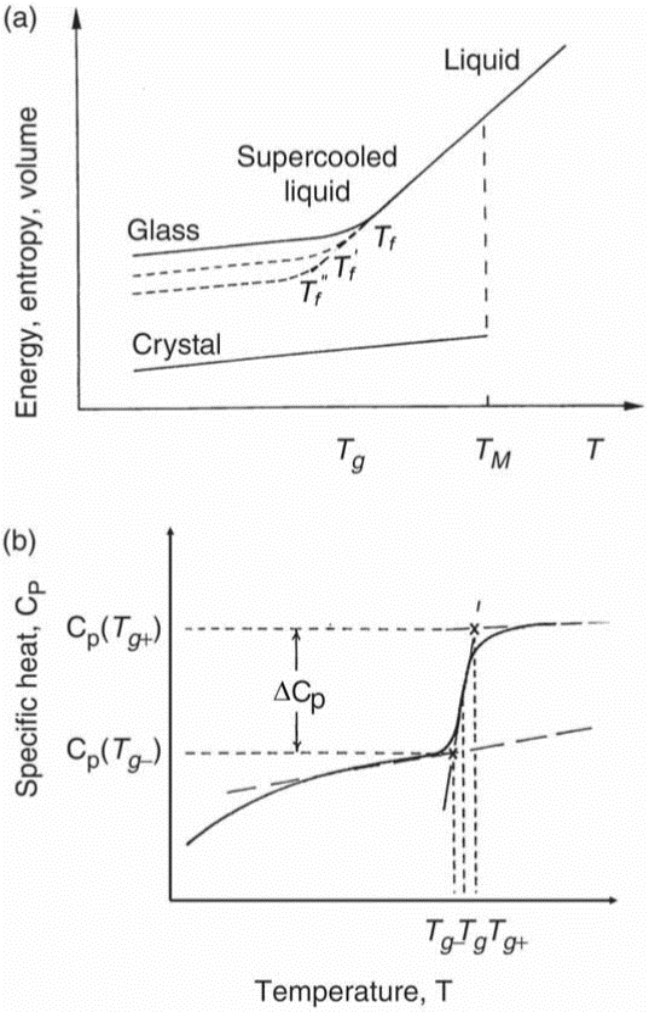

Fig. 1.9 Plots for different states: crystal, glass, supercooled liquid and liquid. (a) Energy, entropy, volume as a function of temperature. Higher T_f corresponds to the higher cooling rate (b) Specific heat falls rapidly around glass transition point T_g Adapted from [16]

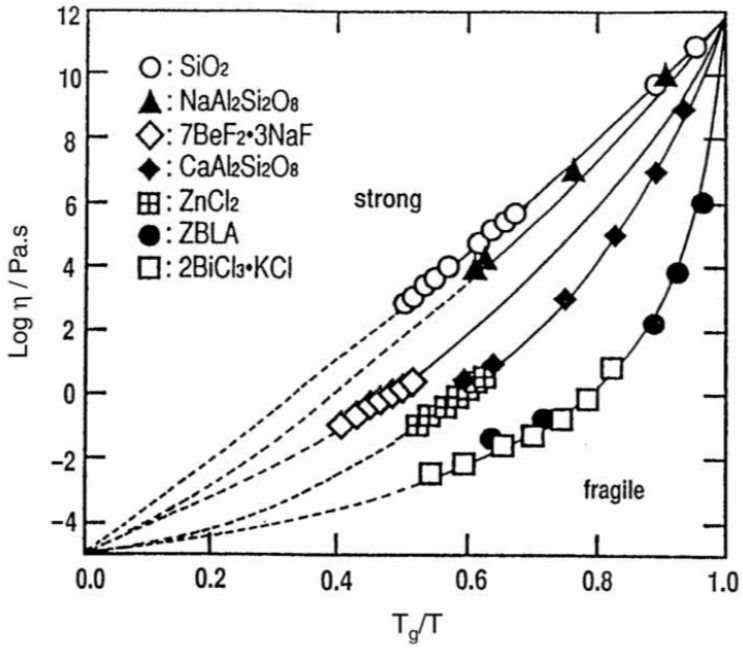

Fig. 1.10 Arrhenius plot of log scaled viscosities (η) of glass-forming liquids as a function of reciprocal temperature normalised to T_g. The curvature of each fit plot correspond to it's fragility. Adapted from [18]

1932. It assumes that silicon atoms are coordinated by four oxygen atoms, forming SiO_4 tetrahedral units. These units then form a network in which each of it shares an oxygen atom known as bridging oxygen with two other SiO_4 units. Zachariasen assumes that there would be a wider distribution of inter-tetrahedral angles in amorphous silica accounting for the violation of long-range order. A picture of such continuous random network shows below, see figure 1.11 .

1.2.2 Alkali-disilicate glass

Alkali oxides such as Li_2O, Na_2O and MgO are often added to SiO_2 as fluxes to lower the melt viscosity and glass transition temperature creating various glasses. Each alkali ion added to the melts leads to the breaking of a certain number of Si-O-Si bonds to create a non-bridging oxygen (NBO) which the charge compensating alkali ion is then associated with. This has been confirmed by molecular dynamics simulation of glasses [20] including rare-earth [21].

In Zachariasen's continuous random network model, the position of network modifiers in the glass network is left unspecified. Recent research examined the local structure

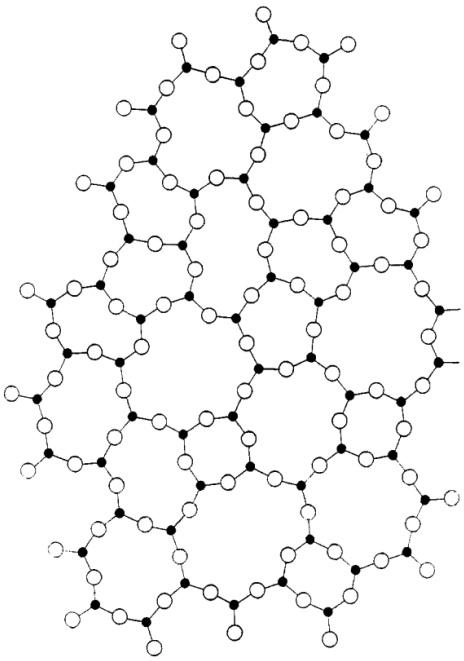

Fig. 1.11 A two dimensional structure of silicate glass showing the continuous random network (CRN) proposed by Zachariasen[19]. Filled circles: Si; open circles: O.

around modifier atoms in various glass compositions using the extended X-ray absorption fine structure (EXAFS) technique [22]. Rather than the homogeneous distribution of modifiers described by Zachariasen (subsequently confimed by the detailed X-ray analyses by Warren and his co-workers), evidence were found suggesting that modifier atoms are segregating inside of modified rich ion channels. The theory that nanoscale segregation of oxide glasses occurs, leading to the formation of different regions rich in modifiers and network formers is often referred to as the modified random network (MRN) model[22].

1.2.3 Mixed alkali effect

In most oxide glasses, where two ion species coexist such as Na^+ and K^+, the properties like conductivity and diffusivity can show a non-linear manner when one alkali cation replaces another. Known as the mixed alkali effect, this phenomenon has been studied more than 100 years but it's still a matter of continuing research.

It was found that adding another alkali ion species would considerably reduce the diffusivity of the other compared to single alkali glasses. Some properties, such

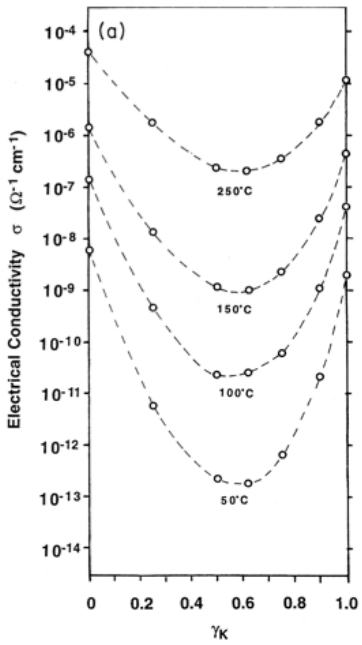

Fig. 1.12 The mixed alkali effect (MAE). Electrical conductivity measurements on $(K_xNa_{1-x})_2Si_4O_9$ glasses [23]. The effect of MAE become weaker at the higher temperature.

as conductivity and diffusion constant, achieve a pronounced value at the 50/50 composition, see figure 1.12.

1.2.4 Aluminosilicate glass

When Si at the centre of the tetrahedral unit is substituted by Al, the extra negative charge from AlO_4^- requires compensating by the cations. Meanwhile because Al is still fully linked with O in tetrahedral units, this can be achieved without non-bridging oxygen in contrast to alkali silicate glass. This results in a distinguished structure for Alumino-silicates glass which can be modelled with a Compensated Continuous Random Network (CCRN), see figure 1.13 (c).

1.3 Pressure-induced amorphization

The glasses discussed above are mostly made from melting and quenching. Different from that, some materials can be amorphized through compression at certain pressure or at modest temperature forming a disordered structure similar to thermal-induced

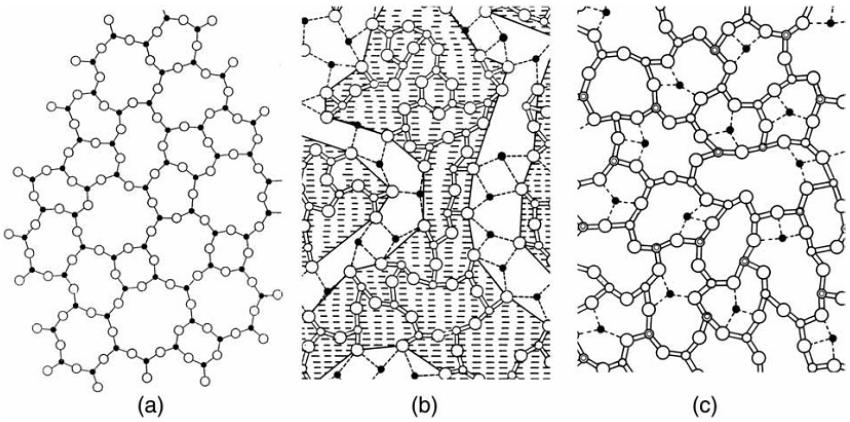

Fig. 1.13 Three random network models in two dimension. (a) Continuous random network (CRN) model for silicate glass. Filled circles: Si; open circles: O [19](b) Modified random network (MRN) model for modified silicate glass such as alkali glass. Small open circles: Si; large open circles: O; Filled circles: modifiers [22] (c) Compensated continuous random network (CCRN) model for alumina-silicate glass. Large open circles: O; Small open circles: Si; Small bold open circles: Al. Filled circles: cations [1]

glass. The amorphization process known as pressure induced amorphization (PIA) has been considered in this thesis[16]. For instance, $\alpha-$quartz and coesite can be transformed to amorphous solids at 25-35 GPa and 300K in a diamond-anvil cell [24].

Nano-porous materials like Zeolitic Imidazolate Frameworks (ZIFs) and zeolites are found to have huge potential in producing these pressure-induced amorphous structures. This is due to the flexibility of their nano-porous structure in which topology can be dramatically affected by the pressure-induced compressing. In particular, ZIF8 and sodalite, both sharing similar sodalite cage topology, are going to be discussed in this study.

CHAPTER 2

METHODOLOGY

2.1 Molecular Dynamics

Molecular dynamics is a computer simulation method that has been developed for almost 60 year since 1959 [25]. Generally, a molecular modelling study can be summarised in three stages.

The first stage is to build the initial atomic structure and inter-atomic interactions of the system. Two major models that have been widely used are molecular mechanics and quantum mechanics. Both these models can give the total energy of the system based on the arrangement of atoms. Therefore it controls how the energy would change whenever the positions of atoms changed. In general, they require a certain set of parameters (for instances classical potential for MD).In molecular dynamics, tuning the parameters for the potentials is probably the most crucial part. While in quantum mechanics, classical method is no longer sufficient enough to describe the system. So in DFT method, basis set and pseudo potential are going to be considered instead. Details of both methods are going to be discussed later in this chapter.

The second stage is about the massive calculation itself which usually runs on high performance calculation facilities. In this study, most of the simulation was performed on High Performance Computing Wales (HPC Wales). It currently has 17000 cores with a 320 Tflop capacity.

In the last stage, usually a calculation for validity would be performed at first including structure or energy verification. Then some physical properties of interest can be analysed..

2.1.1 Initial structure

To start the simulation, it's necessary to have an initial structure of the system. In most cases, a super cell was built from a pre-measured unit cell. The unit cell file usually contains the coordinates of atoms inside the crystallographic structure and the symmetry information. Those files, which usually could be found in material database like Chemical Database Service (CDS) at Daresbury[26], are usually associated to papers published by mineralogists or material scientists. Ideally the coordinates are ready to be put into simulation without further editing. But sometimes the coordinates need to be adjusted or relaxed to fit in the condition of interest. The coordinates of a super cell can be obtained by creating image copy of the unit cell in three dimensions. Sometimes this create duplicated atoms on the boundary. They should be removed otherwise severe problem would occur due to the infinitely strong interaction of two atoms with zero distance in between.

2.1.2 Solving Newton's equations of motion

Given a set of atoms and the prescribed forces between them, molecular dynamics simulation can calculate the time evolution of atom positions. The trajectories of atoms are derived by solving the Newton's equation where atoms interact with each other via the prescribed empirical potential (also named force field). Quite often the potential is taken to be pairwise additive for computational practicality. In this thesis, the pair potential of interest are the BKS format potential and Coulombic potential.

The equations of motion for the N-body system can be written as

$$m\ddot{\mathbf{r}}_i(t) = \mathbf{F}_i(t), \quad i = \{1, ..., N\} \tag{2.1}$$

where t is time , $\mathbf{F}_i$ is force, m is mass,$\mathbf{r}_i$ is the position of atom i.

Considering only pairwise interaction, given the positions of all the other particles in the system at time t, the force on particle i can be calculated by:

$$\mathbf{F}_i(t) = -\nabla_i \sum_{i=1}^{N} \sum_{j>1}^{N} U(r_{ij}(t)) \tag{2.2}$$

where $r_{ij}(t) = |\mathbf{r}_i(t) - \mathbf{r}_j(t)|$. With the initial positions and velocities of each particles, the basic MD procedure, which repeats for the desired number of iterations, is as follows:

1. The force on each particles is calculated from Equation (2.2)

2. The positions of the particles of the system are evolved in time according to Equation (2.1)

For the second step, an integration algorithm is required.

2.1.3 Integration

In MD simulations, the dominant calculation is solving the Newton's equation numerically by integrating particle position and velocities in time. Because most of the MD simulation requires considerable amount of simulation time, it is essential that the integration provides the stability of some quantities such as energy. Also, the time-reversibility of the integration scheme is required. So back tracking the atoms through history is possible. Moreover, a large time step is preferable, without too much loss of accuracy.

The general idea of it is to attempt to predict the molecular positions or velocity on time $t + \delta t$ based on the dynamics information given on time t.

Basic Verlet integration

Verlet integration is a numerical method first used in 1791 by Delambre, and has been developed by many people since then. It's well known that Loup Verlet used the algorithm in molecular dynamics calculation[27] thus it's named after him.

Considering the 4th order Taylor expansion of the position:

$$\begin{aligned} \mathbf{r}_i(t+\delta t) &= \mathbf{r}_i(t) + \mathbf{v}_i(t)\delta t + \frac{\mathbf{F}_i(t)}{2m}\delta t^2 + \frac{\dddot{\mathbf{r}}_i}{3!}\delta t^3 + O(\delta t^4) \\ \mathbf{r}_i(t-\delta t) &= \mathbf{r}_i(t) - \mathbf{v}_i(t)\delta t + \frac{\mathbf{F}_i(t)}{2m}\delta t^2 - \frac{\dddot{\mathbf{r}}_i}{3!}\delta t^3 + O(\delta t^4) \end{aligned} \tag{2.3}$$

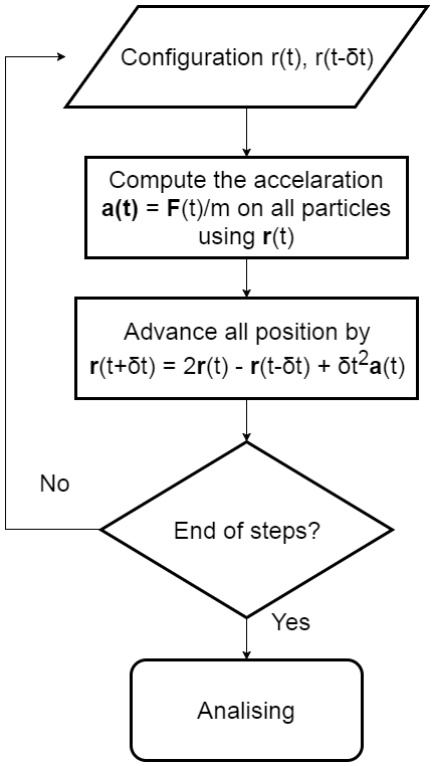

Fig. 2.1 The flowchart of Original Verlet cycles

Thus according to information on time t and $t-\delta t$, we can obtain the $r(t+\delta t)$ from (2.3):

$$\mathbf{r}(t+\delta t) = 2\mathbf{r}(t) - \mathbf{r}(t-\delta t) + \delta t^2 \mathbf{a}(t) + O(\delta t^4) \tag{2.4}$$

The velocity are not needed here if trajectory is the only thing of interest. But for the calculation of kinetic energy, we can obtain the velocity by:

$$\mathbf{v}(t) = \frac{\mathbf{r}(t+\delta t) - \mathbf{r}(t-\delta t)}{2\delta t} + O(\delta t^2) \tag{2.5}$$

A flow chart of Verlet MD cycle is shown as figure (2.1)

Unfortunately, this leads to errors of order δt^2 for velocity since the algorithm introduce some unnecessary numerical imprecision[28].

Also, $r(t+\delta t)$ and $r(t-\delta t)$ play symmetrical roles in equation (2.4). This means that upon changing the sign of the time increment δt, the algorithm will (in principle) retrace the steps it just followed. Thus it's time-reversible.

Leapfrog

Similar to the basic Verlet, a method named leapfrog is also being often used. In leapfrog integration, the equations for updating position is:

$$\mathbf{r}(t+\delta t) = \mathbf{r}(t) + \delta t \mathbf{v}(t+\frac{1}{2}\delta t) \tag{2.6}$$

Molecular dynamics simulations normally require properties that depend on position and velocity at the same time. In the leapfrog algorithm, the velocity at time t is averaged from half a timestep from either side of time t:

$$\begin{aligned} \mathbf{v}(t+\frac{1}{2}\delta t) &= \mathbf{v}(t-\frac{1}{2}\delta t) + \delta t \mathbf{a}(t) \\ \mathbf{v}(t) &= \frac{1}{2}(\mathbf{v}(t+\frac{1}{2}\delta t) + \mathbf{v}(t-\frac{1}{2}\delta t)) \end{aligned} \tag{2.7}$$

Leapfrog algorithm is well known for its time-reversibility and simplistic nature thus it's often used in Hybrid Monte Carlo[29].

Velocity Verlet

The Velocity Verlet assumes that positions, velocities and forces are known at each full timestep. The positions and velocities of atoms are evaluated by:

$$\begin{aligned} \mathbf{r}(t+\delta t) &= \mathbf{r}(t) + \delta v(t) + \frac{1}{2}\delta t^2 \mathbf{a}(t) \\ \mathbf{v}(t+\delta t) &= \mathbf{v}(t) + \frac{1}{2}\delta t[\mathbf{a}(t) + \mathbf{a}(t+\delta t)] \end{aligned} \tag{2.8}$$

It can be proved that the error on the Velocity Verlet is of the same order as the Basic Verlet. Also because tracking down velocity at every timestep is not necessary for this algorithm, the program for running this methods can be less memory consuming.

A flow chart of MD cycles using Velocity Verlet is shown as figure (2.2).

Velocity Verlet was chosen for most of the integration calculation involved in this study for its accuracy and efficiency.

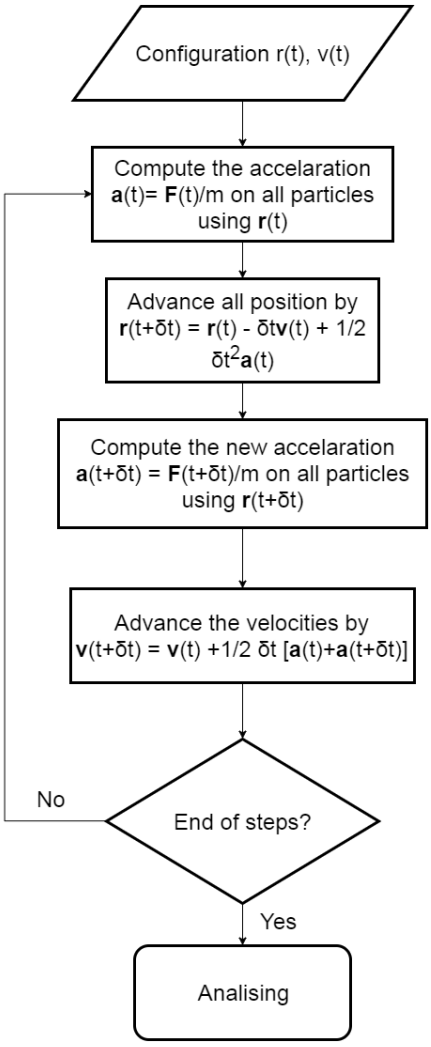

Fig. 2.2 The flowchart of Velocity Verlet MD cycles

2.1.4 Periodic boundary condition

Mostly, the molecular dynamic simulations aim to probe the structural and dynamic properties within a system from hundreds particles to tens of thousands of particles. Although with enormous computation capacity and specific method, this number is going to be higher. For instance, a 314000 particles simulation using NAMD (Nanoscale Molecular Dynamics), which is known for its parallel efficiency and is often used to simulate large systems, was reported in 2005[30]. In most of system with less particles, the surface effect can not be considered negligible. In order to physically replicate the system, commonly a large or infinite structure is going to be built for the simulation. Hence periodic boundary condition is necessary for solving this problem.

First, an unit cell is required for the periodic boundary condition. The unit cell, which usually represents the primitive cell of crystal, can have different shape attributing to various space group of crystal structure. There are 230 space groups defined by different cell parameters and angles.

Then, the desired system can be constructed by repeating the unit cell in N dimensions. Those copies of the original unit cell are called images. Consider a three-dimensional system, the image position of a particle $\mathbf{r}_i$ can be obtained by:

$$\mathbf{r}_m = \mathbf{r}_i + n_1\mathbf{c}_1 + n_2\mathbf{c}_2 + n_3\mathbf{c}_3 \tag{2.9}$$

In this periodic system, a given particle would now interacts with all other particles in the same periodic cell and all particles (including its own periodic image) in all other cells. While the infinite repeating of unit cell has been applied, the interactions between atoms would be difficult to handle. The more periodic image to be considered, the more interaction it needs to be calculated. For long range interactions like Coulombic force, this can be solved by Ewald summation. For short range interaction, a distance called cutoff is introduced to bring down the cost of calculation. The cutoff defines the maximum range between two atom pairs who can interact with each other. This is similar to the inter-atomic potential that is levelling out to zero when atom pair are infinitely far away from each other.

The figure (2.3) below gives a two dimension example of periodic boundary condition.

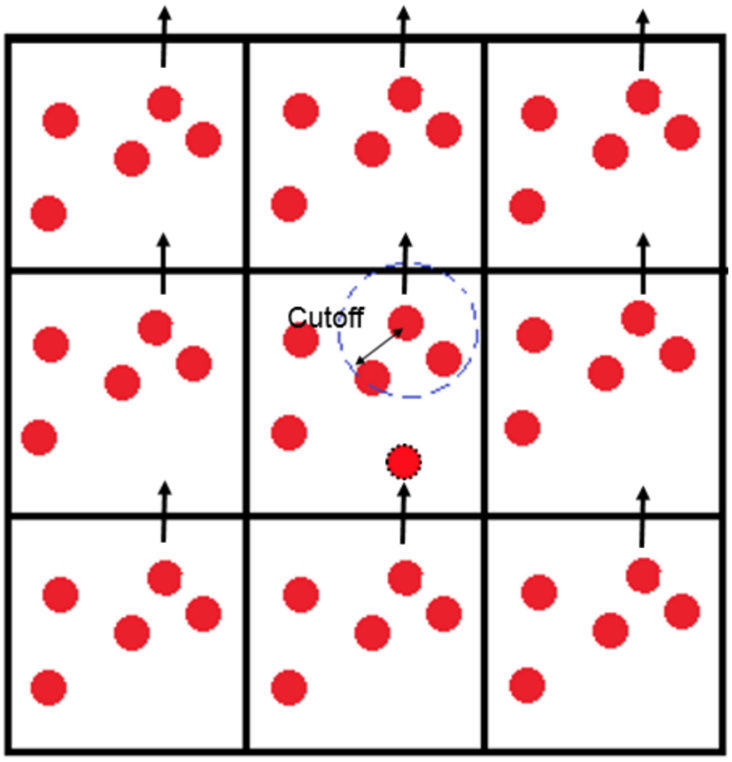

Fig. 2.3 A two dimensional example showing how periodic boundary condition (PBC) works. The central cell represents the simulation cell surrounded by its periodic image. Whenever the red particles move out of the simulation cell, it equivalently move into another periodic image as shown in picture. The blue circle indicates the maximum distance of another atom that the central red atom can interact with.

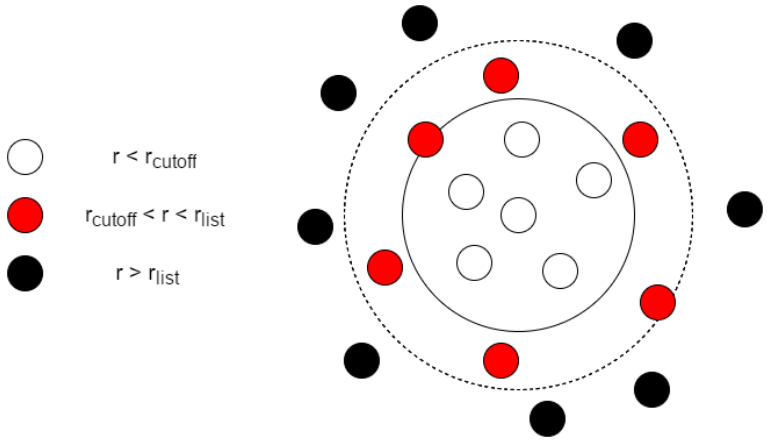

Fig. 2.4 The Verlet list. The potential cutoff (solid circle) and the list range (dashed circle) are indicated. the list must be reconstructed before particles outside the list range (black) entering the list sphere.

2.1.5 Neighbour list

Computing the non-bonded contribution to the interatomic interaction in the MD involves a large amount of pairwise calculation. For an N-atom system, the number of all possible pairs is $\frac{1}{2}N(N-1)$. Assuming that the non-bonded potential are of short range, $U(r_{ij}) = 0$ if $r_{ij} > r_{cut}$, the cutoff, the program can skip the force calculation, avoiding unnecessary work to bring down the computation cost. Even with that, calculating all the short range pair still consumes a lot of time.

Verlet suggested a technique for improving the computing speed. The potential cutoff sphere r_{cut} around a particular atom is surrounded by a larger sphere r_{list} as shown in figure 2.4. At the first step in a simulation, a list is constructed including all the neighbours of each atom, for which the pair separation is within r_{list}. Over the next few MD time steps, only pairs appearing in the list are checked in the force routine. From time to time the list is updated: it is essential to do this before any unlisted pairs have crossed the safety zone and come within interaction range. The list updating can be triggered automatically if a record was kept of the distance travelled by each atom since the last update. The choice of list cutoff distance r_{list} is a compromise: larger lists will need to be reconstructed less frequently, but will not save as much of time on computing as smaller lists.

2.1.6 Interatomic potential

As mentioned before, the interaction between atoms are determined by the pre-described potential. In most cases, the interactions are treated where no chemical bonds are formed, i.e, gases,glasses and amorphous solids. Commonly the non-bonded interactions are weaker than bonded ones. A suitable potential should be able to replicate certain physical properties or phenomenons which are in good agreement with experiments. Thus, which potential to use depends highly on the problem of interest. The potential energy can be a function of the relative position of particles pairs, triplets and even larger groups of interacting particles.

$$U = \sum_{i=1}^{N} \sum_{j=1 j\neq i}^{N} U(\mathbf{r}_i \mathbf{r}_j) + \sum_{i=1}^{N} \sum_{j=1 j\neq i}^{N} \sum_{k=1 k\neq i,j}^{N} U(\mathbf{r}_i \mathbf{r}_j \mathbf{r}_k) + ... \tag{2.10}$$

In this study, mostly the pair-wise potential is going to be considered. There are lots of existing potentials which can be written as different form with some adjustable parameters. An example of the force field formula is shown below:

$$\mathbf{U} = \sum_{bonds} \frac{k_1}{2}(r_{ij} - r)^2 + \sum_{i=1}^{N} \sum_{j=i+1}^{N} (U_{non-bonded} + \frac{1}{4\pi\varepsilon_0}\frac{q_i q_j}{r}) \tag{2.11}$$

In this formula, the former term represents the bonds term in between two connected atom pair. The later term represents the non-bonded potential and Coulombic interaction. There are lots of popular potentials have been proved to be sufficient for simulating pair-wise non-bonded inter-atomic interactions. Some examples are listed below:

$$\begin{aligned} \textbf{Morse}: &\quad U(r) = E_0[\{1 - e^{-k(r-r_0)}\}^2 \\ \textbf{Lennard-Jones}: &\quad U(r) = 4\varepsilon\left[(\frac{\sigma}{r})^{12} - (\frac{\sigma}{r})^{6}\right] \\ \textbf{Buckingham}: &\quad U(r) = Aexp(-\frac{r}{\rho}) - \frac{C}{r^6} \end{aligned} \tag{2.12}$$

Coulomb Energy and Ewald summation

Given the charges of ions $q_1, q_2, q_3, ..., q_N$ and their position $\mathbf{r}_1, \mathbf{r}_2, \mathbf{r}_3, ..., \mathbf{r}_N$, the total electrostatic potential energy can be obtained by :

$$E = \frac{1}{4\pi\varepsilon_0}\frac{1}{2}\sum_{i\neq j}\frac{q_i q_j}{\mid \mathbf{r}_i - \mathbf{r}_j \mid} \tag{2.13}$$

where all interactions are divided by 2 to avoid double counting. For a finite system of charges, this expression can be evaluated directly. However, periodic boundary condition are often used in simulation thus the system would become infinite. In an infinite system, the expression (2.13) does not converge and numerical approach must be used to evaluate the energy. In fact, it is possible to define a meaningful interaction energy by use of an Ewald transformation if the system is neutral.

The Ewald method introduces two adjustments[31]. Firstly each ion is effectively neutralised (at long range) by the superposition of a spherical Gaussian cloud of opposite charge centred on the ion. The combined assembly of point ions and Gaussian charges becomes the real space part of the Ewald sum. Secondly, a second set of Gaussian charges is added into the system with same charges as the original point ions and again centred on the point ions. The potential due to these Gaussians then can be solved as a Fourier series in reciprocal space. Additionally, a correction has to be added, known as the self energy correction, which arises from a Gaussian acting on its own site, and is constant.

The error function erf(x) and its complement erfc(x) are defined as:

$$\begin{aligned} erf(x) &= \frac{2}{\sqrt{\pi}}\int_0^x e^{-t^2}dt \\ erfc(x) &= \frac{2}{\sqrt{\pi}}\int_x^\infty e^{-t^2}dt \end{aligned} \tag{2.14}$$

Ewald noted that:

$$\frac{1}{r} = \frac{erf(\frac{1}{2}\sqrt{\eta}r)}{r} + \frac{erfc(\frac{1}{2}\sqrt{\eta}r)}{r} \tag{2.15}$$

In this expression, the first term goes to a constant ($\sqrt{\frac{\eta}{\pi}}$) as $r \to 0$, but has a long range tail as $r \to \infty$. The second term has a singular behaviour as $r \to 0$, but vanishes exponentially as $r \to \infty$.

Thus, the formula (2.13) can be replaced with two convergent summations:

$$\begin{aligned} E &= \frac{1}{4\pi\varepsilon_0}\frac{1}{2}\sum_{i\neq j}\frac{q_i q_j}{\mid \mathbf{r}_i - \mathbf{r}_j \mid} \\ &= \frac{1}{8\pi\varepsilon_0}\left(\sum_{i\neq j}\frac{q_i q_j erf(\frac{1}{2}\sqrt{\eta}\mid \mathbf{r}_i - \mathbf{r}_j \mid)}{\mid \mathbf{r}_i - \mathbf{r}_j \mid} + \sum_{i\neq j}\frac{q_i q_j erfc(\frac{1}{2}\sqrt{\eta}\mid \mathbf{r}_i - \mathbf{r}_j \mid)}{\mid \mathbf{r}_i - \mathbf{r}_j \mid}\right) \end{aligned} \tag{2.16}$$

For an appropriate choice of the parameter η, the second summation in (2.16) converges quickly and can be evaluated directly. The first term in the summation must be transformed into Fourier space.

2.1.7 Statistics Ensemble

Usually molecular dynamics simulations are performed under a variety of external constraint. To set up the constraint, the ensemble has to be stated in the input file. Micro-canonical (NVE) ensemble, the most commonly used constraint, represents the constant atom number N, volume V and total energy E.

Assuming a system with N particles in dimension number D, the temperature and pressure of the system can be obtained by the methods below. Given the momentums p_i of all the atoms, the total kinetic energy of the system is calculated by:

$$E_k = \sum_{i=1}^{N}\frac{|p_i|^2}{2m_i} \tag{2.17}$$

where m_i is the mass of atoms. Then statistically the temperature can be obtained by:

$$T = \frac{2E_k}{DNk_B} \tag{2.18}$$

where k_B is the Boltzmann constant, . Similarly, the pressure can be calculated from the virial equation:

$$\begin{aligned} PV &= Nk_BT + \frac{1}{D}\langle\sum_{i=1}^{N}\mathbf{r}_i\cdot\mathbf{F}_i\rangle \\ &= \frac{1}{D}\left[2E_k + \langle\sum_{i=1}^{N}\mathbf{r}_i\cdot\mathbf{F}_i\rangle\right] \end{aligned} \tag{2.19}$$

where V is the total volume, r_i is the position of atom i, F_i is the force acting on atom i.

Thermostat

In most cases, a thermostat is required to control the temperature of the system. Thermostats are designed to help a simulation sample from the correct ensemble (i.e. NVT or NPT) by modulating the temperature of the system. In simulations, the "temperature" is usually computed from the kinetic energy of the system. In fact, the thermostat does not fix the temperature as that would lead to a fixed total kinetic energy. Rather, it makes sure that the average temperature of a system is correct. So usually the instantaneous temperature is fluctuating during simulation.

In the Langevin thermostat, atoms in the system receive a random force and have their velocities lowered using a constant friction. The average magnitude of the random forces and the friction are related in a particular way, which guarantees that the fluctuation-dissipation theorem is obeyed, thereby guaranteeing NVT statistics.

In this formalism, the equation of motion (2.1) is modified:

$$m\ddot{r} = \dot{\mathbf{p}} = -\nabla_i U - \Gamma\mathbf{p}_i + \mathbf{R}_i(t) \tag{2.20}$$

where momentum $\mathbf{p}_i = m\dot{r}_i$ and $\mathbf{R}_i$ is a random force that is uncorrelated in time and across atoms, given by:

$$\langle\mathbf{R}_i(t),\mathbf{R}_j(t')\rangle = \delta_{ij}\delta(t-t')6k_BmT\Gamma \tag{2.21}$$

In the Berendsen thermostat, the system is weakly coupled to a heat bath with some temperature. The temperature of the system is corrected by:

$$\dot{\mathbf{p}} = -\nabla_i U - \mathbf{p}_i[\frac{T}{T_0} - 1]\frac{1}{\tau} \tag{2.22}$$

where T is the instantaneous temperature and T_0 is the preset temperature. So if $T > T_0$, the system is too hot, the $\frac{T}{T_0} - 1$ would then be positive thus the system will begin to cool down. If $T < T_0$, the system is too cold, the reverse happens.

This method is widely used due to the efficiency of calculation. In most instances, the system might be initially equilibrated with the Berendsen ensemble, while properties are calculated with the control of Nosé-Hoover.

The Nosé-Hoover thermostat was originally developed by Nosé and was improved further by Hoover. The idea is to introduce a fictitious dynamical variable ζ which slows down or accelerates atoms until the temperature is equal to the desired value. In three dimension, the equations can be written as:

$$\begin{aligned}
\dot{\mathbf{p}} &= -\nabla_i U - \zeta \mathbf{p}_i \\
\dot{\zeta} &= \frac{1}{Q}\left[\sum_i^N \frac{|\mathbf{p}_i|^2}{2m_i} - \frac{3N+1}{2}k_B T\right] \\
&\approx \frac{1}{Q}\left[\sum_i^N \frac{|\mathbf{p}_i|^2}{2m_i} - \frac{3N}{2}k_B T\right]
\end{aligned} \tag{2.23}$$

where Q is the effective "mass" that relate to the relaxation time. $\frac{3N+1}{2}$ can be changed to $\frac{3N}{2}$ when N is large enough. In steady state, $\dot{\zeta} = 0$, the kinetic energy is given by $\frac{3N+1}{2}k_B T$ as required by equipartition.

Barostat

Similar to temperature control, there are different barostats that control the pressure of system. The idea of a barostat is to change the size or shape of the simulation cell in order to obtain a desired average pressure $P_{desired}$ or isotropic stress tensor σ. In the isotropic implementation of Berendsen barostat [32], at each timestep the MD cell

volume, coordinates, and cell vectors are scaled by a factor η:

$$\eta = 1 - \frac{\Delta t}{\tau_P}\frac{P_{desired} - P}{P_{desired}} \tag{2.24}$$

where τ_P is the relaxation time specified by user, P is the instantaneous pressure.

In the Hoover thermostat and barostat, the equations of motion for isotropic fluctuations are:

$$\begin{aligned}
\frac{d\mathbf{r}(t)}{dt} &= \mathbf{v}(t) + \eta(t)(\mathbf{r}(t) - \mathbf{R}_0) \\
\frac{d\mathbf{v}(t)}{dt} &= \frac{\mathbf{f}(t)}{m} - [\chi(t) + \eta(t)]\mathbf{v}(t) \\
\frac{d\chi(t)}{dt} &= \frac{N_f k_B}{O}(\mathscr{T}(t) - T_{ext}) + \frac{1}{Q}(W\eta(t)^2 - k_B T_{ext}) \\
\frac{d\eta(t)}{dt} &= \frac{3}{W}V(t)(\mathscr{P} - P_{ext}) - \chi(t)\eta(t) \\
\frac{dV(t)}{dt} &= [3\eta(t)]V(t)
\end{aligned} \tag{2.25}$$

in which R_0 is the centre of mass. $\chi(t)$ and η are associated with thermostat and barostat respectively. Also they are coupled. $V(t)$ is the volume of system, Q is the effective "mass" for thermostat, W is the effective "mass" for barostat.

2.2 Quantum simulation/Ab initio

Although classical MD methods can successfully provide results matching well with experiments, there are still some obstacles exist that can not be simply ignored. Especially, for different system it requires adjusted potential which is very sensitive making it difficult to find the best fitting potential. Essentially, molecular dynamics methods treat every particle as classical object which would lead to lots of problems when dealing with more complicated system like organic-inorganic hybrid material. Quantum theory has been proved to be very useful for understanding the behaviour of particles. Besides, it also provide us the information that not exist in MD such as energy band. Accordingly , an alternative way of performing MD simulation with quantum theory has become very popular nowadays.

2.2.1 Schrödinger Equation

In principle, the quantum system can be described by a partial differential equation called Schrödinger equation. Depending on the question of interest, the equation has two form if time was considered or not:

$$\hat{H}\psi = E\psi \tag{2.26}$$

for the time-independent Schrödinger equation and

$$\hat{H}\Psi = i\hbar\frac{\partial\Psi}{\partial t} \tag{2.27}$$

for the time-dependent Schrödinger equation.

The time-dependent Schrödinger equation accommodates non-stationary state solutions.

2.2.2 Born-Oppenheimer approximation

The solution ψ to the time-independent Schrödinger equation (2.26) depends on the spin and position coordinates of all electrons $\vec{x}$ and nuclei $\vec{X}$:

$$\psi = \psi(\vec{X},\vec{x}) \tag{2.28}$$

using short-hand notation $\vec{x} \equiv (\vec{r}_1,\sigma_1,\vec{r}_2,\sigma_2,...,\vec{r}_N,\sigma_N)$ and $\vec{X} \equiv (\vec{R}_1,\Sigma_1,\vec{R}_2,\Sigma_2,...,\vec{R}_N,\Sigma_N)$

One of the most well-known principle in quantum mechanics is the Heisenberg uncertainty principle. For electron and nuclei, it can be written as follow:

$$\begin{aligned}\Delta\vec{x}\cdot\Delta p = \Delta\vec{x}\cdot\Delta(mv) = m\Delta\vec{x}\cdot\Delta v \geq \hbar \\ \Delta\vec{X}\cdot\Delta P = \Delta\vec{X}\cdot\Delta(MV) = M\Delta\vec{X}\cdot\Delta V \geq \hbar\end{aligned} \tag{2.29}$$

According to the statistical mechanics, the kinetic energy can be obtained by:

$$\frac{3}{2}k_BT = \langle\frac{1}{2}mv^2\rangle = \langle\frac{1}{2}MV^2\rangle \tag{2.30}$$

Because the mass of nucleus is way more bigger than the electron(1840 times for a lightest nucleus), it can be obtained that:

$$\frac{\Delta X \Delta V}{\Delta x \Delta v} \simeq \frac{m}{M} \ll 1 \tag{2.31}$$

Thus it can be estimated that the nuclei are much more localized in space than the electrons:

$$\begin{aligned} \frac{\Delta V}{\Delta v} &\simeq \sqrt{\frac{m}{M}} \ll 1 \\ \frac{\Delta X}{\Delta x} &\simeq \sqrt{\frac{m}{M}} \ll 1 \end{aligned} \tag{2.32}$$

So it's reasonable to treat the nuclei as classical particles that generate electrostatic field. By neglecting the kinetic energy of the nuclei, the total energy can be obtained by:

$$\begin{aligned} E_e(\vec{X}) &= \hat{H}_{p,n-e} + \hat{H}_{p,e-e} + \hat{H}_{k,e} \\ E &= \hat{H}_{p,n-n} + E_e(\vec{X}) \\ &= \frac{1}{2} \sum_{k1 \neq k2=1}^{M} \frac{1}{4\pi\varepsilon_0} \frac{Z_{k_1} Z_{k_2} e^2}{|\vec{R}_{k_1} - \vec{R}_{k_2}|} + E_e(\vec{X}) \end{aligned} \tag{2.33}$$

Hartree-Fock method

According to the variational principle, the energy computed from a guessed wave function ψ is an upper bound to the true ground-state energy E_0.

So for any trial wave function ψ,

$$E' = \frac{\langle \psi | H | \psi \rangle}{\langle \psi | \psi \rangle} >= E_0 \tag{2.34}$$

Full minimization of the functional $E[\psi]$ with respect to all allowed N-electrons wave functions will give the true ground state ψ_0 and energy $E[\psi_0] = E_0$:

$$E_0 = min_{\psi \to N} E[\psi] = min_{\psi \to N} \langle \psi | \hat{T} + \hat{V}_{Ne} + \hat{V}_{ee} | \psi \rangle \tag{2.35}$$

For a system of N electrons and given nuclear potential V_{ext}, the variational principle defines a procedure to determine the ground-state wave function ψ_0, the ground state energy $E_0[N, V_{ext}]$ and other properties of interest.

The ground state wave function ψ_0 can be approximated as an anti-symmetrized product of N orthonormal spin orbitals $\phi_i(\vec{x})$, the Slater determinant:

$$\psi(\vec{x}_1, \vec{x}_2, ..., \vec{x}_N) = \frac{1}{\sqrt{N!}} \begin{vmatrix} \phi_1(\vec{x}_1) & \phi_2(\vec{x}_1) & ... & \phi_N(\vec{x}_1) \\ \phi_1(\vec{x}_2) & \phi_2(\vec{x}_2) & ... & \phi_N(\vec{x}_2) \\ \vdots & \vdots & \ddots & \vdots \\ \phi_1(\vec{x}_N) & \phi_2(\vec{x}_N) & ... & \phi_N(\vec{x}_N) \end{vmatrix} \tag{2.36}$$

It can be seen that the form of Slater determinants would lead to the automatically rejection of identical orbitals. Consequently the use of Slater determinants ensures conformity to the Pauli principle i.e. a change of sign when two orbitals are interchanged.

2.2.3 Density Functional Theory

Being the most successful approach to compute the electronic structure of matter, the density functional theory (DFT) has been applied in many scientific field like physics, chemistry, biology and material science. However, it was not considered accurate enough until the 1990s, when the theory were greatly refined to better model the exchange and correlation interaction. In this theory, the properties of a many-electron system can be determined by using functionals (functions of another function which in this case is the electron density). Compared to traditional methods that based on the expansion of the wavefunction in Slater determinants, simplest the Hartree-Fock methods, DFT has relatively low computational costs while it still give results agree well with experimental data. In fact, solving wave function in Hartree-Fock methods provides more information than needed. DFT provides an appealing alternative using electron density to systematically map the many-body system.

In DFT, the electron density is defined as the integral over the spin coordinates of all electrons and over all but one of the spatial variables ($\vec{x} \equiv \vec{r}, s$):

$$\rho(\vec{r}) = N \int ... \int |\psi|(\vec{x}_1, \vec{x}_2, ..., \vec{x}_N)|^2 ds_1 d\vec{x}_2 ... d\vec{x}_N \tag{2.37}$$

It can be obtained that ρ vanishes at infinity and integrated to the total number of electrons:

$$\begin{aligned} \rho(\vec{r} \to \infty) &= 0 \\ \int \rho(\vec{r}) d\vec{r} &= N \end{aligned} \tag{2.38}$$

Experimentally, the electron density $\rho(\vec{r})$ is observable and can be measured by X-ray diffraction.

Thomas-Fermi model

In 1927, the first density functional theory was proposed by Thomas and Fermi[33][34]. Based on the uniform electron gas, the following functional can be used for calculating the kinetic energy:

$$T_{TF}[\rho(\vec{r})] = \frac{3}{10}(3\pi^2)^{\frac{2}{3}} \int \rho^{\frac{5}{3}}(\vec{r}) d\vec{r} \tag{2.39}$$

The energy of an atom is obtained by using a classical expression:

$$E_{TF}[\rho(\vec{r})] = \frac{3}{10}(3\pi^2)^{\frac{2}{3}} \int \rho^{\frac{5}{3}}(\vec{r}) d\vec{r} - Z \int \frac{\rho(\vec{r})}{r} d\vec{r} + \frac{1}{2} \int \int \frac{\rho(\vec{r}_1)\rho(\vec{r}_2)}{r_{12}} d\vec{r}_1 \vec{r}_2 \tag{2.40}$$

In order to determine the correct density to be included in (2.40), they employed a variational principle. They assumed that the ground state of the system is connected to the $\rho(\vec{r})$ for which the energy is minimized under the constraint of $\int \rho(\vec{r}) d\vec{r} = N$

Hohenberg-Kohn theorem

The first Hohenberg-Kohn theorem demonstrates that the electron density uniquely determines the Hamiltonian operator and thus all the properties of the system. Assuming that there were two external potential $V_{ext}(\vec{r})$ and $V'_{ext}(\vec{r})$ differing by more than a constant, each giving the same $\rho(\vec{r})$ for its ground state, the ground-state densities of two Hamiltonians $\hat{H}$and $\hat{H}'$ would be same although the normalized wave functions ψ and ψ' would be different. Taking ψ' as a trial wave function for the $\hat{H}$ problem:

$$E_0 < \langle \psi' | \hat{H} | \psi' \rangle = \langle \psi' | \hat{H}' | \psi' \rangle + \langle \psi' | \hat{H} - \hat{H}' | \psi' \rangle \quad = E'_0 + \int \rho(\vec{r}) [V_{ext}(\vec{r}) - V'_{ext}(\vec{r})] d\vec{r} \tag{2.41}$$

where E_0 and E_0' are the ground-state energies for $\hat{H}$ and $\hat{H}'$ respectively. Similarly, taking ψ as a trial function for the $\hat{H}'$ problem,

$$E_0' < \langle \psi' | \hat{H}' | \psi' \rangle = \langle \psi' | \hat{H} | \psi' \rangle + \langle \psi' | \hat{H}' - \hat{H} | \psi' \rangle \quad = E_0 + \int \rho(\vec{r})[V_{ext}'(\vec{r}) - V_{ext}(\vec{r})]d\vec{r} \tag{2.42}$$

Adding them together, it can be obtained a contradiction that $E_0 + E_0' < E_0' + E_0$. So there cannot be two different $V_{ext}(\vec{r})$ that give the same $\rho(\vec{r})$ for their ground state.

Thus, $\rho(\vec{r})$ determines N and $V_{ext}(\vec{r})$ and hence all the properties of the ground state, for example the kinetic energy $T[\rho]$, the potential energy $V[\rho]$, and the total energy $E[\rho]$.

Kohn-Sham equations

The ground state energy of a system can be written as:

$$E_0 = min_{\rho \to N} \left(F[\rho] + \int \rho(\vec{r}) V_{Ne} d\vec{r} \right) \tag{2.43}$$

Where the universal functional $F[\rho]$ can be split into three parts including the kinetic energy, the classical Coulomb interaction and the non-classical interaction:

$$F[\rho] = T[\rho] + J[\rho] + E_{ncl}[\rho] \tag{2.44}$$

In this formula, only $J[\rho]$ is known while $T[\rho]$ and $E_{ncl}[\rho]$ have to be approximated. The Thomas-Fermi model provides an example of it, however its performance is really bad due to the poor approximation of the kinetic energy.

Kohn and Sham suggested that the approximation can be done by calculating the exact kinetic energy of a non-interacting reference system with the same density as the real, interacting one then compensate it by introducing a exchange-correlation energy:

$$\begin{aligned} T_S &= -\frac{1}{2} \sum_i^N \langle \psi_i | \nabla^2 | \psi_i \rangle \\ F[\rho] &= T_S[\rho] + J[\rho] + E_{XC}[\rho] \\ &\equiv (T[\rho] - T_S[\rho]) + (E_{ee}[\rho] - J[\rho]) \end{aligned} \tag{2.45}$$

Exchange interaction

According to the Pauli Exchange Principle, two electrons have parallel spins will not be allowed to occupy the same orbital. This lead to an effective repulsion between electrons with parallel spins. Thus two electrons not only interact via their charges, but also by their spins.

Correlation interaction

The correlation interaction is also a result of the Pauli Exchange interaction. In this case there is a correlated motion between electrons of anti-parallel spins which arises because of their mutual Coulombic repulsion.

The major problem is is that the functional for exchange and correlation are not known. Many approaches have been developed to approximate the functional. Some of the popular methods are going to be introduced.

The local density approximation (LDA)

The local density approximation (LDA) is the basis of all approximate exchange-correlation functionals.

The central idea of LDA is the assumption that the E_{XC} can be written in the following form:

$$E_{XC}^{LDA}[\rho] = \int \rho(\vec{r})\varepsilon_{XC}(\rho(\vec{r}))d\vec{r} \tag{2.46}$$

where $\varepsilon_{XC}(\rho(\vec{r}))$ is the exchange-correlation energy per particle of an uniform electron gas of density $\rho(\vec{r})$. This energy per particle is weighted with th probability $\rho(\vec{r})$ that there is an electron at this position. The quantity $\varepsilon_{XC}\rho(\vec{r})$ can be further split into exchange and correlation contributions:

$$\varepsilon_{XC}(\rho(\vec{r})) = \varepsilon_X(\rho(\vec{r})) + \varepsilon_C(\rho(\vec{r})) \tag{2.47}$$

The exchange part, ε_X, which represents the exchange energy of an electron in a uniform electron gas of a particular density, was originally derived by Block and Dirac in the late 1920's.

$$\varepsilon_X = -\frac{3}{4}\left(\frac{3\rho(\vec{r})}{\pi}\right)^{\frac{1}{3}} \tag{2.48}$$

No such explicit expression is known for the correlation part ε_C.

The generalized gradient approximation (GGA)

As the LDA approximates the energy of the true density by the energy of a local constant density, it fails in situations where the density undergoes rapid changes such as in molecules. An improvement to this can be made by considering the gradient of the electron density. Thus, the exchange-correlation energy can be written in the following form termed generalized gradient approximation:

$$E_{XC}^{GEA}[\rho_\uparrow, \rho_\downarrow] = \int f(\rho_\uparrow, \rho_\downarrow, \nabla\rho_\uparrow, \nabla\rho_\downarrow) d\vec{r} \tag{2.49}$$

GGA's and hybrid approximations has reduced the LDA errors of atomization energies of standard set of small molecules by a factor 3-5. This improved accuracy has made DFT a significant component of quantum chemistry.

2.3 Analysing quantities

There are quite a lot of different physical quantities can be derived from simulation. To introduce them, all the properties are split into two categories: statical quantities and dynamic quantities in the following sections.

2.3.1 Static quantities

In molecular dynamics simulation, the trajectory output includes the coordinates, velocities of atoms and forces acting on them for each step. Using these quantities, it's possible to calculate some static properties based on given information.

Energy

The energy is an quantity that can be calculated straightforward. The kinetic energy can be obtained from the mass m and momentum p of all particles:

$$E_k = \sum_{i=1}^{N} \frac{|p_i|^2}{2m_i} \tag{2.50}$$

Adding the potential energy U (equation 2.10), the total energy of the system can be calculated $E_{total} = E_k + U$.

Cell parameter and density

The cell parameter defines the size and shape of the cell box. The volume of the cell box can be calculated from the cell parameters. The mass of all atoms were defined before simulation. And in most of the cases, no atom is lost during simulation. Accordingly the density of the system can be calculated straightforwardly by $\rho = \sum_{i=1}^{N} m_i/V$ where m_i is the mass of atom i.

Radial distribution function

The radial distribution function, which basically describes how density varies as a function of distance from a reference particle, is an example of a pair correlation function. It proves to be a effective way of describing the structure of disorder systems such as liquids or glasses. Also, because the RDF can be measured experimentally from x-ray or neutron diffraction methods, it provides a direct comparison between experimental and simulation. In a system where the atoms interact via pairwise

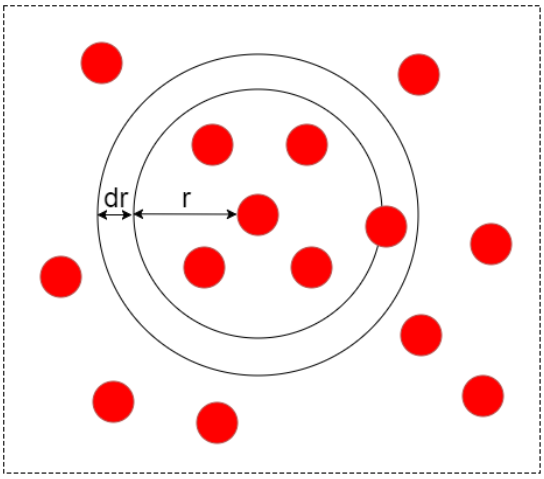

Fig. 2.5 Dashed square represents a simulation box. r is the distance from the central reference atom to the inner cicle. dr is the distance between inner cicle and outer cicle. Shell is defined by combining two circles.

potentials U, the internal energy of system can be obtained by [35]:

$$\langle E \rangle = \frac{3}{2}NkT + \frac{N\rho}{2}\int_V drU(r)g(r,\rho,T) \tag{2.51}$$

where N is the atom numbers, k is the Boltzmann's constant, T is the temperature, $g(r,\rho,T)$ is the radial distribution function.

The approach to calculate the RDF is shown as figure (2.5). Mathematically, the formula g(r) for a single central atom is:

$$\begin{aligned} g(r) &= \frac{n(r)}{\rho V_{ring}} \\ &= \frac{n(r)}{\rho\frac{4}{3}\pi\left((r+dr)^3 - r^3\right)} \\ &\approx \frac{n(r)}{\rho\frac{4}{3}\pi\left(3r^2\right)} = \frac{n(r)}{\rho 4\pi r^2 \Delta r} \end{aligned} \tag{2.52}$$

In which n(r) is the number of atoms in a sphere shell of width Δr at distance r, ρ is the atom density.

Then all the atoms in the system can be treated as the central atoms which result in a total RDF of the system. A example of total RDF calculated for a SiO_2 is shown as figure (2.6)

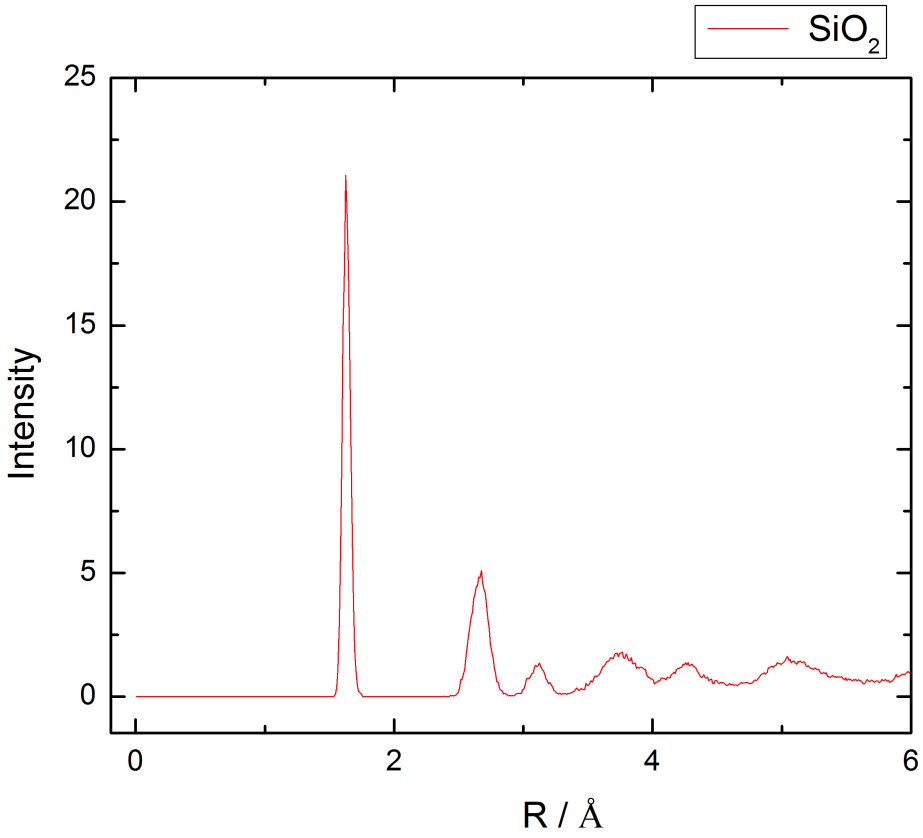

Fig. 2.6 Total RDF of a SiO_2 system.

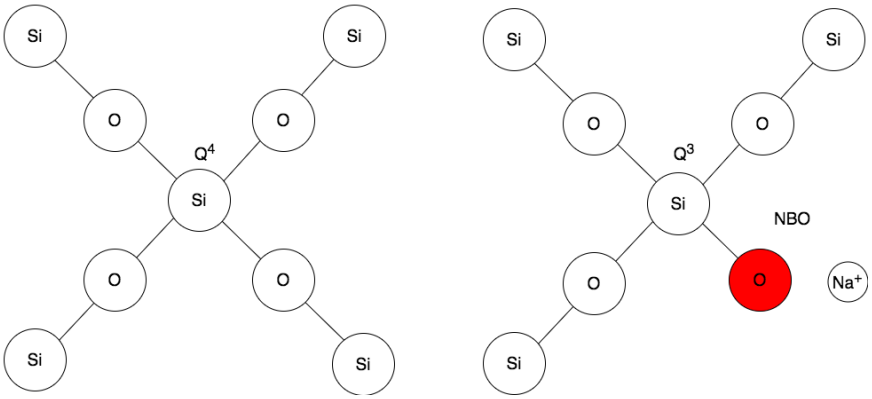

Fig. 2.7 The alkali ion modified the coordination of SiO_4 tetrahedra creating non-bridging oxygen (red).

Q-species and Coordination Numbers

In contrary to crystals, glasses lack long-range order so that standard scattering methods such as X-ray or neutron scattering must be improved to obtain comparable results. While RDF makes possible to determine short-range arrangement in glass structure, exploration of medium-range order may be conveniently performed by calculating Q-species. In experiments, distribution of Q-species can be obtained from nuclear magnetic resonance methods and Raman spectroscopy.

Theoretically, Q-species Q^n is defined by the number n of coordinated bridging oxygen (BO). For instances in silicate glasses, Q^4 stands for the silicon coordinated by four bridging oxygen. By introducing alkali oxides into silica structure, some Si-BO-Si interconnections are broken and non-bridging oxygen are created as shown in figure (2.7).

On the other hand, the coordination number of a central atom or ion can be associated with the number nearest neighbours. In a crystal system, it is clearly determined by the crystalline structure. For example in quartz, the coordination number of silicon would be 4 due to its tetrahedral connection to oxygen. However in a disordered system, it is usually obtained from the radial distribution function g(r). The first neighbour coordination number can be calculated by integral:

$$CN_1 = 4\pi \int_{r0}^{r1} r^2 g(r) \rho dr \tag{2.53}$$

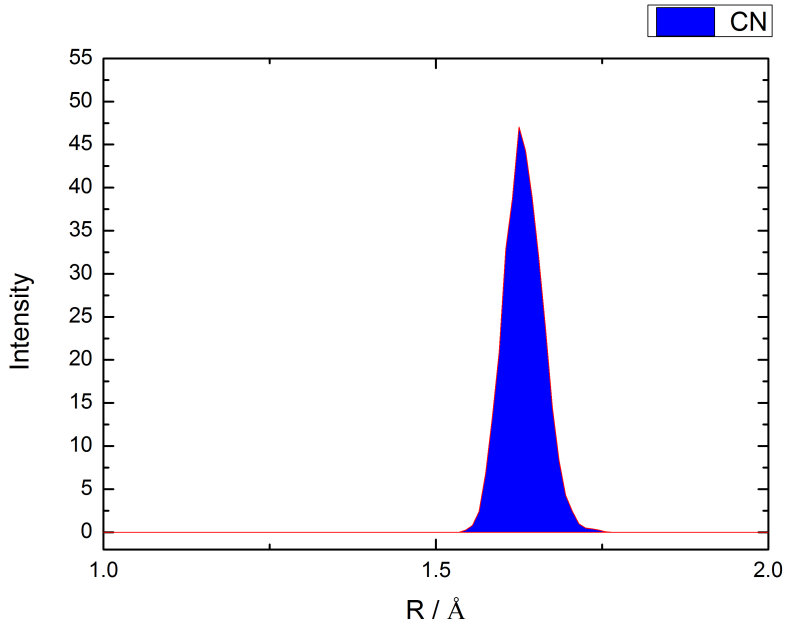

Fig. 2.8 Si-O radial distribution function of a SiO_2 system featuring the first peak. Coloured area indicates the coordination number of Si.

2.3.2 Dynamics

Mean squared displacement and diffusion constant

To analyse the diffusivity of the system, mean squared displacement can be calculated. Mean squared displacement is a measure of deviation over time between the position of a particle and the reference position. The simplest way is to set the reference position on **r**(t=0). Thus the MSD can be obtained by:

$$MSD(t) = \frac{1}{T}\int_0^T \frac{1}{N}\sum_i^N \left\langle (\vec{r}_i(t+T') - \vec{r}_i(T'))^2 \right\rangle dT' \tag{2.54}$$

where T is the totally time to be averaged.

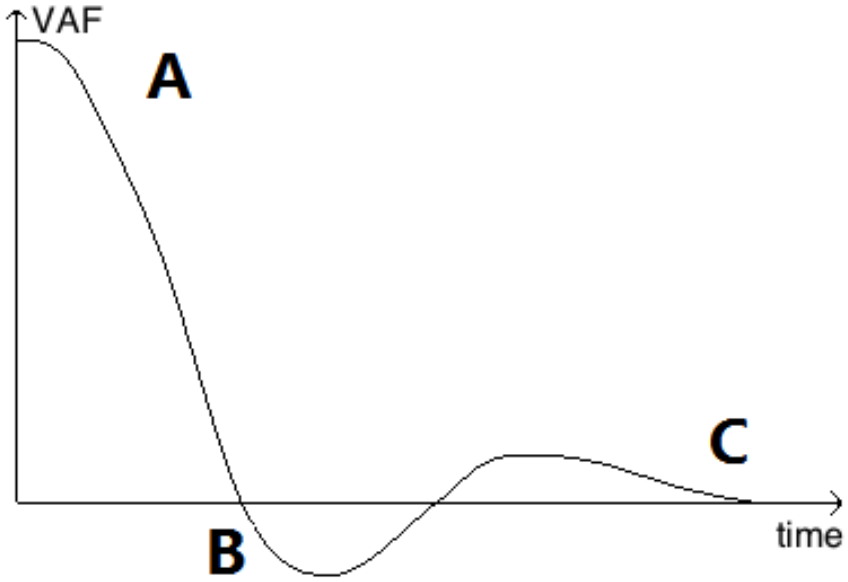

Fig. 2.9 An example of velocity autocorrelation function.

Velocity autocorrelation function

The velocity autocorrelation function (VAF) is a example of time dependent correlation function. It's essential in molecular dynamics because it reveals the underlying dynamical behaviour of system. Given the velocity $\vec{v}(t)$ for the time t, this form of average can be obtained:

$$\langle \vec{v}(t_1) \cdot \vec{v}(t_2) \rangle = \frac{1}{N} \sum_{i=1}^{N} (\vec{v}_i(t = t_1) \cdot \vec{v}_i(t = t_2)) \tag{2.55}$$

which can be written in short notation $\langle \vec{v}(t_1) \cdot \vec{v}(t_2) \rangle$. Therefore the simplest form of velocity autocorrelation function can be written as:

$$Z(t) = \frac{\langle \vec{v}(0) \cdot \vec{v}(t) \rangle}{\langle \vec{v}(0) \cdot \vec{v}(0) \rangle} \tag{2.56}$$

A typical example of VAF result is shown as curve in figure (2.9) where three common behaviour of it are marked out. At mark A, the curve starts with a zero-slope. At mark B, the value of it goes below the zero. At mark C, where $t \to \infty$, the curve shows the asymptotic behaviour.

According to Newton's Laws of motion, the velocity of atoms in the system would be retained if they did not interact with each other. Therefore the VAF would become a horizontal line. So a flat VAF indicates a very weak forces are acting in the system.

On the other hand, if the forces are weak but not negligible, for instance in the gas, it can be expected that the VAF would decrease algebraically, revealing the weak forces slowly destroying the velocity correlation.

In higher density systems like solids and liquids, the forces can be strong. In these cases, the atoms tend to seek the balance between repulsion and attraction due to the energetically reason. These locations are extremely stable in a solid system due to strong forces between atoms thus the atoms are fixed on certain positions. This leads to an oscillating motion of atoms. The VAF of such system would then become a function that oscillates from positive to negative values and back again. However the magnitude would still decay in time due to the perturbative forces. Liquids have a similar behaviour to solids, but now the atoms do not have a fixed location. The diffusive motion would destroy rapidly any oscillatory motion. The VAF therefore would only show one minimum before it decaying to zero. The diffusion coefficient can be obtain by a integral:

$$D = \frac{1}{3}\int_{t=0}^{t=\infty} \langle v(0)\cdot v(t)\rangle \, dt \tag{2.57}$$

Vibrational density of states

Vibrational density of states (VDOS), on which optical and thermodynamic properties depend, is one of the important feature of the solid system. It is well known that in the harmonic approximation, the power spectrum of the velocity autocorrelation is the vibrational density of states[36]:

$$f(\omega) = \mathscr{F}[Z(t)] = \mathscr{F}\left(\frac{\langle \sum \bar{v}_i(0)\bar{v}_i(t)\rangle}{\langle \sum \bar{v}_i(0)\bar{v}_i(0)\rangle}\right) \tag{2.58}$$

Viscosity

The viscosity of a fluid is a measurement that describe how easy it can be deformed by applying the shear stress or tensile stress on it. For liquids, it corresponds to the

concept of "thickness". A fluid that has no such resistance to stress is known as and ideal or inviscid fluid. The zero viscosity known as superfluidity was originally discovered in liquid helium, by Pyotr Kapitsa[37] and John F. Allen.

To model the viscosity of system in molecular dynamics, several approaches can be applied. Three models are going to be demonstrated below.

Einstein relation: A general form of the Einstein equation is:

$$D = \mu k_B T \tag{2.59}$$

where D is the diffusion constant, μ is the mobility, k_B is the Boltzmann's constant, T is the absolute temperature.

In the limit of low Reynolds number, the mobility μ is the inverse of the drag coefficient ς. A damping constant $\gamma = \varsigma/m$ is frequently used for the momentum relaxation time. of the diffusive object. For spherical particles of radius r, Stokes' law gives:

$$\varsigma = 6\pi\eta r \tag{2.60}$$

where η is the viscosity. Thus the Einstein relation results into the Stokes-Einstein relation:

$$D = \frac{k_B T}{6\pi\eta r} \tag{2.61}$$

Alternatively, in melts and glasses the atomic diffusion is generally regarded as thermal activated. The Eyring model is based on absolute reaction rate theory. The Eyring model for viscosity is stated as:

$$\eta = \frac{k_B T}{D\lambda} \tag{2.62}$$

where is k_B is Boltzman constant, T is temperature, D is diffusivity, λ is hopping distance based on the nearest neighbour separation. This has been used in various silicate models to relate the diffusivity of oxygen or silicon to viscosity[38].

Similar to equation (2.57), the viscosity relation can also be derived from autocorrelation function:

$$\eta = \frac{V}{kT}\int_0^\infty dt \left\langle p_{xy}(0)p_{xy}(t)\right\rangle_0 \tag{2.63}$$

Equation 2.57 and 2.63 is called Green-Kubo relation which can be used to directly derive the diffusion and viscosity from the dynamic information of the entire system. The Green-kubo relation of calculating diffusivity can be seen as an equivalent method to MSD approach with higher calculation complexity. Instead, this study is focusing on getting diffusivity and viscosity of individual elements and deriving the total viscosity based on averaging atom fractions according to the composition.

CHAPTER 3

NEPHELINE AND ALUMINO-SILICATES GLASSES

3.1 Introduction: glasses and their nanostructure

The relations between the structure of glasses and their properties are always a fundamental problem of interest in the material science. The first attempt of understanding the molecular structure of glasses can be dated back to 1930s when Zachariasen proposed his Continuous Random network (CRN) [19]. Before that, glass structures were considered to be comprised of nano-size crystals around 20 Å estimated from the x-ray pattern. Zachariasen noted similar mechanical properties can be measured, such as elastic modulus, between crystals and glasses. So the similar structural energies or in other words the atomistic building units (framework cation polyhedra) could be expected. In his model of Silicon oxide (figure 3.1), glasses and crystals have the same building blocks (SiO_4 polyhedra) arranged in different patterns. Generally in the glasses structures, the bond angles of two polyhedra have broader distributions compared to crystals. Also, Zachariasen recognized that certain polyhedra are preferable for forming the disordered networks particular to glass. For instance, oxides like SiO_2, B_2O_3,GeO_2 form glasses, whereas oxides like MgO, Na_2O do not. In fact, based on observations, he proposed four rules for glass formation:

1. An oxygen atom is linked to no more than two cation A.
2. The coordination number (CN) of cation is small, preferably 3 or 4.
3. In the cation-oxygen polyhedra, the cation shares corners but no sides or faces.
4. For three dimension networks, at least three corners must be shared.

Using Pauling's rule [39], it is able to calculate the preferable bonding form between the anion and cation (O^{2-} in this case) which determines the CN. The linking number of cations to oxygen then can be calculated by considering the CN of oxygen and

Table 3.1 Examples of whether an cation-oxide can be glass former

Cation	$CN(O^{2-})$	CN(cation)	Polyhedra sharing	Glass former
Si^{4+}	2	4	four corners	Yes
Al^{3+}	4	6	four corners	No
Mg^{2+}	6	6	edge sharing	No

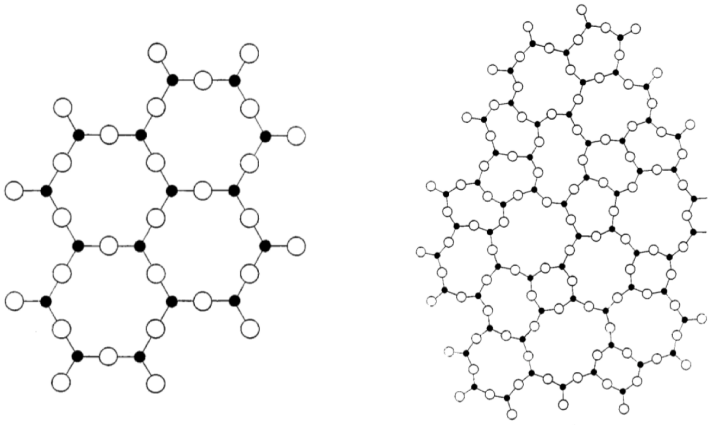

Fig. 3.1 Two dimension example of molecular structure. Left: SiO_2 crystal Right: SiO_2 glass

charges of both cation and oxygen. Some of the results with polyhedra sharing information are shown below in table (3.1).

Therefore since SiO_2 satisfies all the rules stated above it's able to form a glass on its own. A two dimension example of such model is shown in figure (3.1) below. The left structure represents the crystal state of SiO_2 which can be seen as $[SiO_4]$ tetrahedral links to each other and forms the topology with both short range and long range order. Similar to the crystal of SiO_2, the glass on the right is formed by same unit blocks (SiO_4) with topology lacking long range order.

It's known that the glasses can be formed by materials with not only one type of ion. For instance, alkali silicate which contains both alkali ion and Si ion has been widely produced. So obviously there should be a different way of how structure is arranged when a non-glass former is added in to the glass former that lead to some different structure. In fact, the research tell us such Continuous Random Network (CRN) of the glass former would still retained but being modified by the introduced cation. Those ions are called modifiers in these glasses. Using technique of EXAFS and XANES, modifier channels in such Modified Random Network (MRN) has been revealed[22] as shown in figure (3.2). Nanostructure of a sodium silicate is plotted with iso-surface

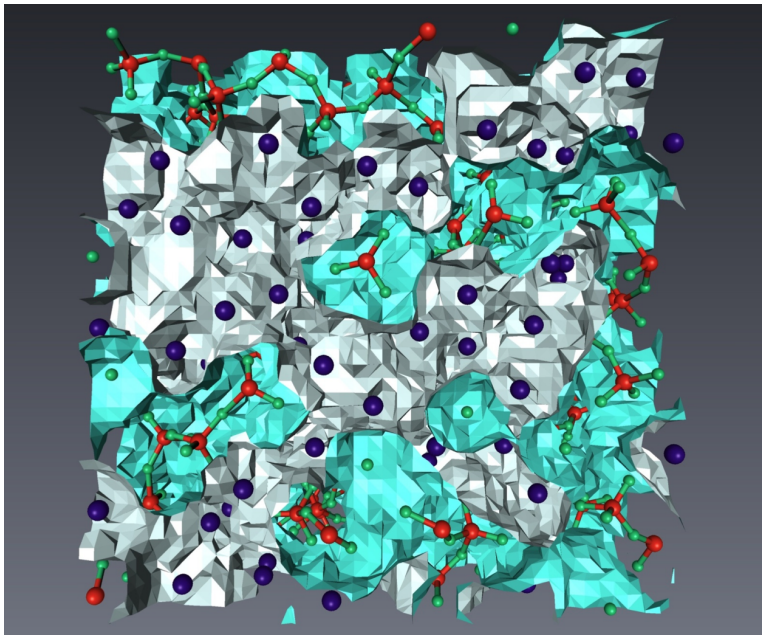

Fig. 3.2 A snapshot showing the Modified Random Network (image courtesy of Zhongfu Zhou and G.N.Greaves with permission). Cyan and white iso-surface mapping out the interaction for framework atoms and modifier cations respectively. Red: Silicon Green: oxygen Blue: Sodium

for interaction enabled. Acting as modifier, the metal ions break down the inter-tetrahedral bonds in silicate structure by introducing the non-bridging oxygen forming the percolation channels through the broken network [22][40][41][42][16][43][20]. Such network results in a considerably low viscosity compare to the CRN.

Aluminium usually exist in many cases of modified random network. They mostly replace the centre of tetrahedron where Si sits at and form the AlO_4^- unit. The deficit charge of AlO_4^- unit would then be compensated by the metal ions. It's well known that in the crystals of silicates and alumino-silicates the distribution of aluminium at centre of the tetrahedra follows a certain principle which was proposed by Lowenstein in 1954 [44]. The rule states that Al-O-Al bonds are forbidden in alumino-silicates minerals for energetic reasons. In this research, natural nepheline $K_XNa_{4-X}Al_4Si_4O_{16}$ was chosen as the glass former for alumino-silicates glass. Due to the 1:1 ratio of Al/Si, according to the Lowenstein's rule, a system with equal amount of aluminium and silicate should form a network with evenly distributed Al and Si atoms in which only Si-O-Al bonds exist. In fact, results can be shown that such distribution rule is violated when glasses are formed due to the compensating role of ions[7]. Thus these alumino-silicates glasses can be described by a Compensated Continuous Random Network (CCRN).

In order to understand the roles both tetrahedral formers Al, Si and metal ions K, Na play in the alumino-silicates melts and glasses, a variety of concentrations of them have been analysed and visualized structurally on an atomic and also nanoscale as well as ion dynamics.

The unit and scale for classical MD simulation

Compared to the experiments, simulations focus on tinier scale in both time and space. A single step in these simulations is usually about 1 fs while the total simulation time is mostly less than 100 ns (as shown in figure 3.3)for molecular dynamics performing on current available computational capacity in this research (roughly hundreds of cores). In order to observe an equivalent behaviour as in real life, the manipulation applied on system are quite often stronger to compensate for the short time. For instance, when a crystal is heated in molecular dynamics simulation, the virtual temperature to actually melt the system would significantly higher than the real melting point measured considering that the structure has to change within a fraction of time.

The lengths of the simulation box are often much less than 1 μm in molecular dynamics (figure 3.3). Typically a 5 nm size of a cubic box contains around a thousand atoms. On one hand it limits the simulation time as well as the size of lattice can be built up to, and on the other hand it give us the advantage of having a more immersive perspective to look into the micro-structure of glasses with the possibility of being able to manipulating it as wanted. In the case of this research on nepheline, such scale of view provides sufficient atomic information of the structure and dynamics while the run time can be within few days for convenience.

The molecular dynamics simulations of this thesis including nepheline, ZIF8 and SOD in later chapters were performed using the DLPOLY classic package [45]. Most of the calculation involved in thesis was performed on HPCWales (a high-performance computer cluster funded by the EU and Fujitsu). In order to perform the molecular dynamics simulation efficiently considering the running time and queuing time, generally 32 cores were used for running normal jobs. For heavy jobs, 64 cores were used. For instance,a normal job of simulating the melting process for nepheline within 0.1 ns lasts about 1 hour.

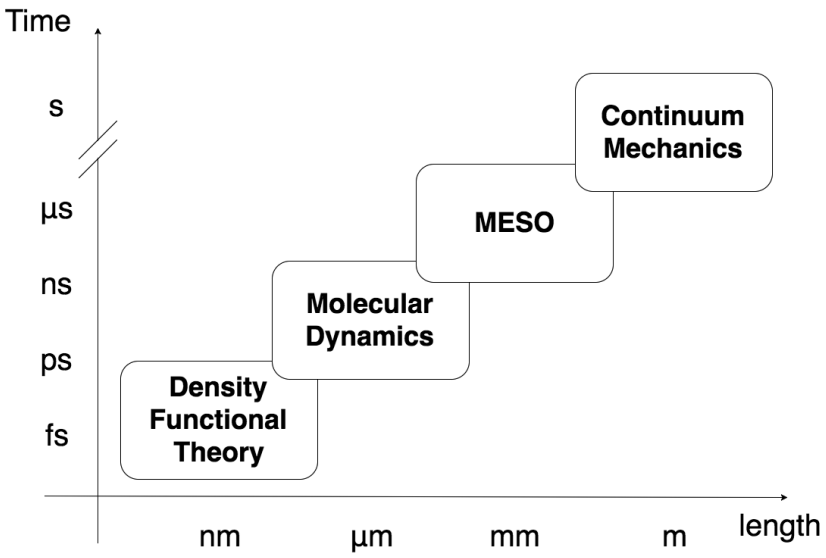

Fig. 3.3 Examples of different simulation methods for a variety of time scale and length scale.

Table 3.2 Cell parameters of nepheline (hexagonal)

Parameters	a (Å)	b (Å)	c (Å)	$\alpha(^\circ)$	$\beta(^\circ)$	$\gamma(^\circ)$
Value	10.050	10.050	8.380	90	90	120

3.1.1 Crystalline structure of nepheline

Figure 3.4 shows the crystalline structure of nepheline $KNa_3Si_4Al_4O_{16}$. The framework species Al, Si and O bond in tetrahedra and form the basic backbone of the crystal. Because nepheline contains equal percentage of Al and Si, the Al distribute evenly with Si according to the Lowenstein's rule. In between the framework atoms, the alkali ions K and Na fill in the pores. Particularly, they have different environment due to the larger ion radius of K. The K ions sit in the larger hexagonal channels while two relatively small Na ions occupies the other type of channels.

In simulation, the crystalline structure of nepheline is described by a unit cell with periodic boundary condition in three dimension. Unlike most of the cases, the unit cell here is not orthorhombic. The cell parameters of a single unit cell is shown below in table (3.2). This unit cell contains 1512 atoms. While larger ensembles could have been used, this would have been unmanageable even with the major HPC resources available for probing dynamics properties like viscosity as a function of temperature which

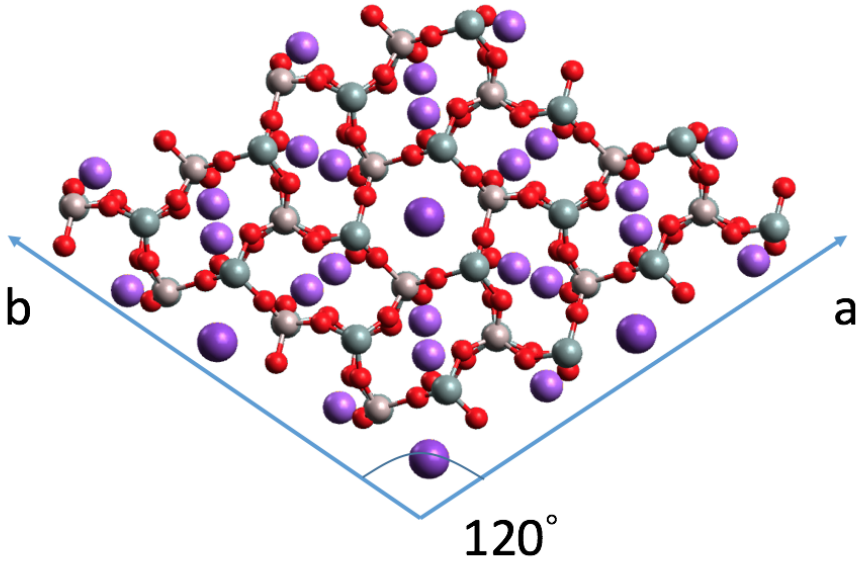

Fig. 3.4 Crystalline molecular structure of nepheline. Silicon distributes evenly with Al as $Al/Si-O_4$ tetrahedra. Mobile ions K and Na occupied the pores/channels creating by framework atoms. K:large purple Na:small purple Si:grey Al:pink O:red

needs to be demonstrated in large time scale (2.3) up to 10 ns for both mobile alkali as well as less mobile network ions like Si, Al and O. Compromises also needed to be made with the respect to thermostats both Berendsen and Nose-Hoover realizations were trailed. In particular, Berendsen thermostat is considered to be efficient over short times thus it was used during heating and quenching processes for producing melts and glasses. However, to accommodate the large time scale needed to derive the diffusion and viscosity, Nose-hoover thermostat was proved the most reliable. Likewise, 48 cores were sufficient for physically realistic simulations that reached the diffusion region even for less mobile network ions that dominate the viscosity (Si,Al,O in this case). While experiments were conducted over the all supercooled range from the molten state to the glass transition, simulations proved practical above 1700K where the diffusion regime can be observed within a realistic amount of simulation time.

3.1.2 Obtaining glasses in simulation

To obtain a simulated glass or amorphous state in simulation, a similar approach to the melt-quenching technique, which is widely used in the glasses factory, was applied.

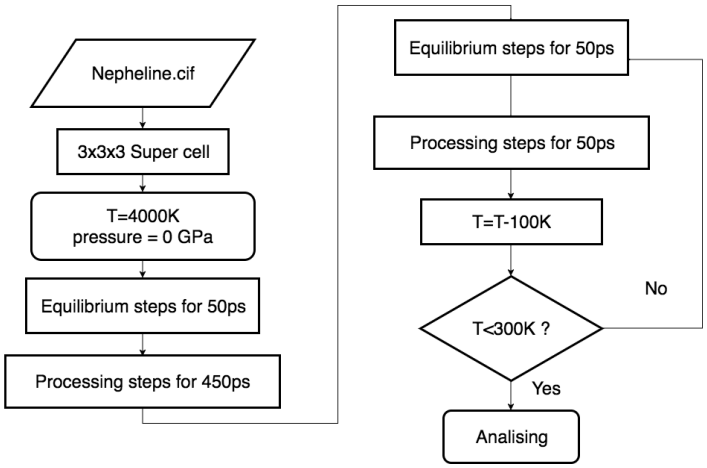

Fig. 3.5 A flow chart of producing nepheline glass in simulation in this study. Instead of a continuous temperature annealing, a multi-step cooling scheme was applied.

The basic idea of it is to heat the materials until the temperature pass above the melting point T_m then quickly cool it down below glass point T_g. The melting point of T_m can be known before from the glass forming crystal. The T_g can be affected by the quenching speed, the faster it quenched the higher T_g would be. Although it follow the same procedure as the real melt-quenching in simulation, the detail of it can be differed in lots of aspects. Firstly, the melting point in simulation would often be much higher than in reality as mentioned in section 3.1 before. Secondly, the cooling speed in simulation can be extremely high which may not even be possible to achieve in reality. This is because in the simulation system, the temperature is controlled by the thermostat with whom abrupt jump of temperature in sudden is acceptable. Accordingly in this research, a multi-step cooling scheme was applied to replicate the effect of continuous cooling. A flow chart of generating such glassy structure for nepheline is shown below as figure 3.5.

As it was shown in the flowchart, the system was heated to 4000K for 50ps in order to get a complete dismantled structure. The comparison between the simulated X-ray diffraction (XRD) of crystal nepheline and 4000K nepheline as well as the cooled down structure is shown below (3.6).

Specifically, the individually sharp peak in the diffraction patten of nepheline crystal indicates the well defined order of the crystal structure. The diffraction pattern of structure at 4000K shows that atoms are moving much more far away from each other due to the heating resulting the peak concentration at very small angle ($2dsin\theta = n\lambda$, $d \to \infty$ so $theta \to 0$). In the cooled structure at 300 K, long range order disappears.

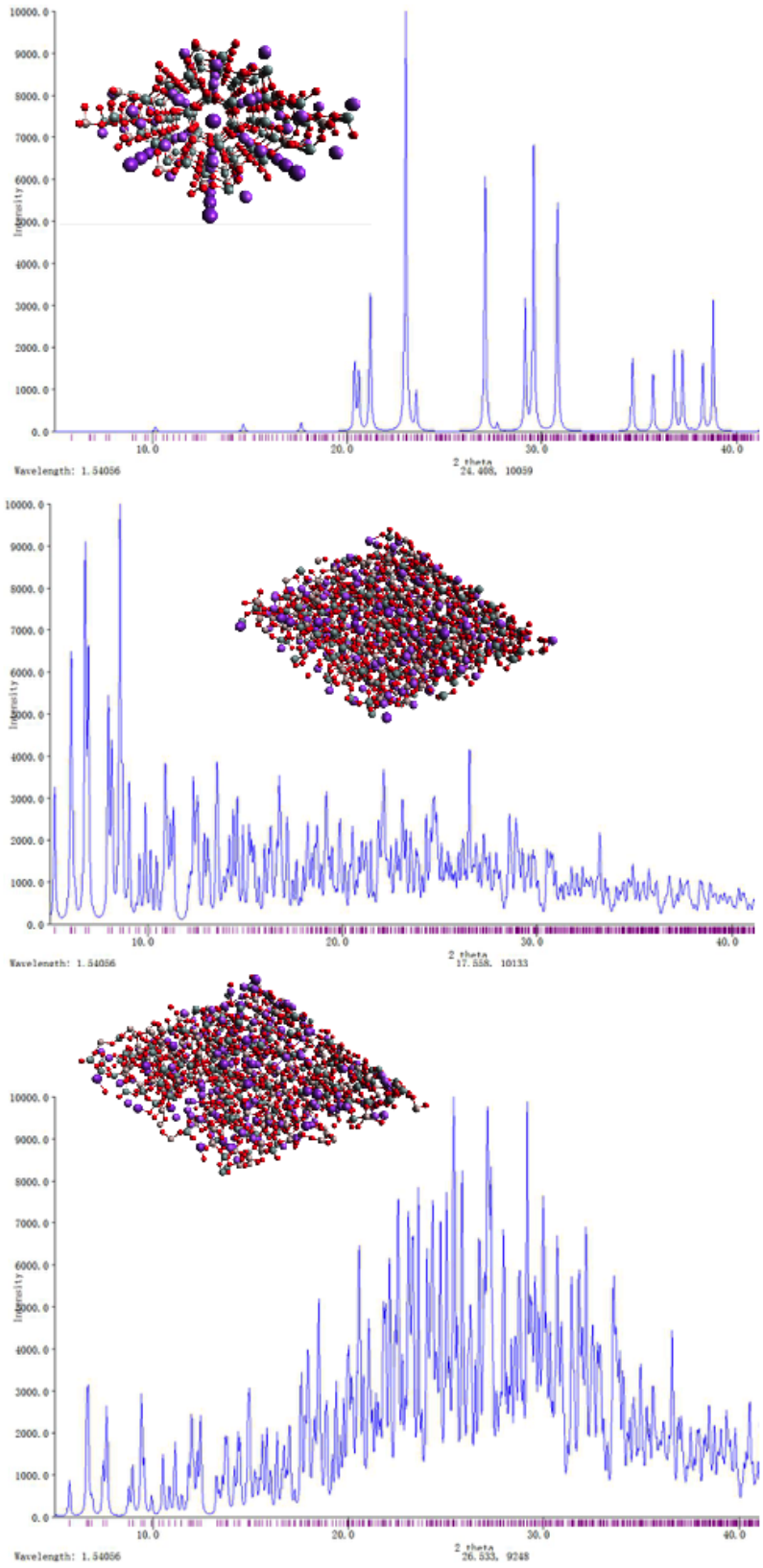

Fig. 3.6 Top: nepheline crystal at 300K Middle: nepheline heated at 4000K Bottom: nepheline cooled down to 300K. Diffraction pattern of nepheline crystal exhibit sharp individual peaks associated with highly ordered structure. The left shifting of peaks in heated structure indicates the extreme expanding of structure. The broad peak of cooled structure is associated with high amorphization in which long range order is lost.

Hence the distance between atoms rearrange by the averaging of potential interaction leading to a broad distribution of peaks.

3.1.3 Interatomic potential

From experience, the key of performing a successful molecular dynamics simulation is to find the best suitable potential for the system. According to the equation (2.11), the total interaction U can be split into three parts: the bonded term, the non-bonded term and the Coulombic interaction. Usually, the Coulombic interaction can be handled by the normal form as it in the equation. The Ewald summation was introduced to compensate the effect of long range interaction of it. The bonded term and non-bonded would be more complicated since they can be quite different depending on the system to be investigated and accuracy needed to be achieved.

In this research, a potential without bonded term is preferable because obtaining glasses requires the dismantlement of the structures thus a bonded potential has to be avoided. For instance, considering two members interaction between atom i and j, the simplest example is a harmonic form:

$$\mathbf{U}(r_{ij}) = \frac{k}{2}(r_{ij} - r_0)^2 \tag{3.1}$$

Where r_{ij} is the distance between atom i and atom j. Such potential would lead to a very strong attraction when $r_{ij} >> r_0$ which makes the connection between two atoms unbreakable. Therefore, the potential should have a convergence at certain distance. This means that the problem left now is to find a non-bonded potential.

The original BKS

BKS (Beest, Krammer, and van Santen) potential is combination of Buckingham potential and Coulombic interaction aiming to describe the interatomic interactions within silicas, aluminophosphates and zeolites[46]. To obtain the parameters, a small cluster of $H_4TO_4(T = Si, Al, P, etc.)$ (shown in figure 3.8) is simulated using ab initio methods [46]. The potential-energy of that cluster was calculated to fit the experimental data on α-quartz.

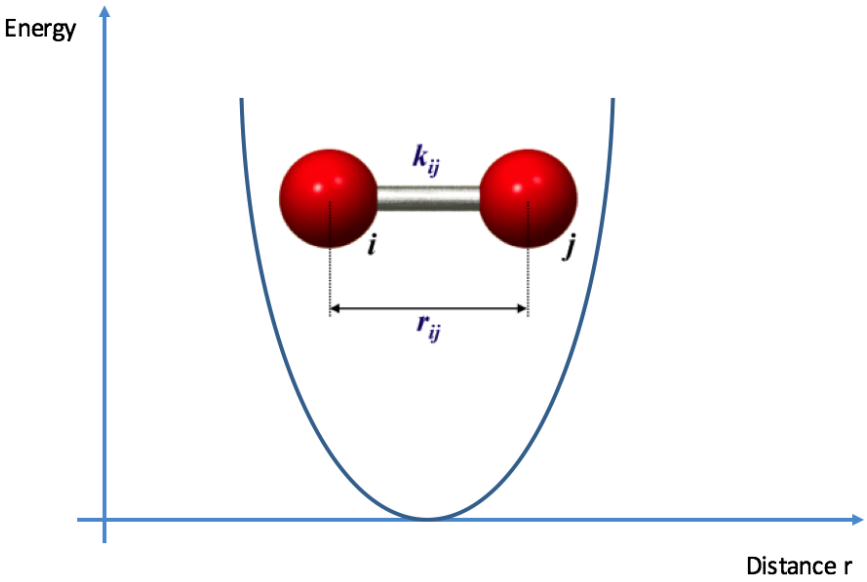

Fig. 3.7 Harmonic potential

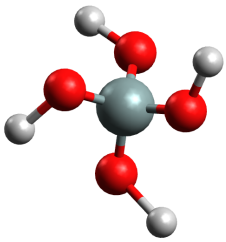

Fig. 3.8 $H_4TO_4(T = Si, Al, P, etc.)$ cluster for calculation

Table 3.3 Parameters of BKS potential

$\alpha_i - \alpha_j$	$A_{\alpha_i\alpha_j}(eV)$	$\frac{1}{\rho}_{\alpha_i\alpha_j}(A^{-1})$	$C_{\alpha_i\alpha_j}(eVA^6)$	Charges q_α
SCF				
O-O	444.7686	2.48513	0.0000	$q_O = -1.1$
Si-O	24441.2370	4.93504	180.8045	$q_{Si} = 2.2$
mixed SCF empirical				
O-O	1388.7730	2.76000	175.0000	$q_O = -1.2$
Si-O	18003.7572	4.87318	133.5381	$q_{Si} = 2.4$
Al-O	16008.5345	4.79667	130.5659	$q_{Al} = 1.4$
P-O	9034.2080	5.19098	19.8793	$q_P = 3.4$
Na-O	3542.2072	4.13455	0.0000	$q_{Na} = 1.0$
Na-Cl	5783.1124	3.11593	521.3348	$q_{Cl} = -1.0$
X_α O-O	551.4486	2.90000	0.0000	$q_O = -1.0$
Si-O	16869.7220	4.86258	124.9962	$q_{Si} = 2.0$

A Table of potential parameters (3.3) is showed below.

As shown in the table that the mixed SCF empirical section almost contain every species needed for the nepheline except the K. The charges of framework atoms (Si, Al, O) have been varied to balance the electrostatic interaction with Buckingham form interaction while the sodium ion's is unchanged. This lead to a non equally shrinking of charges between Si and Al in order to achieve the charge balance $charge_{Al} + charge_{Na} = charge_{Si}$.

Modified BKS

In order to model the system contains K^+ ions, the original BKS is not sufficient so it has to be modified. In this study, a potential used for simulation of low Silica Yttrium Aluminosilicate Glasses [47] is merged with the K-O term from a alkali silicate glasses simulation [48] to cover all the species in nepheline system. For the purpose of amorphization, the potential does not contain any three-body term for angle bonding because it conflicts with the melting process of glass making. The parameters for the modified BKS potential in this work is shown below in table (3.4)

Both potentials share the universal Buckingham form $U = Ae^{-Br} - \frac{C}{r^6}$. The partial charge is evenly shrunk by multiplied the normal charges with $\frac{3}{5}$. In most cases, the partial charges are introduced to avoid the imbalance of pressure and to get rid of three body terms. This can be tested by performing a NVT simulation with ideal volume

Table 3.4 Parameters of modified BKS potential

$\alpha_i - \alpha_j$	$A_{\alpha_i\alpha_j}(eV)$	$\rho_{\alpha_i\alpha_j}()$	$C_{\alpha_i\alpha_j}(eV^6)$	Charges q_α
O-O	2029.2204	0.343645	192.58	$q_O = -1.2$
Al-O	12201.417	0.195628	31.997	$q_{Al} = 1.8$
Si-O	13702.905	0.193817	54.681	$q_{Si} = 2.4$
Na-O	4383.7555	0.243838	30.70	$q_{Na} = 0.6$
K-O	20526.972	0.233708	51.489	$q_K = 0.6$

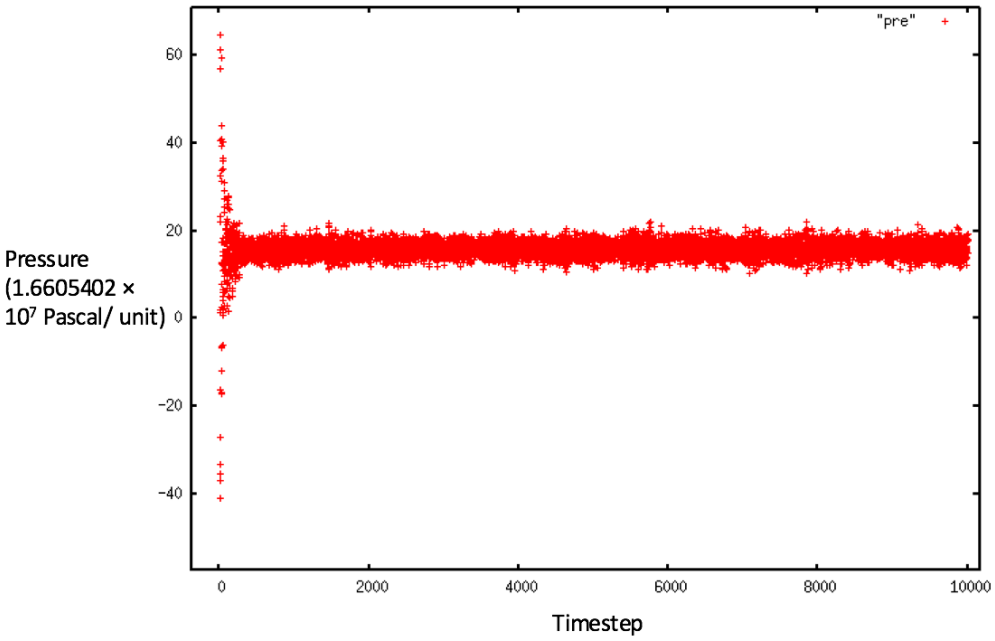

Fig. 3.9 The pressure versus timestep in an NVT simulation

and temperature. It's expected that the value of pressure should be close to zero. A graph (3.9) below shows the pressure variation during 50ps of NVT simulation.

According to the graph, the systems has a pressure around 0.3 GPa (15.84 in DLPOLY unit showed in figure 3.9) when the volume was fixed at measured value. In consequence, presumably the structure obtained with the potential is going to be slightly expands after releasing the restriction on volume.

Potential performance

One of the most important measure to validate the force field is duplicating the experimental crystal structure in simulation. Commonly, the crystallographic structures

Table 3.5 Structure optimization for super cell

	a (Å)	b (Å)	c (Å)
non-optimized	30.150	30.150	25.140
optimized	30.488	30.488	25.422
pressure compensated	30.157	30.157	25.146

from experiments were used as the initial atomic coordinates. NPT ensemble of room condition were then applied to get the optimized crystal structure. A table (3.5) below shows the difference between non-optimized structure and optimized structure. A compensated pressure was used to get the ideal structure base on the experimental measurement.

3.2 Result of glasses

Radial Distribution Function

To obtain the structure information of cooled glasses, a series of NPT simulation was performed to extract the radial distribution functions. Data points were collected through 100 ps of NPT simulation with a 10 fs interval. Five different K concentrations (K/(K+Na) = 0%, 25%, 50%, 75%, 100%) have been simulated for comparison.

The blue curve in figure (3.10) shows the total radial distribution functions of $KNa_3Al4_Si_4O_{16}$. The first and second peaks which correspond to the most probable bond distances of Si-O and Al-O, are equal to 1.67 and 1.80 Å respectively. These numbers are in good agreements with the measurements (Si-O = 1.64, Al-O = 1.78) [49]. Since K^+ has a larger ion radius than the Na^+ while they both have same charge of 1+, the preferable bond length of K-O is slightly larger than the Na-O shown as in curves at bottom in figure (3.10).

3.2.1 Percolation channel

Figure (3.12) below contains the molar volume obtained from both MD simulation and experiments. Overall, the molecular dynamics result successfully replicated the molar volume.

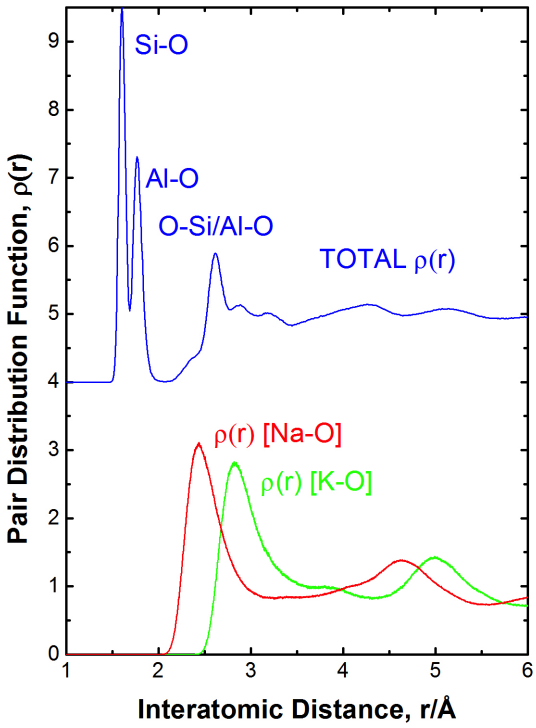

Fig. 3.10 Blue: total RDF with a offset of 4. Peaks ascribed to certain atom pair distance are marked out. Red: RDF of Na-O Green: RDF of K-O

Elements	K	Na	Si	Al	O
Ionic radii	1.64 Å	1.24 Å	0.25 Å	0.43 Å	1.36 Å

Fig. 3.11 Table of ionic radii

As mentioned in previous chapter, the alkali inside of alumino-silicates can form channels within the frameworks. When a channel occurs from one side to the other through the whole cell, it is called a percolation channel. Having less field strength than Na^+, the bigger ion K^+ would presumably be easier to achieve percolation. Therefore changing the concentration of K^+ would affect the forming of those percolation channels. To support this contention, a quantity is necessary for determining the forming of channels. Accordingly, the percolation threshold for octahedral systems can be derived to measure the existence of the channels. It reflects the amount of ions that should exist to be able to form the percolation. Assuming the ions can be simplified as spheres, the volume of individual alkali ion is calculated by $V = \frac{4}{3}\pi r^3$ where r is the radius of ion. Table (3.11) shows the radius of different ions in the system.

Then the critical value for percolation can be calculated by :

$$\begin{aligned} \xi &= \frac{V_{ions}}{V_{box} - V_{framework}} \\ &= \frac{\sum \frac{4}{3}\pi r_{ion}^3}{L^3 - \sum \frac{4}{3}\pi r_{framework}^3} \end{aligned} \tag{3.2}$$

For instance, to replace the spheres with octahedral units, it can be derived that the critical point for percolation would be around 25.2% [50]. The blue dots in figure (3.12) represents the ξ for both K and Na combined. In the system of nepheline, it correspond to the 68% concentration of the K as shown in figure 3.12. (I am endebted to Prof. Greaves for this argument.)

These percolation channels can be shown in the molecular dynamic shots below cropped from software VMD. The radii used for Na^+ and K^+ are ionic radii. In both d and e, the percentage of K which, together with sodium, occupy a total volume that surpasses the critical percolation threshold ξ_c indicate percolation channels that are created. Since K^+ has larger ionic radii than Na^+, the percolation becomes to be more

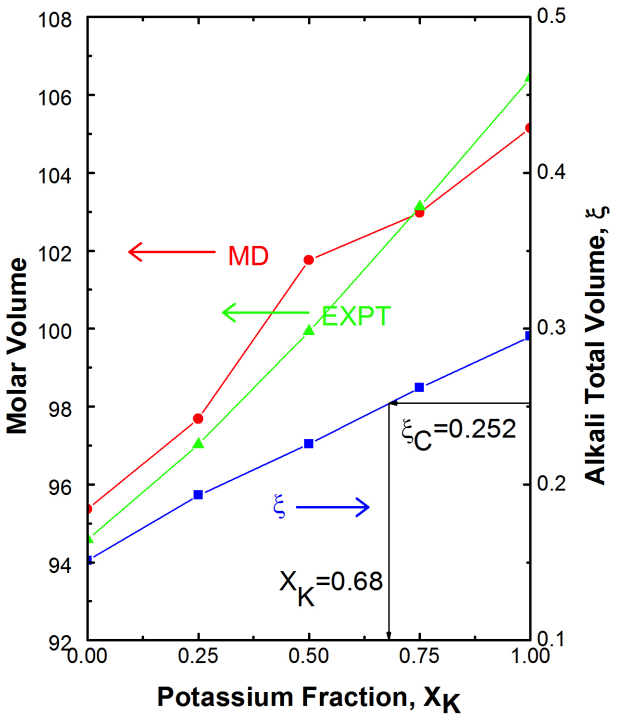

Fig. 3.12 Molar volume as a function of K concentration: molecular dynamics (red), experiment [Charles Lelosq] (green). Alkali volume fraction (equation 3.2) is shown in blue. The critical value of ξ_c relates to the percolation threshold for octahedral unit [50].

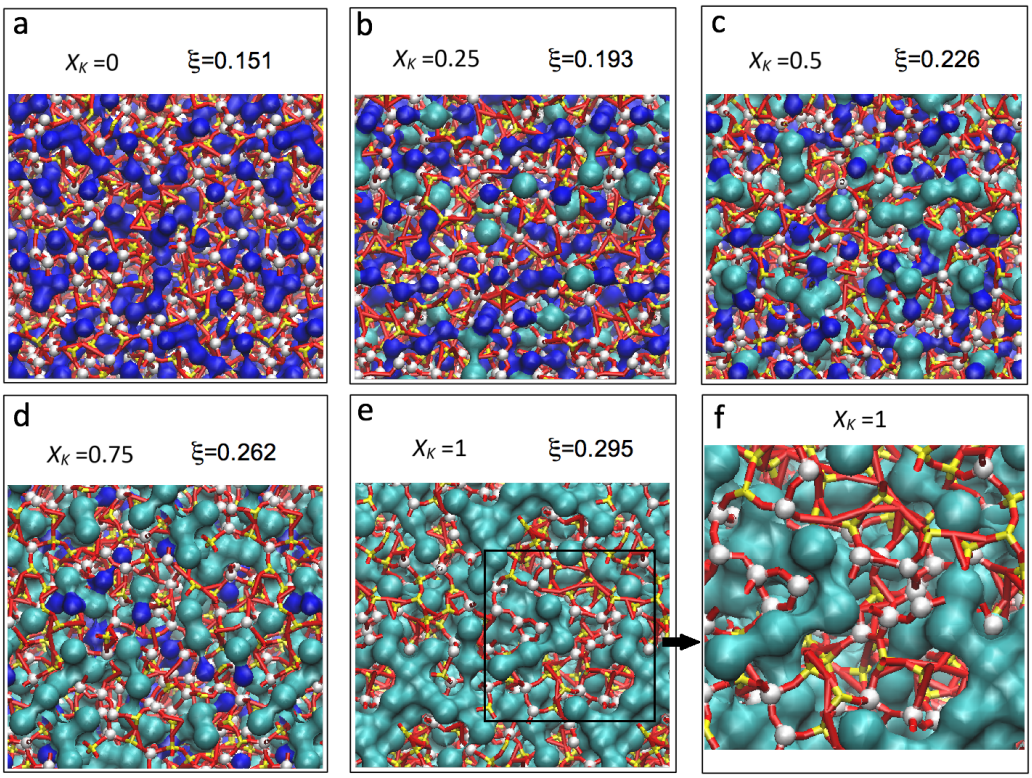

Fig. 3.13 Six snapshots taken on different concentration of K. Overall, the scale of segregation increases as the K concentration increase. This leads to a percolation of ion channel forming at around 75 % (figure 3.12). Final figure shows a zoom-in for 100 % K. White balls represent the Al atoms. It is clear that the segregation of K ions affects the framework structure. In particular, Al atoms segregate around percolation channels breaking the Lowenstein's rule that forbids Al-O-Al connection.

and more dominated by K^+ after the percolation threshold at 68% which eventually lead to a pure K^+ percolation channel.

Evidence for the violation of Lowenstein's rule

The forming of ionic percolation channels certainly affected the topology of frameworks atoms. While the Lowenstein's rule is found to be consistent in crystal aluminosilicates as demonstrated in previous session, the molecular dynamics snapshots of nepheline glasses (3.13) shows the violation could happen. Using ^{17}O NMR measure-

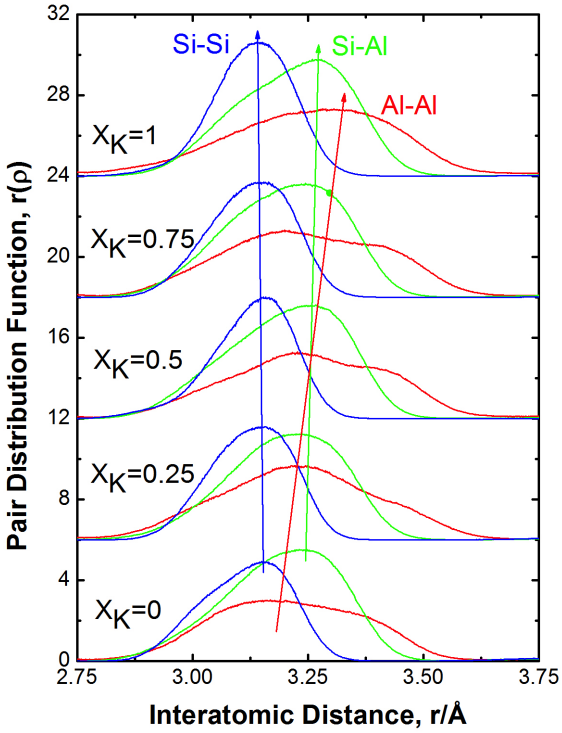

Fig. 3.14 Radial distribution functions for Si-Si, Si-Al, Al-Al correlation. The areas below the curves are associated with the percentage of different T-O-T bond exist in the system. This suggests that around 30 % of the Al-O-Al bonds can be observed in the system indicating the violation of Lowenstein's Rule.

ments [7], recent research states that such deviation can be found in aluminosilicate glasses.

To quantify the violation and the effect of K concentration, a series of RDF was measured. Figure (3.14) shows five pair distribution functions that correspond to the framework atoms Si,Al. The X indicates the ratio of $K/(Na+K)$ in the simulation cell. The peaks of Si-Si and Si-Al barely changed with the increasing composition of K^+ ions exist in the system. Distinguishably, the Al-Al function appears to have a right shifted peak as well as a broader Al-Al bond distribution. By measuring the area below it's possible to calculate the percentage of different bonds existing in the system. Overall the Al-O-Al bonds appearing around 30% of total without considerable change for all compositions.

The violation of Lowenstein rule can be clearly observed as shown in figure 3.13 f. Large K ions segregate and form several percolation channels within the structure. This also affects the topology of framework atoms. In particular, the Al-O-Al bonds appear alongside with the segregation channels.

3.2.2 Dynamic properties

Mean Squared Displacement and Diffusion constant

Calculating the diffusivity from simulation can help us understand the dynamics information. Mean Squared Displacement measures the squared distance that atoms travelled during a certain amount of time. It can be calculated straight forward from the trajectories of simulation using following algorithm:

$$MSD \equiv \left\langle \Delta\vec{r}(t)^2 \right\rangle \equiv \frac{1}{N}\sum_{i=1}^{N}(\vec{r}_i(t) - \vec{r}_i(0)) \tag{3.3}$$

Given a certain amount of time, the further atoms travelled means the higher diffusivity they have, and the distances of them would have travelled are hugely affected by their velocity thus the system temperature. So although atoms are still moving at low temperature, they mostly swinging around the equilibrium positions. Because of the limitation on time scale that can be performed through molecular dynamics simulation, the temperature of the system must be high enough to reach the diffusion process. In this study, the melts of nepheline and variations were studied at 2000K which is above the T_g. A plot containing mean squared displacements of Si/Al/O is shown below as linear and log-log representations (figure 3.15). In the log-log plot, three regions can be identified:

I. Ballistic region where ions oscillate within the same interatomic potential II. Transition region where the mean square displacement increases more slowly with time. III. Diffusive region where ions move to adjacent sites and beyond.

Mathematically, the movement of individual atom can be seen to be a good approximation to a random walk. Famously analysed by Alber Einstein in the study of Brownian

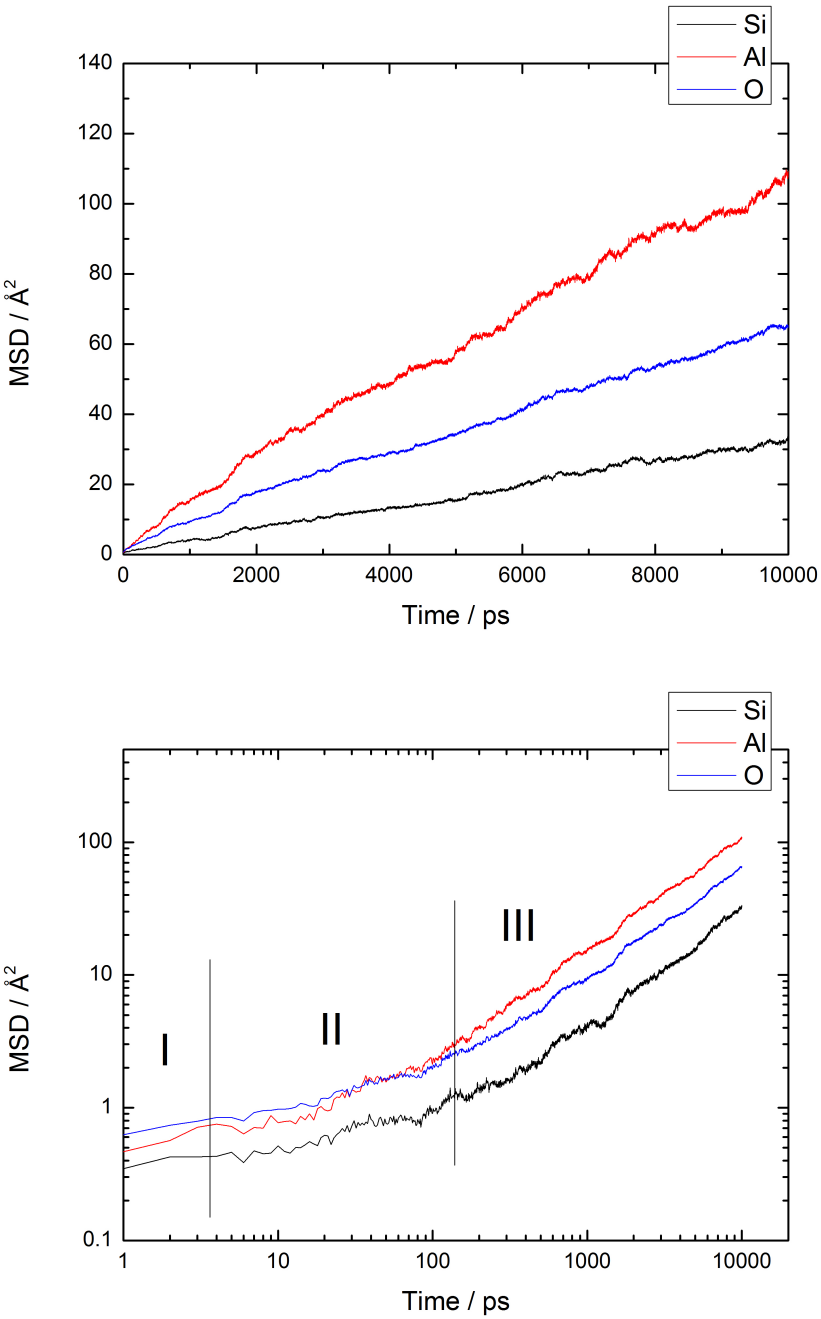

Fig. 3.15 Mean squared displacement of Si/Al/O versus timestep at 2000K shown as linear plot (top) log-log plot (bottom) with three marked regions. Diffusion constant can be derived from the slope of the diffusive region. (equation 3.4)

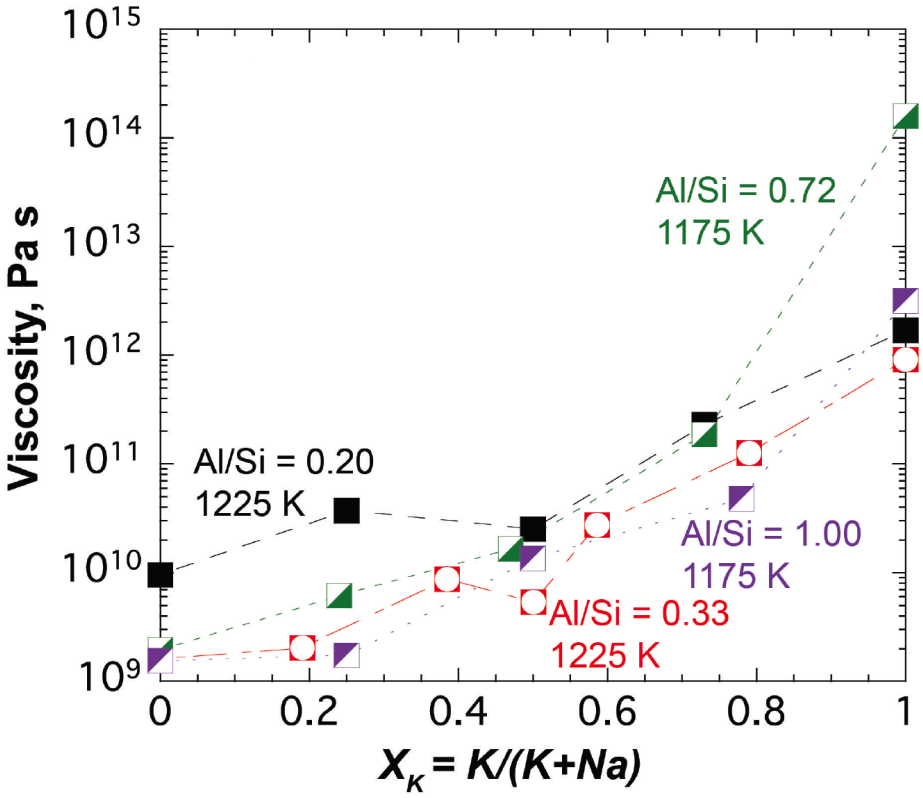

Fig. 3.16 Experimental measurements of viscosity of nepheline including different Al/Si concentrations. (Charles Lelosq, Australian National University)

motion, the relationship between the self diffusion coefficient D and MSD can be written as :

$$\left\langle r^2 \right\rangle = 6Dt + C \tag{3.4}$$

Where $\left\langle r^2 \right\rangle$ is the mean square distance and t is the time.

The slope of MSD is derived for calculating the diffusion constant. Accordingly diffusion coefficient can be derived from dividing the slope by 6. According to the plot, diffusion coefficients of different atom species follow the sequence: Na>K»Al>O>Si. This is due to the strong bonding between framework atoms that limits the diffusion.

Table 3.6 The hopping distance of elements derived from radial distribution function (T = 2000K)

	K	Na	Si	Al	O
hopping distance (pm)	334	343	316	333	266

3.2.3 Predicting the non-linear viscosity behaviour

In experiments, the viscosity can be measured by the drag of anti-rotation concentric cylinders at high temperatures using creep methods [51]. On the other hand, the viscosity can be derived empirically from the diffusion constant of the system. There are two formula describe the relation between diffusion constant and viscosity. The Stokes-Einstein law gives the viscosity by only taking the temperature and radius of particles into account:

$$\eta = \frac{k_B T}{6\pi D r} \tag{3.5}$$

while the Eyring relation [38] consider the hopping distance λ of particles:

$$\eta = \frac{k_B T}{D\lambda} \tag{3.6}$$

The distance λ is estimated from the first neighbour distance which can be derived from the Radial Distribution Function.

In comparing experimental determination of diffusion and viscosity the Eyring equation predicts the best correspondence for silica melts [38].

In previous section, the diffusion coefficient of each elements was derived from the mean squared displacement. Total diffusivity is dominated by the diffusivity of mobile alkali cations coming from the channel structure. The partial diffusivity of different elements are converted to partial viscosity values. Then for each elements, there would be a corresponded 'partial viscosity'. These can not be measured directly from experiments. But from calculations it provides insights into the different contribution anion and cation makes to the total viscosity in where the dominant species come from the network (Si, O, and Al). In this study the total viscosity is the average value weighted by the number percentage of every atom species. This is the assumption being made for deriving the total viscosity.

The total viscosity dependence on K^+ concentration shows an sharply increase at around 75% X_K close to the percolation threshold 68 % (3.17). This is confirmed

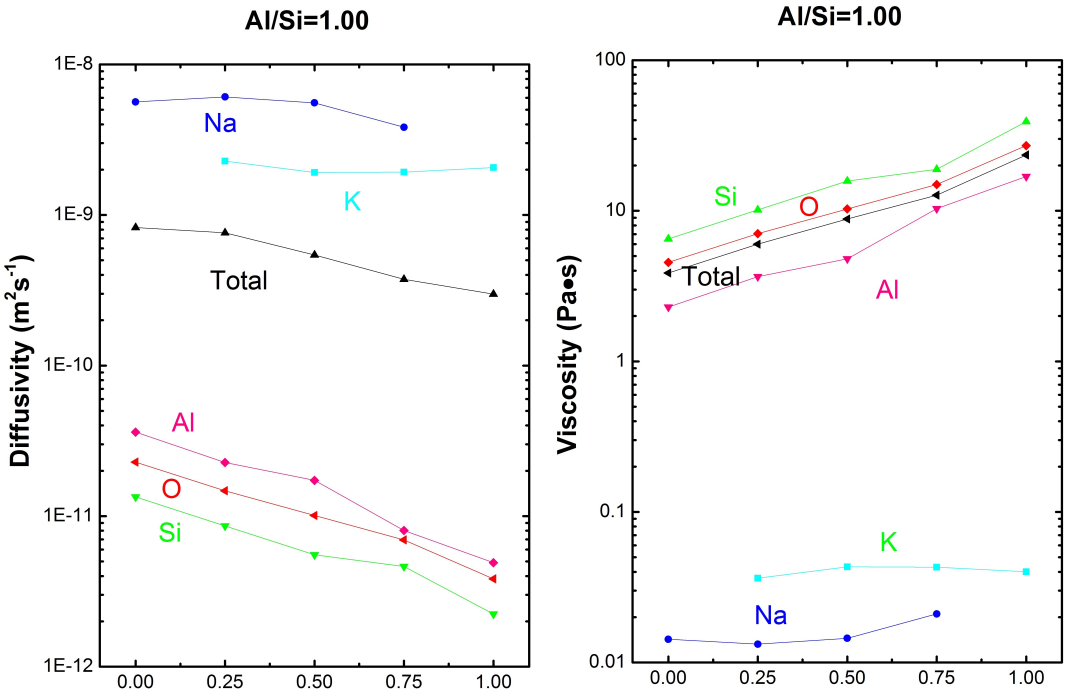

Fig. 3.17 Diffusion coefficients deriving from Mean squared displacement for Al/Si = 1. Viscosity calculated by Eyring relation. Plots exhibit that the dominant species for diffusion (Na, K) and viscosity (Si, O, Al) are different.

by experiment in which similar rising appear at high K^+ concentration 3.16. The total viscosity of system is almost identical to the partial viscosity of oxygen. This is due to the large amount of slow moving O existing in the system. Hence when the concentration of alkali is changing, the contributions for viscosity are mainly from oxygen and other two less mobile framework atoms Si and Al instead of alkali ions. This explain the abnormal non-linear increasing behaviour compared to symmetrical conductivity minimum curve (chapter 1, figure 1.12) found from typical mixed alkali effect in silicate glasses. This explains the non-linear viscosity behaviour also occurs in diffusion but with the decrease occurring around the percolation threshold (3.12).

To establish whether the non-linear increasing of viscosity occurs for different compositions, two other alumino-silicates with different Si/Al ratio (Si/Al= 0.33 figure 3.18 and Si/Al= 0.6 figure 3.19) were also simulated where similar behaviour differentiating alkali dominating diffusivity and network ions dominating viscosity.

However, there are quantitative differences as function of Al/Si ratio. Figure (3.20) shows that the more Al that is present the more population of alkali the more exaggerated the non-linear behaviour in K^+/Na^+ above the percolation threshold for nepheline. This suggests that percolation channels are more prevalent the more Al ions are present. This scaling behaviour is qualitatively in agreement with experimental viscosity measurements figure (3.16). Detailed differences between theory and experiments in viscosity magnitude are expected as the simulations came out from 2000K compared to experiments at 1175K.

A fitting model for viscosity ranging from 2000K to 1000 K based on Adam-Gibbs theory is given below as figure 3.21. It includes the simulated total viscosity value as well. A good agreement between models and simulations at 2000 K is found.

Raman spectroscopy and Vibrational density of states

The experimental Raman spectroscopy of nepheline with different alkali mixtures is shown in fig (3.22). There are four features highlighted that range from stretching through bridging oxygen bending to low frequency Boson peak. In between, there are sharp features D1 and D2 attributed to four and three fold rings respectively. [52]. All of these features become more prominent with the increasing concentration of K.

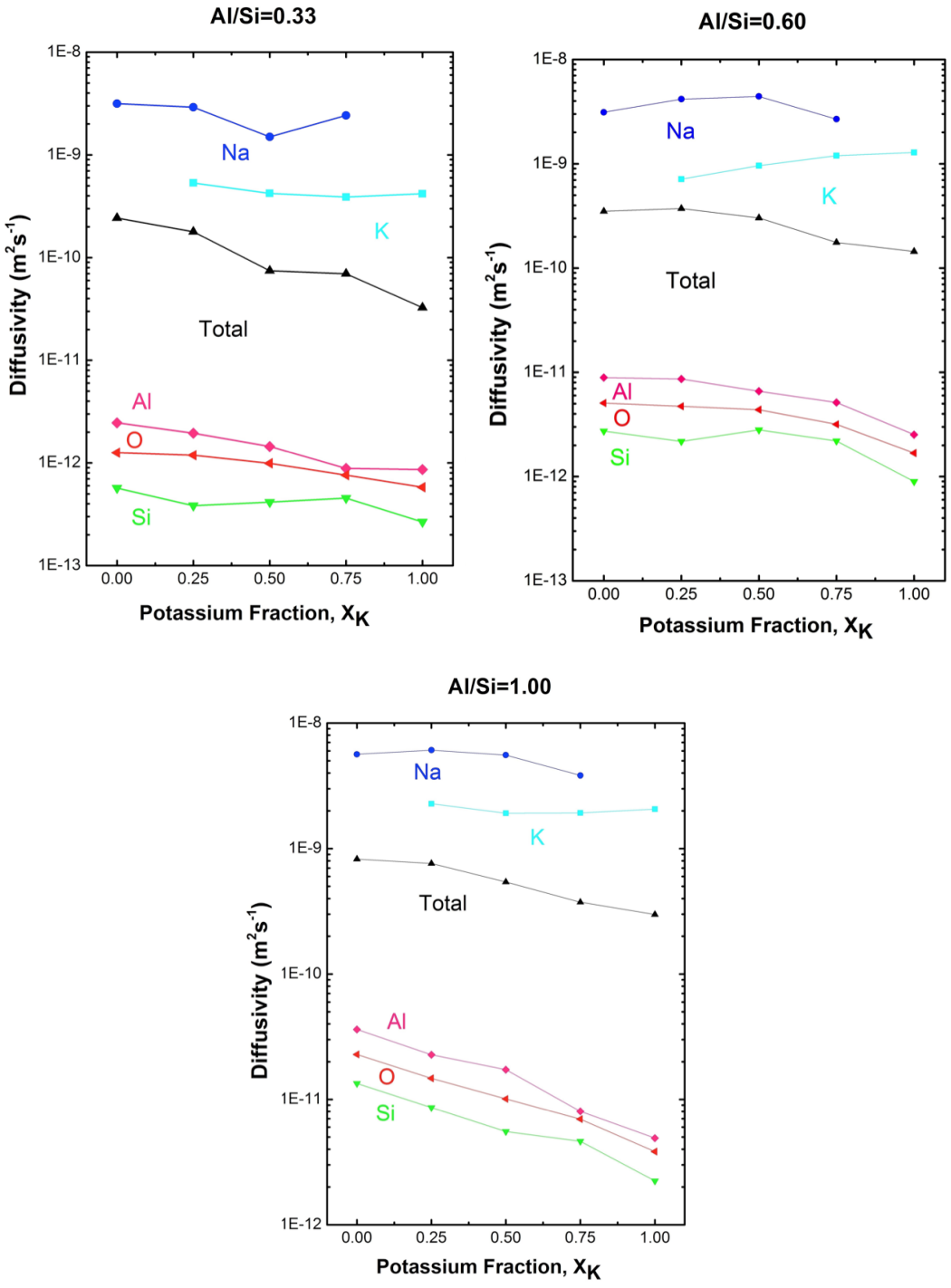

Fig. 3.18 Diffusivity for all three Al/Si ratio (0.33, 0.6, 1). Diffusion coefficients for all atom species are obtained by Mean squared displacement methods. Total diffusivity is based on individual diffusivity average on atom numbers.

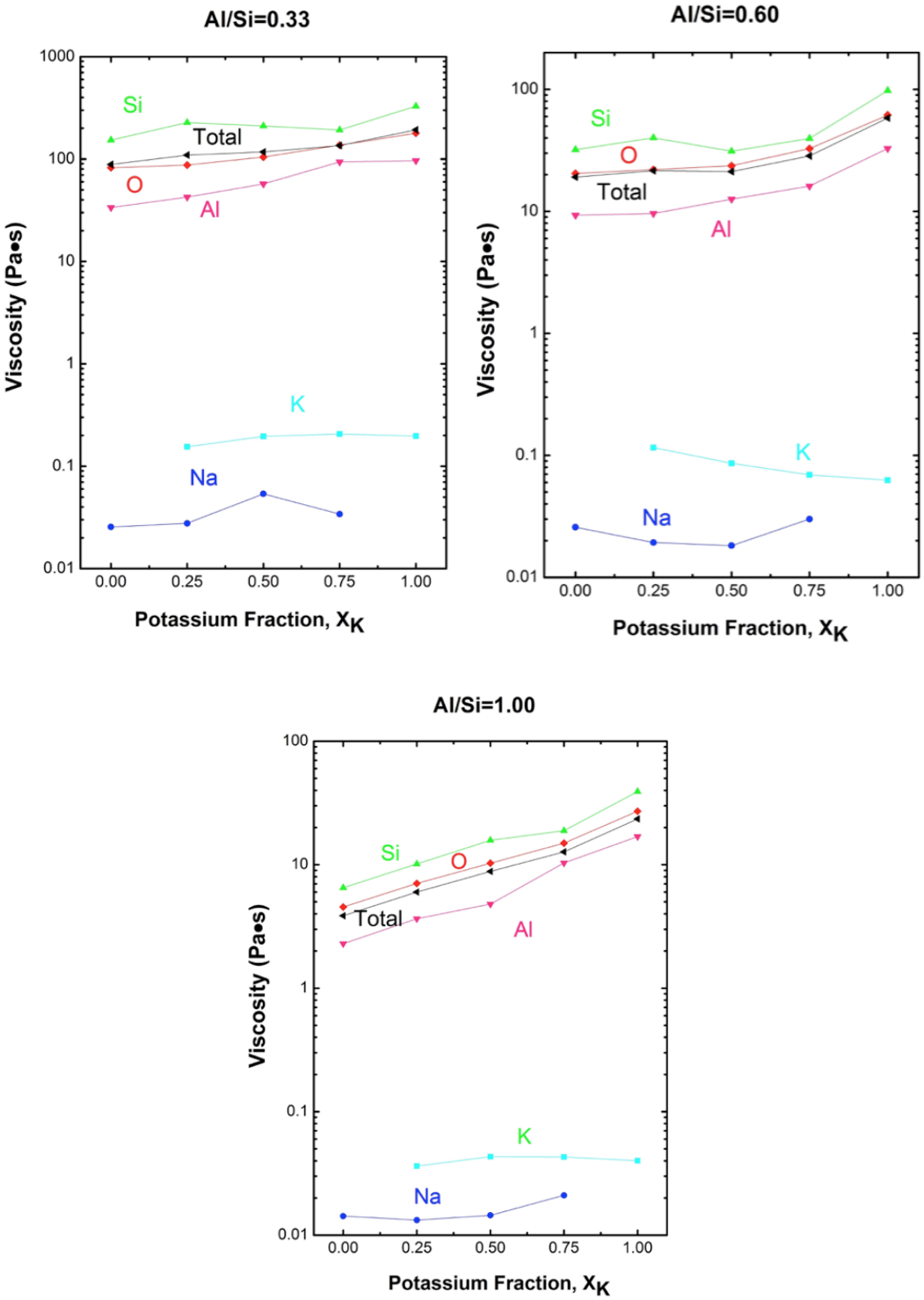

Fig. 3.19 Viscosity for all three Al/Si ratio (0.33, 0.6, 1). Total viscosity is based on individual viscosity average on atom numbers. Total viscosity is dominant by the slow moving framework atoms.

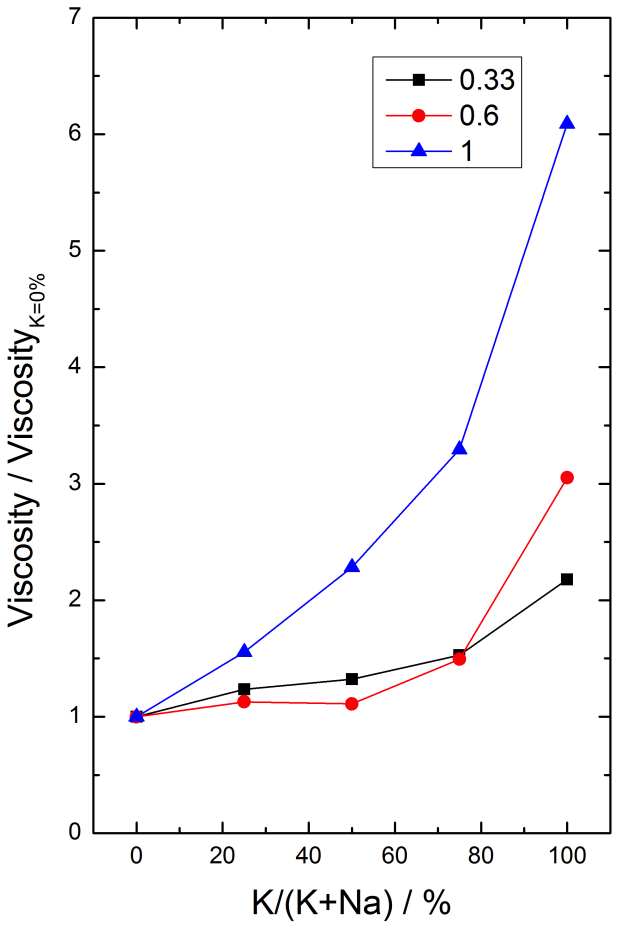

Fig. 3.20 Viscosity simulated at 2000K for nepheline melts with three different Al/Si compositions (0.33, 0.6, 1). Values have been normalized to exhibit the changing.

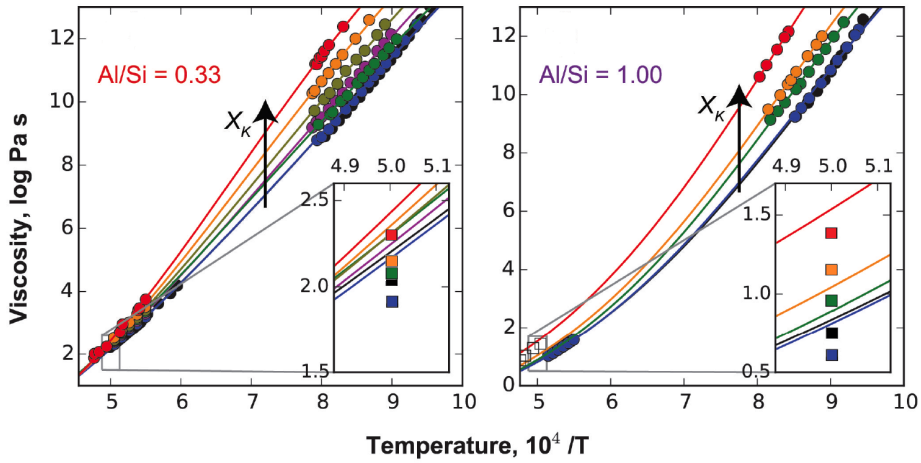

Fig. 3.21 Curves of viscosity predicted by a fitting model of Adam-Gibbs theory [Charles Lelosq, Australian National University] ranging from 2000 K to 1000K. The viscosity increases as temperature decreases. Squared points are associated with the simulated total viscosities. Difference between simulation and model is within half of decade.

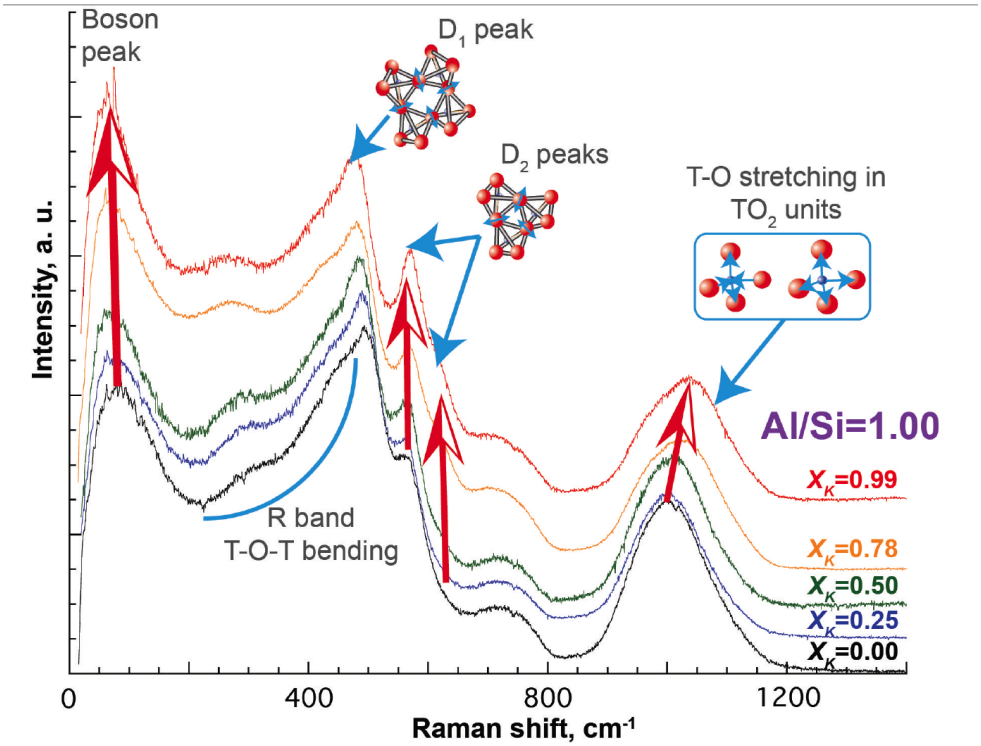

Fig. 3.22 Raman spectroscopy of nepheline glasses. Some major peaks are marked out in the plot. The peak at lowest wavenumber is ascribed as boson peak associating with collective liberations between adjacent tetrahedra. The D1 peak and D2 peak correspond to four fold ring and three fold ring respectively. The peak at high wavenumber around 1000 cm^{-1} is ascribed to Al/Si-O stretching.

To obtain the equivalent information as Raman spectroscopy, Vibrational density of states (VDOS) can be calculated through MD simulations. VDOS is derived from the Fourier transform of the Velocity Autocorrelation Function (VAF). Molecular dynamics with Verlet methods provides us the full information of velocity at each time steps. Therefore it's possible to calculate the VAF from the velocities of all atoms following the trajectory. VAF reveals the underlying nature of the dynamical processes operating in a molecular system. It is one of the prime example of time dependent correlation function, The approach for calculating the VAF can be constructed as follows.

Assuming a starting timestep t=0, velocity v(t=0), the length of each timestep Δt, the VAF can be defined as :

$$C_v(t = n\Delta t) = \frac{1}{N}\sum_{i=1}^{N}(v_i(t = t_0) \cdot v_i(t = t_0 + n\Delta t)) \tag{3.7}$$

or for short

$$C_v(t) = \langle v_i(0) \cdot v_i(t) \rangle \tag{3.8}$$

VDOS is obtained by Fourier transforming of the VAF from the time domain to the frequency domain.

Similar features to experiments can be seen in VDOS (3.23) with slight differences that can be attributed to transition matrix elements terms are operating in the Raman processes. The first peaks around $100cm^{-1}$ are typical boson peaks for glasses. As the K composition increase, the boson peak rises as well. A similarly rattling peak around 200 cm^{-1} due to alkali motion also increases as K^+ replaces Na^+. This feature can also be seen in the Raman spectroscopy (fig 3.22). The D1 and D2 peaks which correspond to four-fold rings and three-fold rings respectively. In the simulations, increasing of the D2 peak is not as large as it is in the experiments where this is attributed to Si-Al-Si three fold rings. This difference maybe be due to matrix elements effect in Raman spectroscopy. The final broad peak shows the increasing of T-O bond stretching increased with the K concentration in agreement with the experiments.

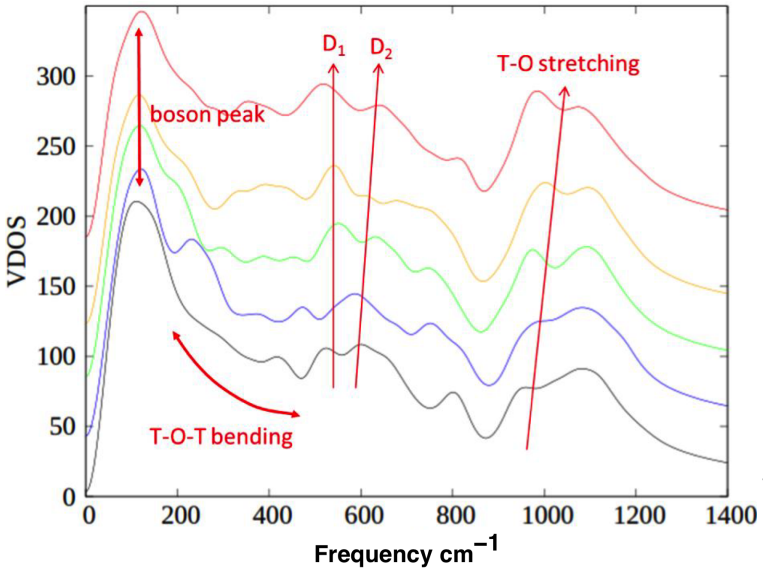

Fig. 3.23 Vibrational density of states (VDOS) simulated for 5 alkali concentrations. Similar to Raman spectroscopy (figure 3.22), four feature were observed. The peaks at 100 cm^{-1} are ascribed to boson peak. The peaks at around 500-600 are associated with four-fold ring and three fold rings. The peaks at 1000 correspond to Al/Si-O stretching.

CHAPTER 4

AMORPHIZATION OF ZIF8 UNDER PRESSURE

4.1 Introduction

Zeolitic Imidazolate Frameworks (ZIFs) are three dimensional low density structures consisting of Metal-N_4 tetrahedra linked through bridging imidazolate units. Similar topologies to crystalline ZIFs can be observed in zeolites (1.1.2) as mentioned before in first chapter. Due to the nano-porous properties of ZIFs, a large amount of research has been focusing on the gas adsorption ability of their pores considering the thermal effect on structure. A study on ZIF8 containing solvent has been reported [53] indicating that a transition phase appeared to exist by increasing pressure to 1.47 GPa squeezing solvent into other areas of the nano-porous structures. For solvent-free ZIF8, application of pressure up to around 0.3 GPa appears to be reversible described by 3rd-order Birch-Murnaghan Equation of State with a compressibility of 0.15(33) GPa^{-1}. At higher pressures, amorphization takes place both under hydrostatic and non-hydrostatic conditions. At 1.2 GPa, this appears to be permanent. However, in earlier atomic simulations on inorganic zeolites, collapse of Zeolite A was shown to comprise of two phase transitions which could be reversed by decompression in ambient pressure. Reversibility involved some hysteresis [54].

In this chapter, the Radial distribution function (RDF), Vibrational density of states (VDOS) and network topology of ZIF8 are followed as a function of pressure and time. In order to detect if phase transitions occurred in ZIF8 as they do in zeolite A, the changing volume of the simulation cell is recorded with increasing pressure. In addition, the reversibility of the transition is followed by de-pressurizing compressed structures. Molecular dynamics snapshots of different stages with structural simplification in compression and decompression are used to identify pressure-induced amorphization phase transitions and their decompression to the crystalline starting point.

In previous chapter 3, classical molecular dynamics methods were used to measure the structure and dynamics of nepheline at different temperatures. In the case of pressure induced amorphization, this empirical potential approach proved to be inadequate for following reasons. It's because empirical potentials generally have been developed and applied to reproduced structure of the crystalline state and thermal flexibility often with rigid bonds, links and angles (2.1.6). They are therefore not always appropriate to replicate the structure and compressibility except for less complicated inorganic crystals such as quartz [55]. DFT methods despite having smaller cell sizes, by using electron density (2.2.3) approach instead of empirical potentials, offer a better chance to follow pressure induced amorphization processes of organic-inorganic hybrid structures like ZIF8. Similar methods were also used to explore the compression and decompression of zeolite A [54].

4.1.1 Pressure-induced amorphization of ZIF8 using classical empirical potential approach

To replicate the crystalline structure of ZIF8, a classical molecular dynamics approach was first used. The potential used is based on a previous study on the flexibility of ZIF8 [56]. To accommodate the limitation of empirical potentials for an inorganic-organic structure like ZIF8 and its molecular linkage, carbon and hydrogen are separately parametrized as different species based on their sites in the molecule. For instance, the parameters of potentials for different carbons have to be adjusted based on the atoms they connect to. Therefore by applying these adjustments, the interatomic interaction can be simplified to a mixture of nearest neighbour bonded potentials and long range non-bonded potentials. The bonded part includes bond stretching and bending, proper and improper torsional potentials. The nonbonded potential includes Lennard-Jones (LJ) and Coulombic potentials. These methods were used for an initial study of the amorphization of ZIF8 using classical molecular dynamics.

ZIF8 has an identical structure to the inorganic zeolite sodalite except for tetrahedral centres (nodes) being occupied by Zn cations. The bridging molecular linkage (linker) is 2-methylimidazolate (figure 4.1) for ZIF8. The classical approach uses bonded potentials for nearest neighbours like Zn-N and N-C within the imidazolate unit and non-bonded potentials for all more distant interatomic pairs. Images of the crystalline ZIF8 and amorphized ZIF8 are shown in figure (4.2) [57]. In particular this initial study reproduced the amorphization of ZIF8 at 1.2 GPa found experimentally [58].

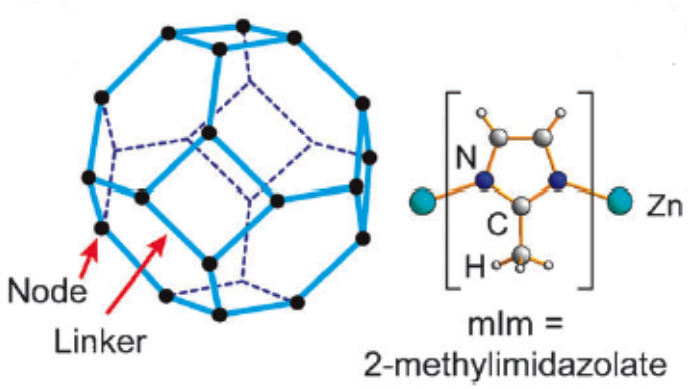

Fig. 4.1 the ZIFs structure (left) and the linker for ZIF8 (right) adapted from[15]. In the case of ZIF8, nodes are occupied by Zn atoms. A fully connected ZIF8 cage contains 8 six-node rings and 6 four-node rings.

This was an important contribution to the study of ZIF4 and ZIF8 amorphization [57]. Example of six-fold rings are shown for both structures where for ZIF-8 the six-fold ring is convex. It is noticeable that for the amorphized structure at 1.2 GPa there are concave configurations around the six-fold rings which are identified later in the ab initio calculations when similar pressures were used.

However, for higher pressures than the 1.2 GPa structure, the simulation cell failed to keep consistency possibly due to abnormal energy that was generated by extremely close atom pairs because of the empirical potentials. Although this approach successfully shows the onset of the amorphized structure, it has proved to be impractical for detailed quantitative simulations at higher pressures above 1.2 GPa.

4.2 Pressure effect and evidence for phase transitions using DFT methods

Because of the problems brought about by using classical empirical methods, an ab initio approach was used instead for simulating the structure of ZIF8 at different pressures including 1.2 GPa and above. By using the DFT methods as implemented in the code CP2K with PBE, one of the Generalized Gradient approximations (2.2.3), a more detailed and realistic ZIF-8 model was achieved at ambient conditions. GTH (Goedecker-Teter-Hutter) was selected for the pseudo-potential [59][60]. Further simu-

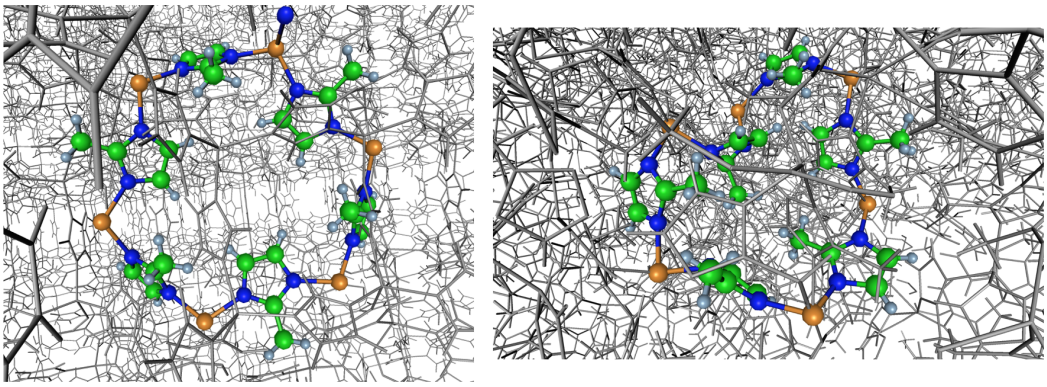

Fig. 4.2 A remnant six-fold ring structure. Zn(orange), N(blue), C(Green), H(grey) Left: ZIF-8 crystal Right: Pressure-induced amorphized ZIF-8 simulated by the author in the MD study contributing to [57]

Table 4.1 Simulated cell parameters of crystalline ZIF8 at ambient pressure. A cubic simulation cell is chosen.

Parameters	a (Å)	b (Å)	c (Å)	α(deg)	β(deg)	γ(deg)
Value	16.740	16.740	16.740	90	90	90

lations on compressing showed that it is also applicable for higher pressure simulations which go up to 5 GPa without unphysical interactions resulting in unrealistic cell structures.

To construct the ZIF-8 crystal, a geometry optimization was performed on the experimentally known ambient pressure ZIF-8 cell. The cell contains 276 atoms ($Zn_{12}N_{48}C_{96}H_{120}$). An ambient pressure test shows that the volume of the cell is 4691.24 Å^3 which corresponds to a density of 0.967 g/cm^3. Cell parameters at ambient condition are given below in table 4.1. The cell volume (4691.24 Å^3) is a little less (3 %) than the recorded crystallographic cell volume that is 4905.20 Å^3 which is the starting point for all calculations.

To neglect the possible extra thermal energy brought about by the thermostat and focus only on the effect of pressure on the system, all of the simulations have been performed on ambient temperature 300K. NPT Simulations, controlled by a Nose-Hoover thermostat and barostat, have been performed in ps scale to reveal the undergoing phase transition. All of the simulations are started from the geometry optimized structure but with different applied pressure. Figures 4.3 below shows the global structures obtained at various times following the application of pressure. These include six-fold rings

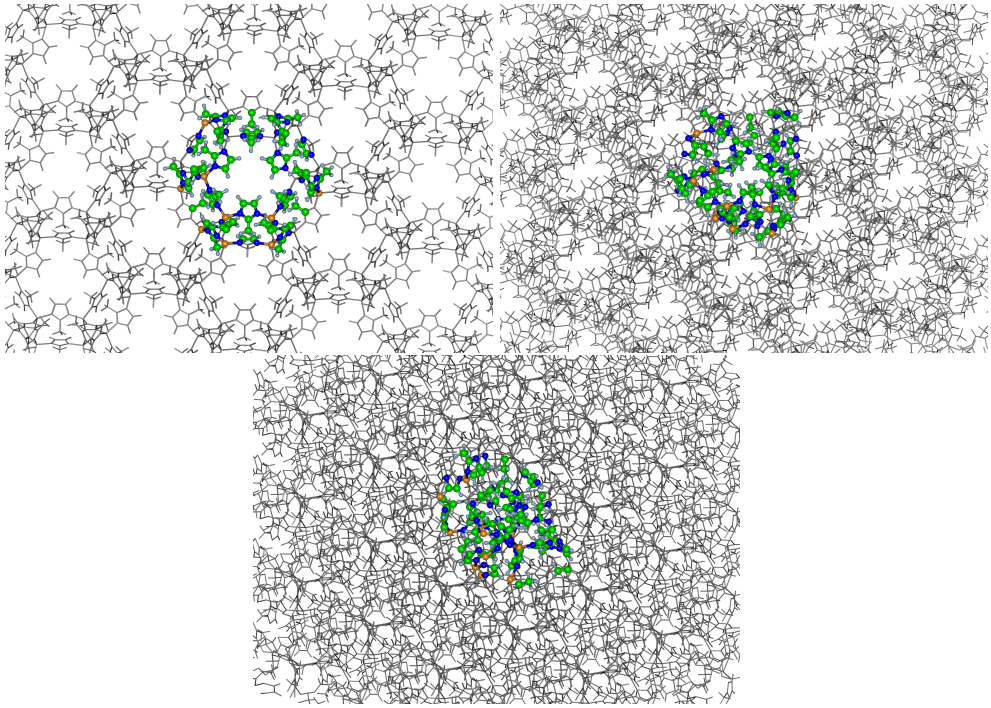

Fig. 4.3 Supercells built by periodically repeated unit cell of ZIF8 crystal, Low density amorphization (LDA) and High density amorphization (HDA), with simulation cell highlighted, obtained from 3.0 GPa compression at starting point, 1.2 ps and 6 ps.

highlighted at each stage. In order to reveal the physics of compression and later of decompression the changes of volume are first discussed and then the local structures of the tetrahedral Zn nodes (4.11).

4.2.1 Structure simplification and rings

In order to reveal the deformation and breaking of the amorphized ZIF8 structure, a simplification has been made to the snapshots shown above for clarification (4.3). Assuming only atoms of Zinc exist in the system and each one of them are connected to the nearest Zinc atoms, it is possible recognize some ring structure.

The distance for judging if two Zn are connected was set to be 6.3Å representing the first neighbour distance measured at ambient pressure. After applying a certain pressure on the ZIF8 structure, the stretching and tilting of these rings can be observed. With even higher pressure, the Zn rings lose their shapes and eventually breaks (figure 4.4). Their observation offers a chance to follow the topology changing during compressing without being obscured by surrounding atoms.

To explain the phase transition during pressure compression, the plot from 3.0 GPa is going to be discussed as follows in three phases (figure 4.4):

I_a. The optimized ordered structure locates at 4691 $Å^3$. The fully linked symmetrical rings indicate the complete structure without deformation from the effect of pressure.

I_b. Pressure changes the shapes of rings by affecting the bonding angle. Tilted rings are formed with less and less symmetry during gradual compression but retaining the ZIF8 ring topology.

II. An intermediate phase between the ordered and disordered topology is located around 3100 $Å^3$ (close to 2/3 of the starting volume) where again the crystalline topology is retained but the density is significantly higher and the rings are disordered with concave configurations reminiscent of the re-entrant topology of negative Poisson's ratio materials. This continues between 1 and 2 ps.

III. At longer time extending to 4 ps, the breaking of bonds within rings results in an amorphous topology and a higher density (almost double the density of the starting point).

In an earlier study of the compression of zeolite-A ([54]), similar stages were recorded using DFT methods. Starting from 0 GPa, the pressure of the system was increased incrementally with an interval of 0.25GPa for 100fs continuing to 10GPa. Generally, ZIFs are much more softer than zeolites as reported. This can be seen in figure (4.5)[15] where the elastic moduli of hard and soft materials are contrasted with their mechanical hardness. For elastic moduli, ZIF8 and other ZIFs are approximately a decade less than inorganic zeolites. Correspondingly their hardness is also around a decade softer than inorganic zeolites. Hybrid MOFs like ZIFs are best considered as soft materials. Organic molecular solids are generally referred to as soft and they overlap with the ZIF region. The dynamics of soft solids is expected to be significantly slower than the dynamics of inorganic materials like zeolites. Ceramics like alumina being mechanically the most resilient will respond to barostatic changes the most rapidly.

Accordingly, with ZIFs being softer than the inorganic zeolites amorphization pressures are expected to be smaller. Also, the equilibration time for zeolites to respond to changes in pressure should be much more smaller than for ZIF8 - 100fs [54] compared to 2ps (4.4). The larger equilibration time for ZIF8 provides the chance for looking

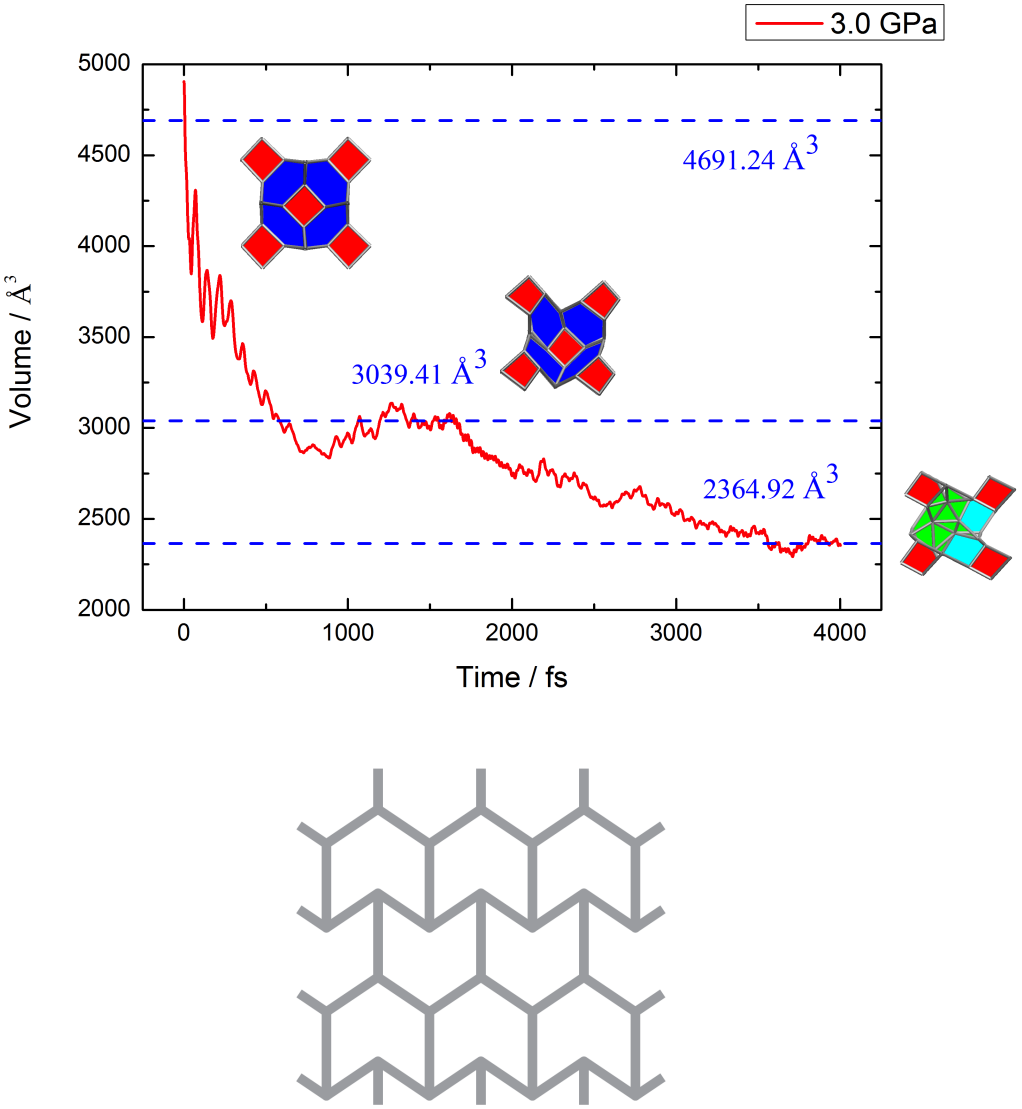

Fig. 4.4 (a)The cell volume of ZIF8 as a function of time during 3.0 GPa compression. Note six-fold Zinc rings become puckered with concave sections. (b) re-entrant hexagonal structure exhibiting negative poisson ratio [61]

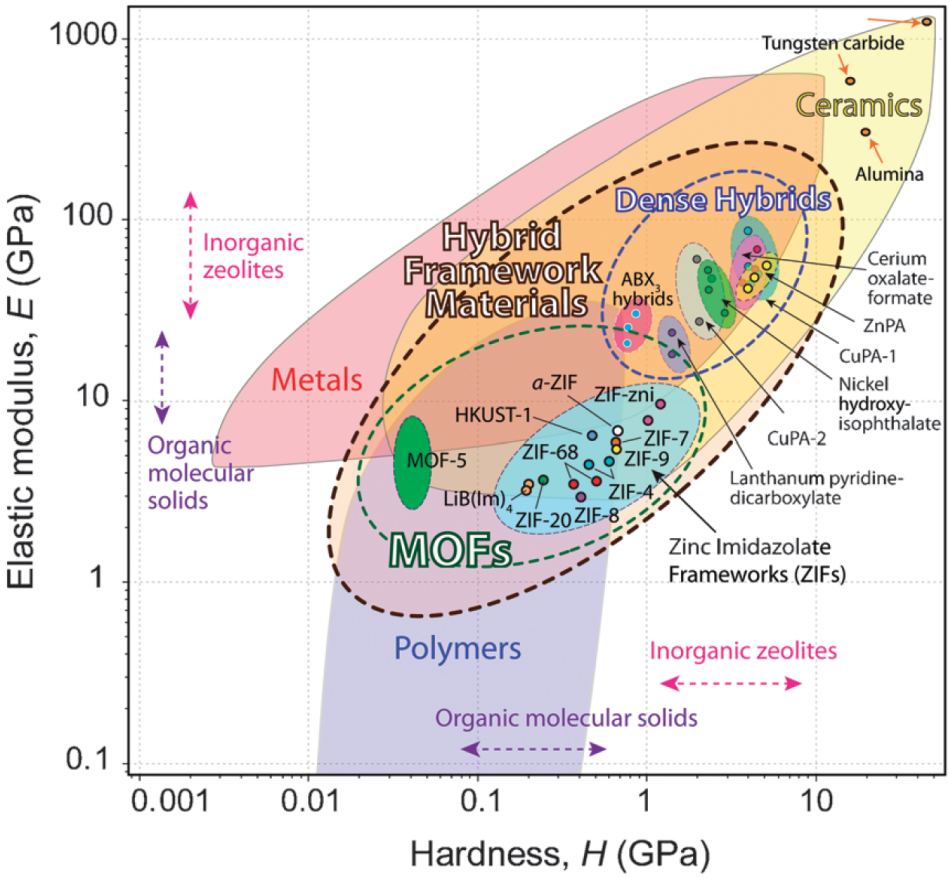

Fig. 4.5 Elastic moduli contrasted with mechanical hardness for MOFs, polymers, metals, inorganic zeolites and ceramics adapted from [15]. ZIFs can be seen in the centre of this Ashby map with inorganic zeolites located at above right of center. Organic molecular solids which are traditionally referred to as soft approximately overlap the ZIF region.

into volume changing versus time which would have been missed out if shorter run time have been used such as for zeolite A [54].

4.2.2 Volume changing versus time during compression of different pressures

Figures 4.7 below show the result of significant volume changes occurring as the starting pressure increases. In general, the volume decreases monotonically over the time resulting in different equilibrated volumes depending on the initial pressure applied (shown by the horizontal dashed line). However in the 3 GPa simulation and for similar pressures, a semi-equilibrated volume around 3039.41 $Å^3$ appears during 1100-1600 fs which can be clearly seen in figure (4.4) where it is evident that the significant changes occurring in volume for an initial pressure of 3 GPa would have been missed if the criteria used for inorganic zeolites had been followed [54]. Finally for 4 GPa the final volume stablises around 2267 $Å^3$ without clearly showing the intermediate phase (4.7). This is because the higher pressure accelerates the dynamics through the order-order transition leaving the order-disorder transition prominent.

Figure 4.8 shows the final volume at 4ps for each initial pressure ranging from 1 atm to 4 GPa. The volume decreases as the pressure increases while two major drops were observed at around 1.2 GPa and 2.4 GPa. The first of these coincides with the experimental observations using X-ray diffraction by Chapman et al. [58] who followed the ZIF8 Debye-Scherrer pattern until it disappeared. In the present simulations, the equilibrated volume can be followed to higher pressures when the structures are aperiodic. In this way we can identify the second transformation at 2.4 GPa. Returning to the sodalite cage graphics illustrated in figure (4.4), a pressure of 1.2 GPa coincides with the transformation which retains the topology of ZIF8 despite minor distortions in the linker ring structures. On this basis, given the well defined equilibrated volume, this is associated with an order-order transition. Similarly at 2.4 GPa, which is out of the range of X-ray diffraction techniques, the abrupt decline in volume is associated with an order-disorder transition, given the breaking up of the sodalite cage evident in the graphics figure (4.4) and the inter diffusion of Zn ions . Both the intermediate ordered phase and the final disordered phase are amorphous following the description of the collapse of inorganic zeolites ([61] , [16]). These are corresponding to the low density amorphous (LDA) and high density amorphous (HDA) phases respectively described in the literature of polymorphism [62].

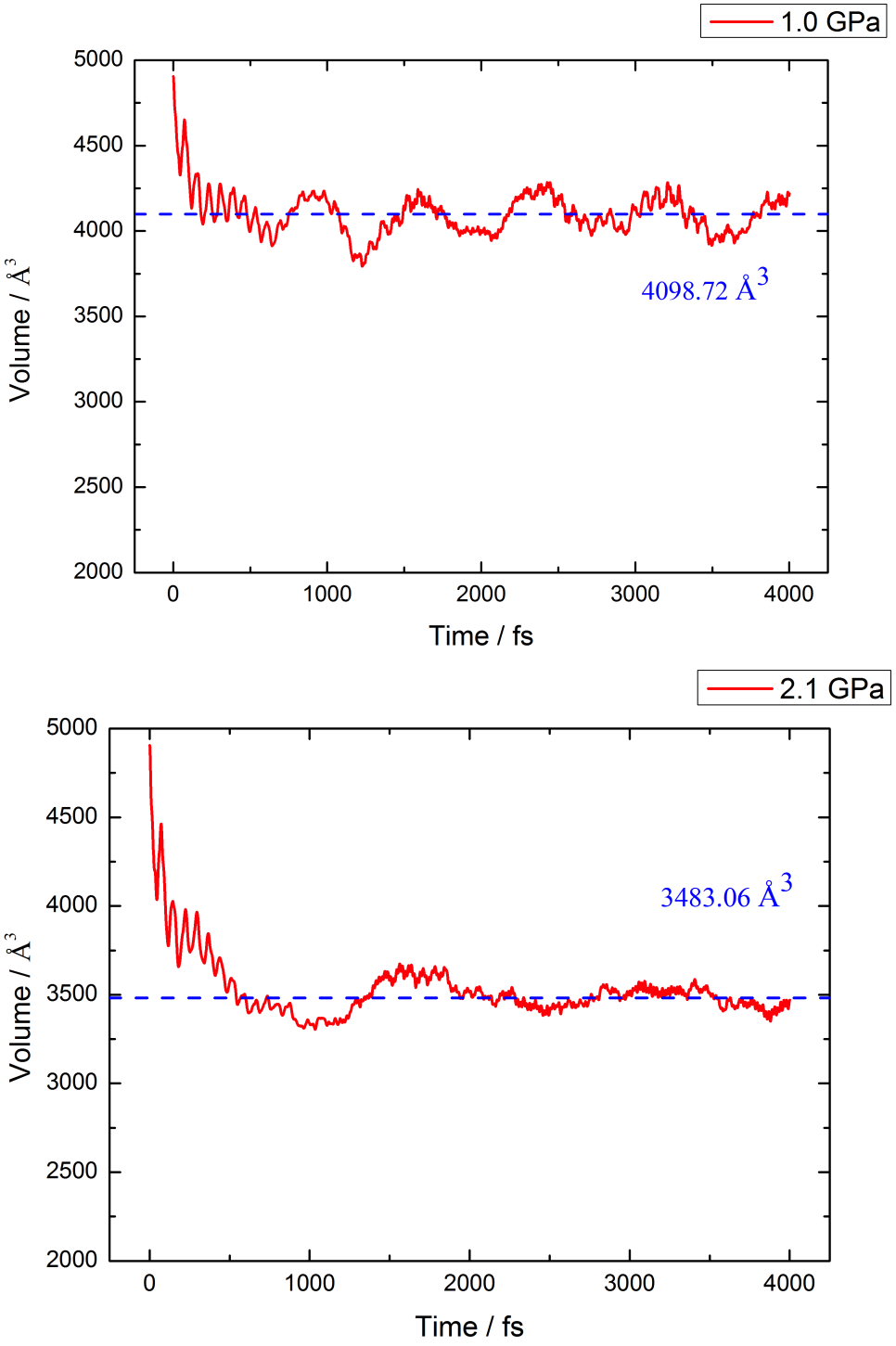

Fig. 4.6 Plots of volume changing versus time during compression of ZIF8 at 1 GPa and 2.1 GPa. The final equilibrated volume after 4ps of compression (shown in blue) decreases as the applied pressure increases (shown as legend). Plots at 3.0GPa and 4.0GPa are on the next page.

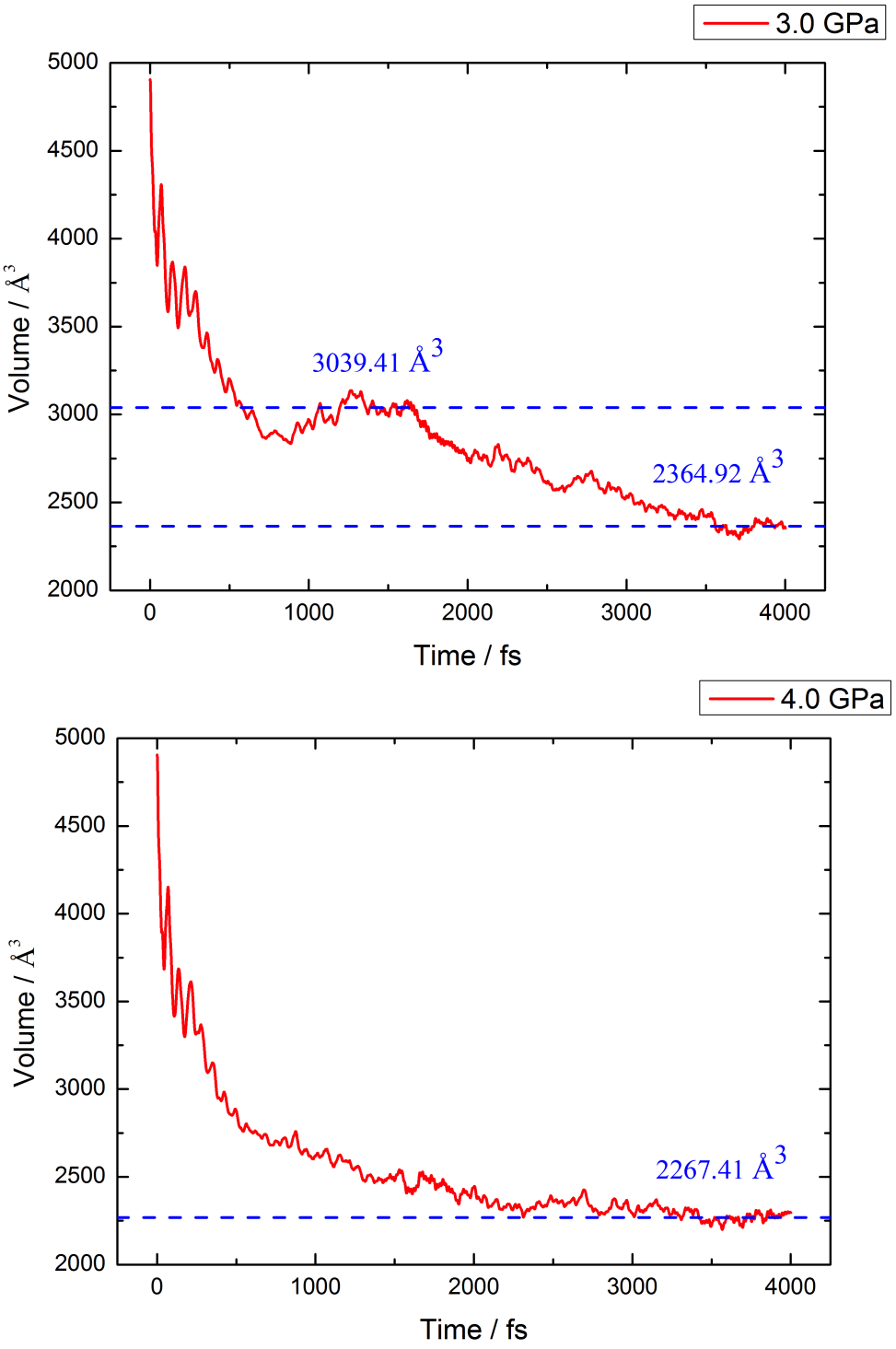

Fig. 4.7 In the plot of 3.0 GPa, a noticeable intermediate volume can be observed at around 3000 Å^3 of volume. This corresponds to the intermediate phase mentioned in figure 4.4 where the ring topology of ZIF8 crystal still remains. At even higher pressure 4GPa, the intermediate volume becomes less noticeable due to the faster dynamics.

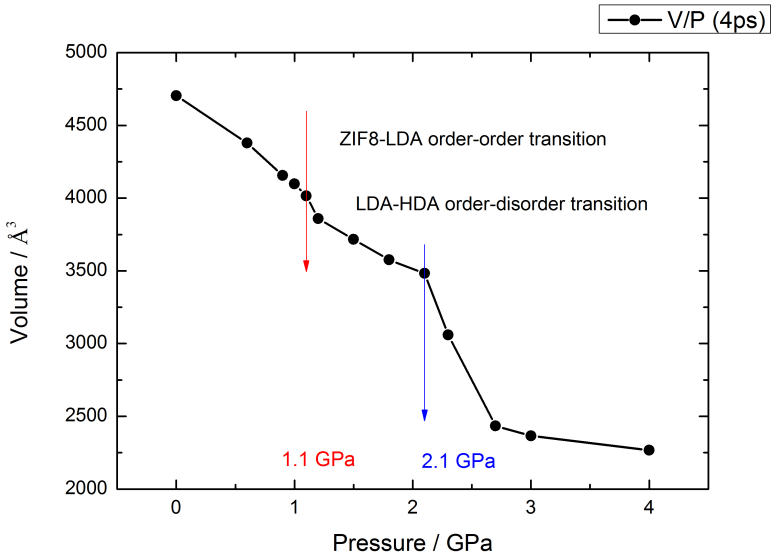

Fig. 4.8 Equilibrated volume at 4ps (from figure 4.7) versus applied pressure. Discontinuities appear at 1.2 GPa and 2.4 GPa identified by the arrows are interpreted as order-order and order-disorder transitions respectively. With the intermediate phase identified with a low density amorphous (LDA) phase and the final phase with a high density amorphous (HDA) phase as described in the text.

From the volume versus pressure results showing in figure (4.8) the compressibility $\beta = \frac{-\delta V}{V \delta P}$ can be obtained shown in figure (4.9). The base line compressibility which starts at 0.3 GPa falls with increasing pressure as expected. The initial value at 0.3 GP (0.1197 GPa^{-1}) is in reasonable agreement with the experimental value (0.1533 GPa^{-1}) obtained from the 3rd-order Birch-Murnaghan Equation of State from X-ray diffraction [58]. The abrupt changes in volume versus pressure at 1.2 GPa and 2.4 GPa in figure 4.8 translate into sharp peaks in compressibility (figure 4.9), indicating the compressing structure becomes sharply compressible as each of the phase transition is approached then falls back to the base line when complete. This mechanical softening can be attributed to the coexistence phases, viz, ZIF8 and LDA, LDA and HDA respectively.

4.3 Radial distribution function

To confirm that the ab initio model provides realistic structures, RDFs of crystalline ZIF-8 were calculated up to 10 Å in distance. Peaks that appear below 2 Å represent

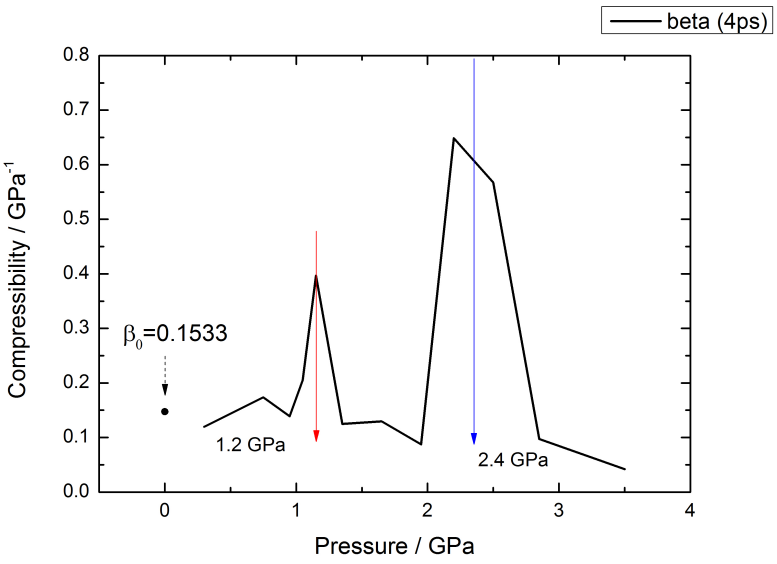

Fig. 4.9 Compressibility plot versus applied pressure derived from the volume versus pressure (figure 4.8). Except the two spiking peaks, the compressibility generally decreases as the pressure increases. The compressibility at 0.3 GPa reasonably matches the arrow which is associated with the experimentally measured value using 3rd Birch-Murnaghan equation of state[58]. Two marked sharp peaks (red at 1.2 GPa and blue at 2.4 GPa) are corresponding to the abrupt rising of compressibility at the order-order phase transition and order-disorder phase transition respectively.

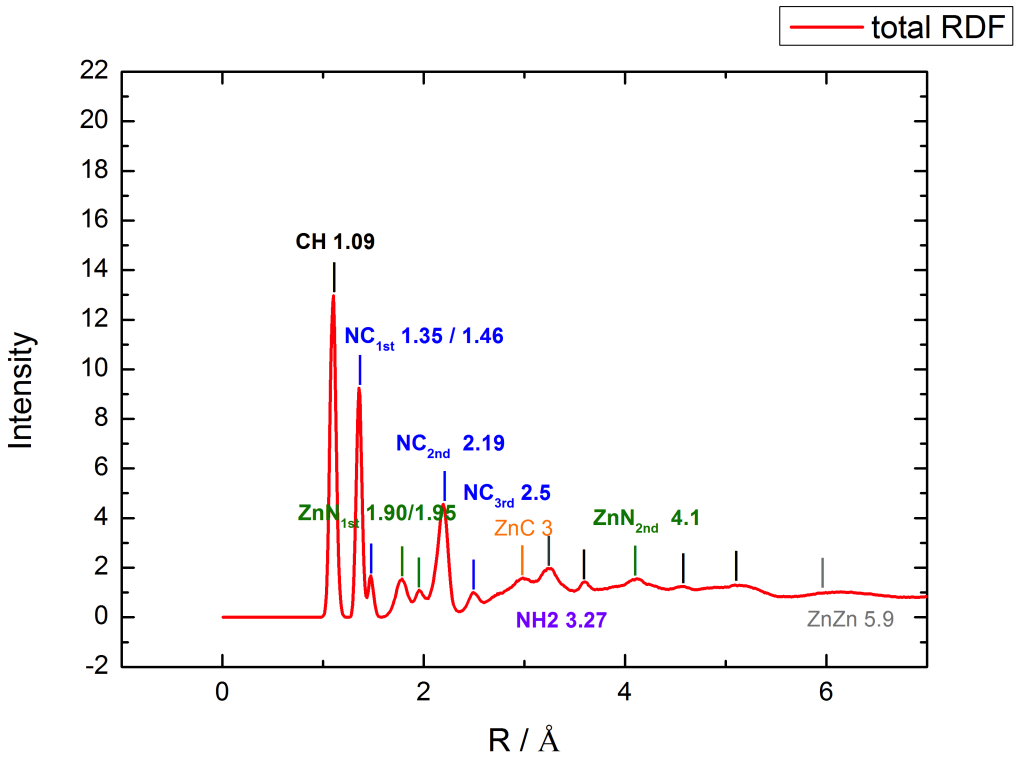

Fig. 4.10 The total radial distribution function of crystalline ZIF8. Peaks marked by vertical bars represent the possible neighbour pairs of two atom species. Each first peak at short distance indicates the bonding distance of certain atom pairs. Peaks at distances above 4 are inappropriate to be interpreted due to the overlap of many atom pairs.

the first neighbour distance of certain atom pairs. These distances can be compared with the experimental measurements.

In ZIF8, the nodes are occupied by the Zn atoms. By assuming only Zn existing in the system with a reasonable bonding cutoff, the crystalline ZIF8 can be seen as sodalite cages consisting of six-fold rings (yellow) and four fold rings (red) shown in figure (4.11 b). The peaks appearing in pair distribution function of Zn-Zn (4.11 left top) indicate the corresponding Zn-Zn distance within the rings. In figure (4.11 right top), the position of four peaks are related to 1st, 2nd, 3rd, 4th neighbouring distance of Zn-Zn respectively.

In the compressed structure of LDA, all peaks shift left as the atoms become closer, as expected (figure 4.11 left middle). Also, the deformation of rings flatten the peaks indicating the gradual loss of symmetry of rings. Furthermore, in figure (4.11) four-fold rings originally within the surface of the sodalite cage pop in and out of the

adjacent cages retaining the same amount of four fold ring and six fold rings making the transition topologically invariant. The arrangement of six fold rings acquires concave features reminiscent of semi-re-entrant geometry of auxetic (negative poisson ratio) structures[61]. In addition, the porosity of ZIF8 appears to transfer to LDA.

The further increasing of pressure results in a HDA phase (figure 4.11 right bottom). Peaks corresponding to four-fold rings and six-fold rings merge respectively and would eventually become one broad peak. This reflects the disappearing of ring shape which affects the Zn-Zn distances to be homogeneous. In this disordered high density structure, porosity would appear to be pinched off compared to LDA and ZIF8 topologies. In the crystal phase of ZIF8, each four-fold ring is adjacent by 4 six-fold rings. Comparably, due to the deformation with compression, large-member rings like 6 fold rings are decomposed into four fold rings and five fold rings. with the further compression, this decomposing should continue. Considering the pressure dependence of silica glass, the change in network topology might occur as amorphous-amorphous phase transition which falls around 10 GPa recovering on decompression [61].

Previous work on zeolite A reveals that the phase transition is reversible in such pressure-induced amorphization [54]. To discover the potential of reversibility for ZIF8, two compressed structures at 2.7 GPa and 2.3 GPa, corresponding to HDA and LDA respectively, were decompressed to a pressure of 1 atm. The recovering of associated four and six fold rings (shown in figure 4.12) proves that a similar reversed phase transition is achievable in ZIF8 as well as in zeolite A. These can also be confirmed by the radial distribution function provided above and VDOS plots which are going to be shown later. From figure (4.12), it is clear that decompression to an LDA with virtually the same topology at compression together with the topologies of the starting and ending ZIF8 mean that the porosity of the two LDA structures appear to be very similar. This suggests that the initial stage of amorphization to the intermediate LDA phase is not destructive in terms of porosity. Experimental evidence for the recovering can be found in the Fourier transform infrared spectroscopy (FTIR) [63] where decompression recovered from high pressure material results in a different spectrum compared to decompression from intermediate pressures taken together - simulation and experiment it may well be possible to isolate porous LDA for classical MOF compositions.

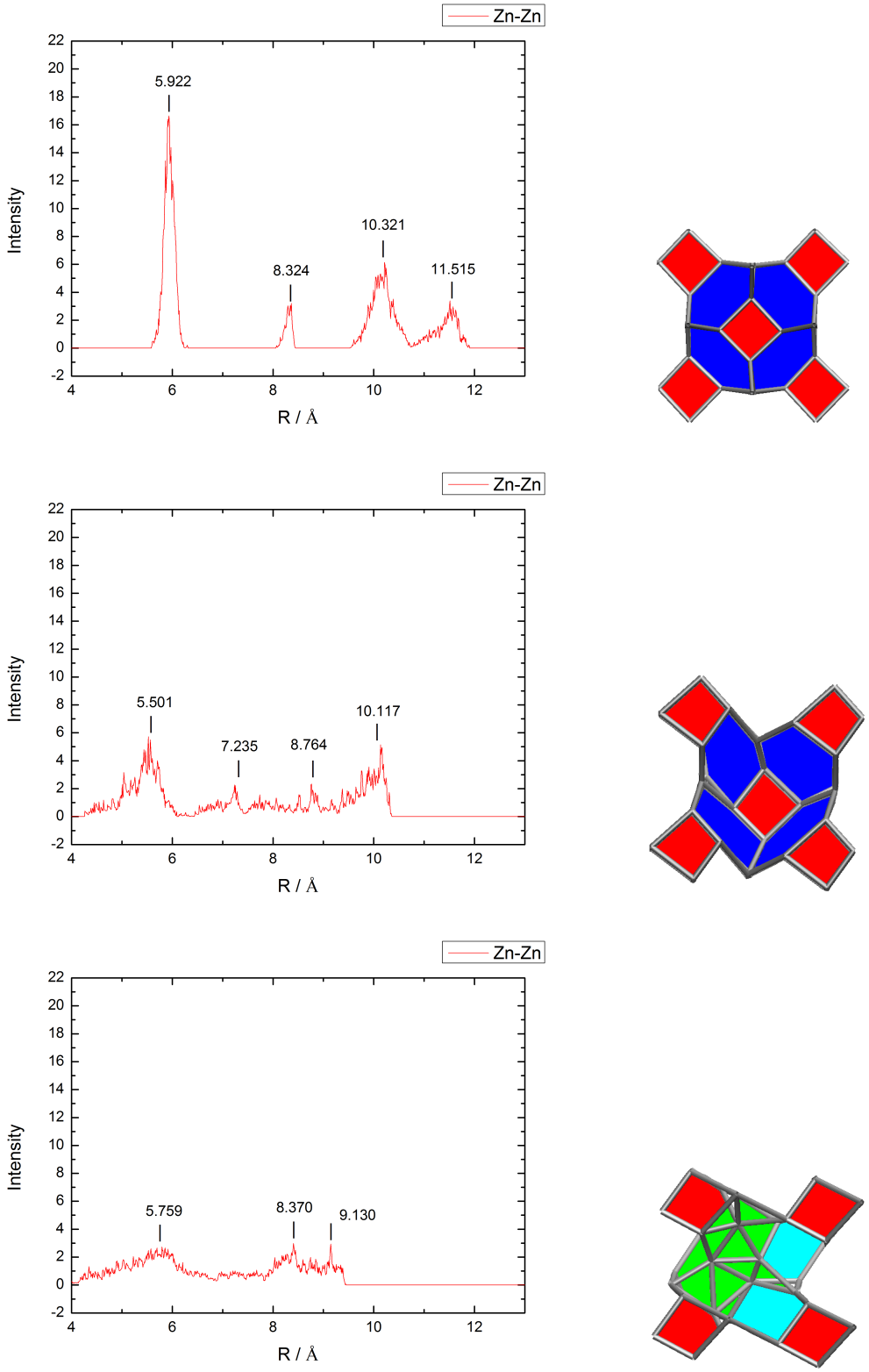

Fig. 4.11 Left column: Zn-Zn radial distribution function at three phases (crystal, LDA, HDA) Right column : MD shots at three phases with simplified Zn ring structures

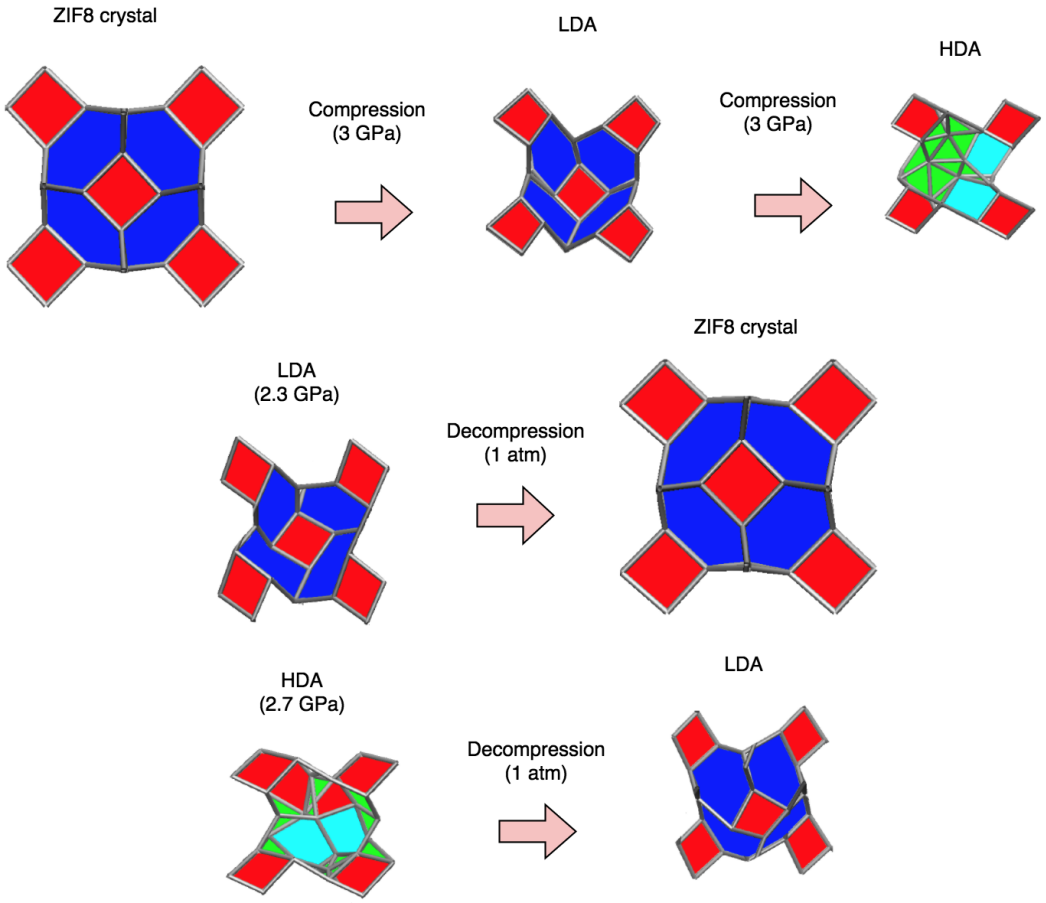

Fig. 4.12 Top: Compression of 3GPa following phase transition ZIF8-LDA and LDA-HDA Middle: HDA structure of 2.7GPa decompress at 1 atm to the LDA phase. Bottom: LDA structure of 2.3 GPa decompress at 1 atm to the ZIF8 phase. Topology changing through compression and decompression. The number of four and six fold rings persistent through compressing from ZIF8 to LDA then is eventually lost in HDA together with the inter-ring association. With decompression, this ring association is recovered first LDA then ZIF8. The recovered LDA and ZIF8 are not identical to the initial ones but sufficient for the four and six fold ring associations.

4.4 Vibrational density of states

4.4.1 Introduction

As shown in chapter of nepheline before, from the Vibrational density of states (VDOS) it is able to attribute the motion of rings to specific modes. The VDOS can be obtained from the velocity autocorrelation function (VAF) of different structures Fourier transformed into frequency spectra. The peaks of the VDOS represent the possible frequency modes of certain geometries in the structure. For instances, the peak of six-fold rings would appear at a lower frequency than the four-fold rings and eight-fold rings lower more. Other modes can be associated with bending, wagging vibrations and stretching vibrations which should occur at higher frequencies. Figure (4.13) shows the modes from collective vibrations at THz frequencies through to stretching frequencies in the near infrared. Very reasonable agreement is obtained between the simulated VDOS and Raman spectra for ZIF8 (figure 4.13). However, the intensity of Raman peaks will be affected by the matrix element effect in Raman processes.

4.4.2 Attributions of vibrational modes

Detailed attributions between 500 and 1600 cm^{-1} to motions ranging from imidazolate puckering, out of plane C-H bending, methyl bending with C-N stretching and wagging can be seen in literature [64]. Between 2750 and 3250 cm^{-1}, the double feature is attributed to methyl and aromatic C-H stretching Below 500 cm^{-1}, our new simulations reveal several peaks in the THz region which are attributed in this study to collective atomic motions involving many atoms and large rings as discussed below.

The VDOS of the ZIF8 crystal obtained from a 6 ps simulation is shown below in figure (4.13) with the experimentally measured Raman spectrum [64]. There are 13 features being marked out corresponding to different modes of dynamics of atom pairs including bending (both in plane and out plane), stretching and wagging. 10 of the features can be replicated in the simulated VDOS spectrum. With even longer simulation time which affects the resolution of VDOS, more individual peaks are able to be resolved.

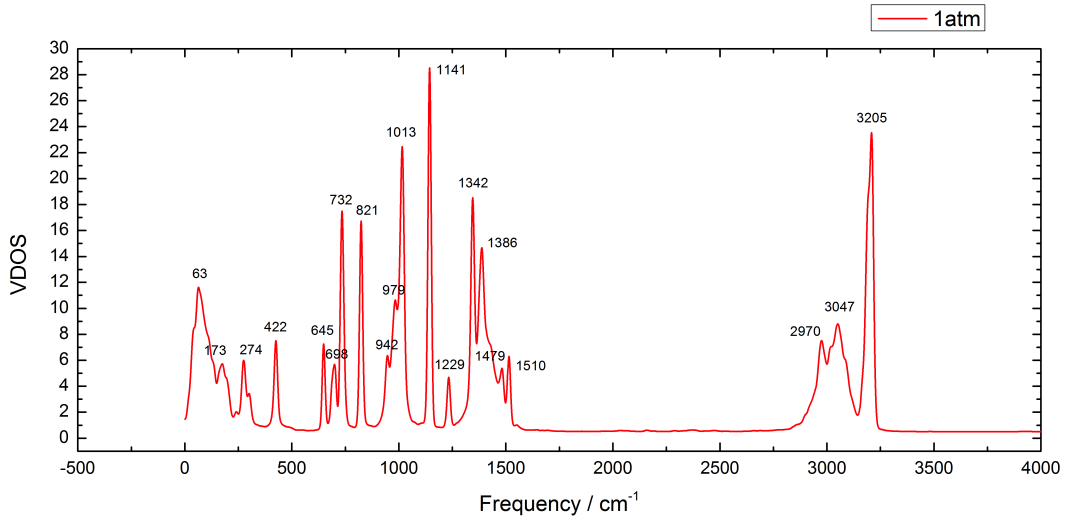

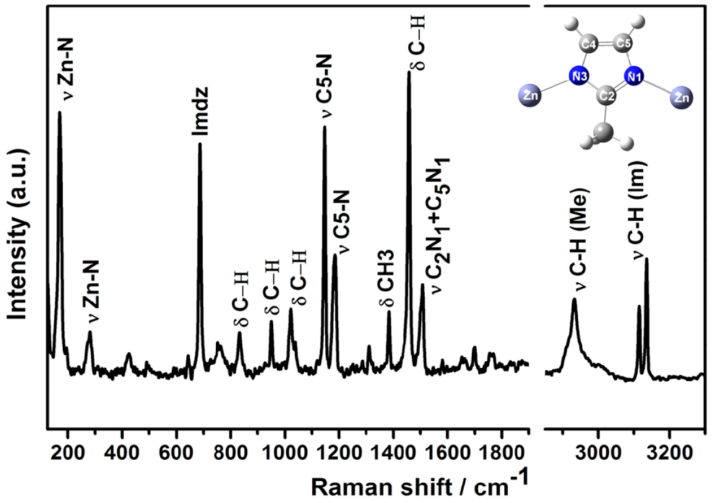

frequency (cm^{-1})	band assignment[a]
168	ν Zn–N
273	ν Zn–N
686	Imdz ring puckering, H oop bend
755	C═N oop bend, δ N–H
833	C–H oop bend (C4–C5)
950	C–H oop bend (C2–H)
1021	C–H oop bend
1146	ν C5–N
1180	ν C–N + N–H wag
1187	ν C–N
1311	ring expansion + N–H wag
1384	δ CH3
1458	C–H wag
1499	C2N3 + C4N3 + ν C5N1 + N-Hwag
1508	ν C4–C5
2915	ν_{sym} C–H (methyl)
2931	ν_{asym} C–H (methyl)
3110	ν C–H (ar)
3131	ν C–H (ar)

Fig. 4.13 Top: VDOS obtained by Fourier transforming the Velocity autocorrelation function obtained from a 6ps run. Middle: Raman spectrum obtained from [64]. Each of the peak in Raman spectrum is attributed to a certain mode of bonding, stretching or wagging. Bottom: Peak attribution table obtained from [64].

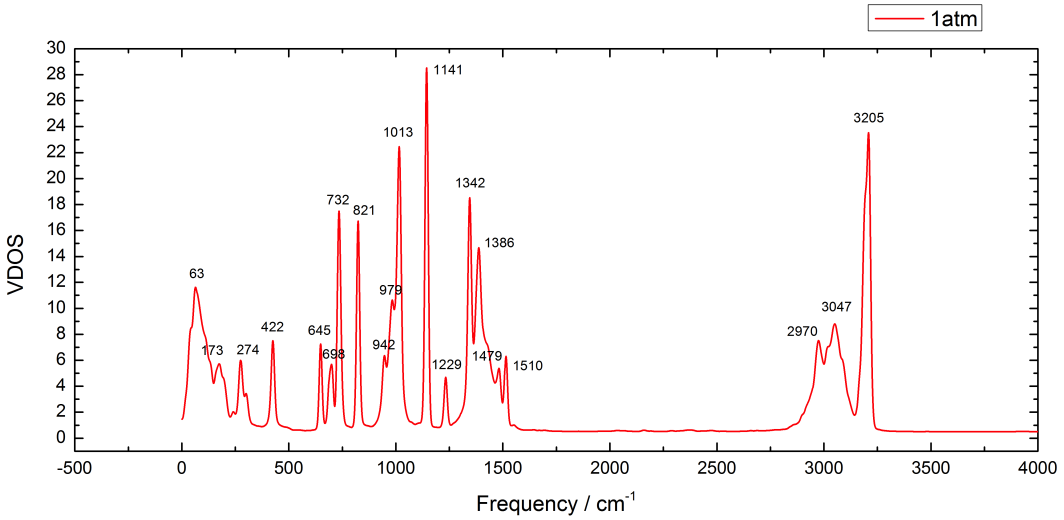

Fig. 4.14 VDOS of ZIF8 crystal. Numbers are marked on peaks associating with various motion modes within the system.

4.4.3 Changes in VDOS on compression and decompression

There are significant changes to the peaks with compressions first to LDA then to HDA. In particular, the peak corresponding to methyl bending at 1386 cm^{-1} increases significantly in LDA suggesting increased dynamics of methyl groups compared to ZIF8. All other modes decrease in intensity with broadening. The low frequency groups below 500 cm^{-1} have some significantly change due to the deforming and reordering of Zn rings with four, six or even higher members which appears responsible for the decreased intensities in the collective motion region. This is also the case for HDA. In addition the peak attributed to ring expansion at 1229 cm^{-1} disappears in HDA commensurate with the increasing density and diminishing of ring geometry, for example 6 fold rings (figure 4.12).

Decompression from HDA to LDA confirms the recovery of the inter-mediate phase including methyl bending with C-N stretching and wagging at 1385^{-1} likewise all other bands sharpen from HDA back to LDA (figure 4.15). This is because of the dominance of modes associated with the organic linkage common to all of these structures. This demonstrates that the VDOS and Raman spectroscopy is not very sensitive to topological changes (figure 5.18). The main changes occur in the low frequency bands attributed to collective vibrational modes associated with larger rings.

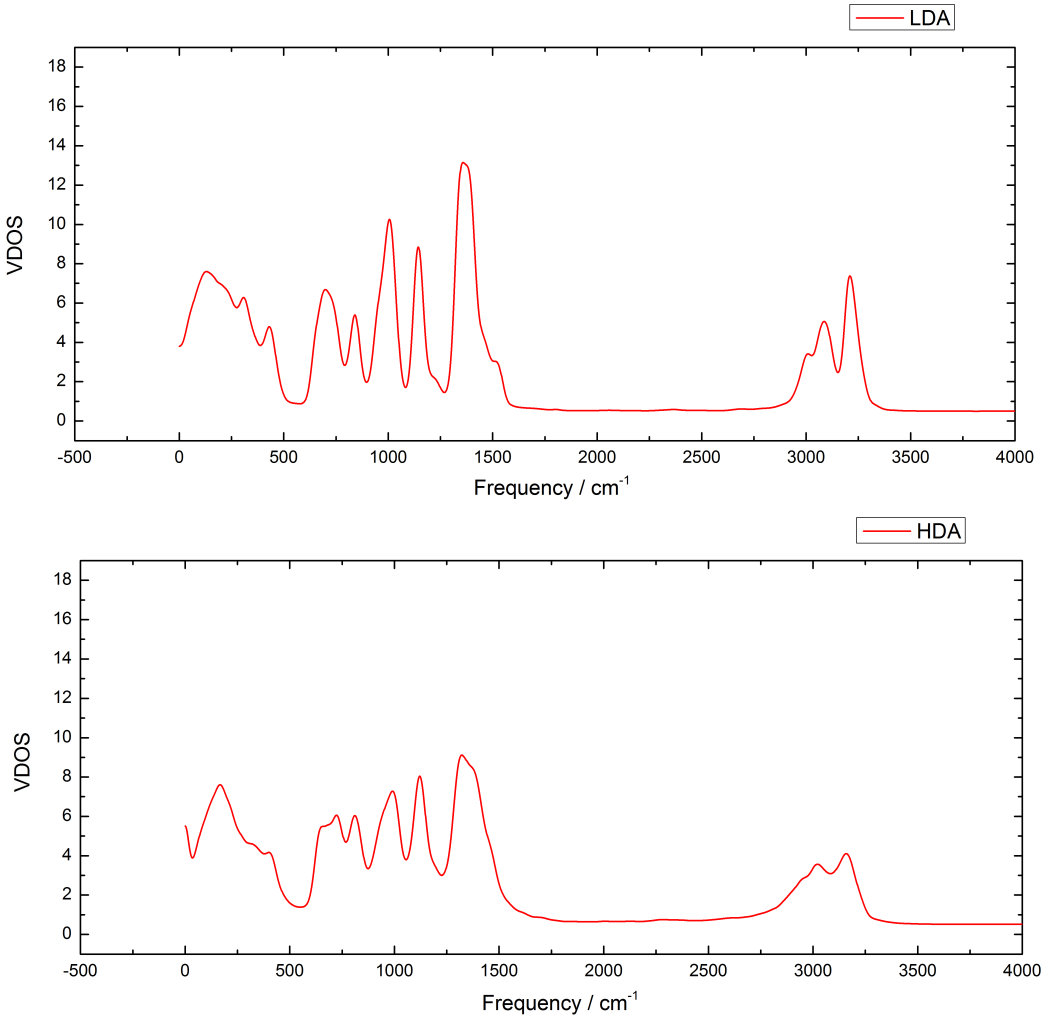

Fig. 4.15 VDOS of amorphized phase LDA and HDA. Generally, when systems become more and more amorphized, the peaks of VDOS decrease in intensity and become broader. Multiple peaks are merging into one in HDA.

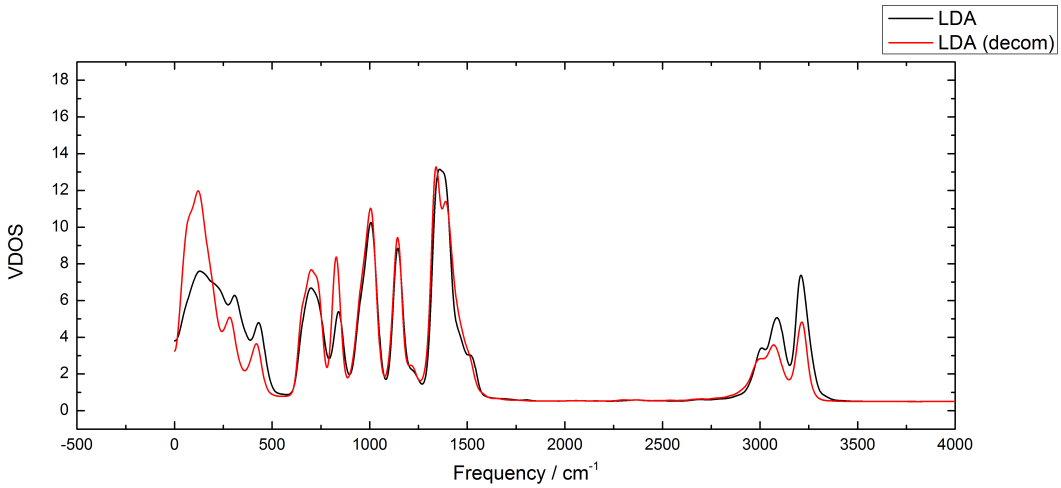

Fig. 4.16 Comparison between compressed LDA and decompressed LDA. As the structure being restored from HDA to LDA, the peaks corresponding to LDA structure rise back. Two shoulder peaks before 500 cm^{-1} (corresponding to Zn) indicate the reassembling of the Zn ring topology.

Decompression from LDA to ZIF8 is shown at figure 4.17 indicates that all original modes are recovered in line with the four and six fold ring topology of Zn. However, the intensities of methyl and aromatic stretching modes around 3100 cm^{-1} are weaker on decompression while the THz modes between 0 and 500 cm^{-1} are stronger. This suggests that the recovered sodalite structures is more flexible compared to the compressed one while the linkage stretching modes are still similar.

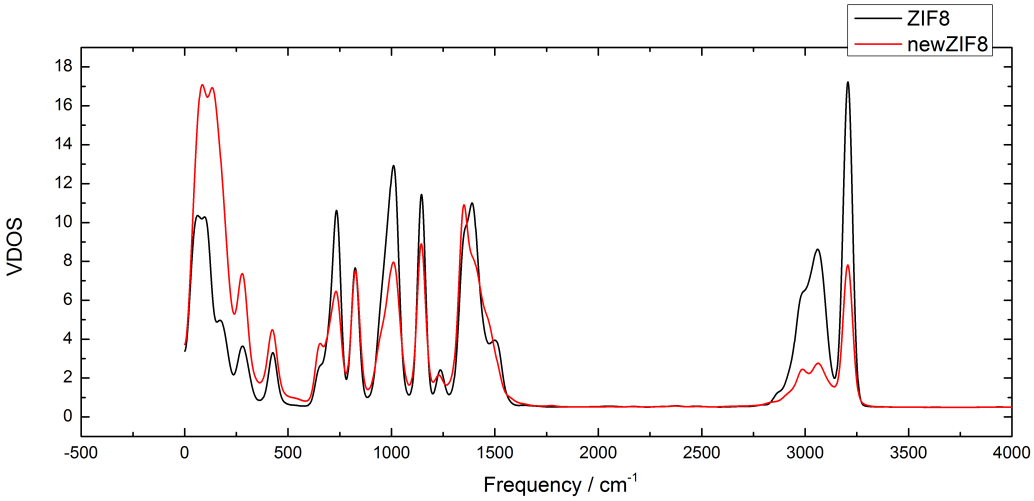

Fig. 4.17 Comparison between compressed original crystal and decompressed crystal. The medium frequency zone is almost fully restored.

CHAPTER 5

SODALITE

5.1 Introduction

As introduced in first chapter, zeolite has diverse framework types which are made of various building units (1.1.2). Usually they can be represented by three letters. In this chapter, SOD zeolites, named due to the topological similarity between sodalite and them, are going to be studied. SOD is going to be used as short notation for crystalline pure-silica sodalite later on in this chapter. Compared to the material nepheline in the Chapter 3, zeolites generally have lower density due to the higher porosity. The SOD only contains two types of atoms: Si and O, similar to silica, resulting a fairly rigid structure comparing to ZIF8. This can be reflected from the simulation of compression later. The topology of SOD can be constructed by connecting tetrahedra units of SiO_4, being shown in figure 5.1, forming four-fold rings and six fold rings. Based on ring structure, a sodalite cage can be recognised as an assemble of rings. This is similar to what being discussed before in the ZIF8 chapter where linkers and nodes of different elements (or group of element) form similar tetrahedra units. Due to the periodic boundary condition of unit cell, such sodalite cage is going to be manually selected for demonstration because sharing ring unit between adjacent periodic cells can cause confusion. For convenience, the central sodalite cage (figure 5.1 d) is going to be isolated for clarification. To interpret the structure of SOD, Si-Si distances are going to be examined in following sections since it controls the shape and size of ring. The value for 1st,2nd,3rd,4th neighbouring Si-Si distances is shown in figure 5.1. A close matching is going to be attempted in simulation with the calculation of radial distribution function.

Similar to ZIF8, DFT methods were used for modelling the SOD. A GGA (Generalized Gradient Approximation) methods implemented in CP2K codes with GTH pseudo-potential[59][60] have been used for DFT. Preparation of crystalline SOD requires a geometry optimization on the recorded SOD structure as well as an equilibration MD run in ambient condition. The volume changing during ambient condition simulation

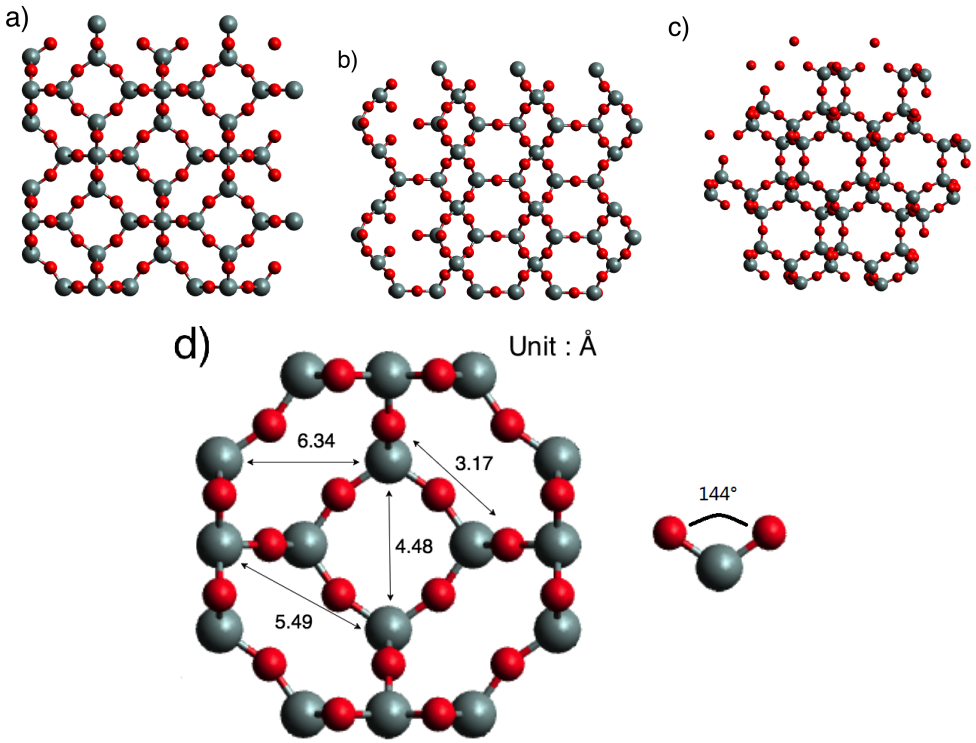

Fig. 5.1 a),b),c) (001) (011) and (111) surfaces of sodalite crystal. d) A zoom-in view of one sodalite cage showing Si-Si distances in unit of angstroms from 1st neighbour to 4th neighbour.

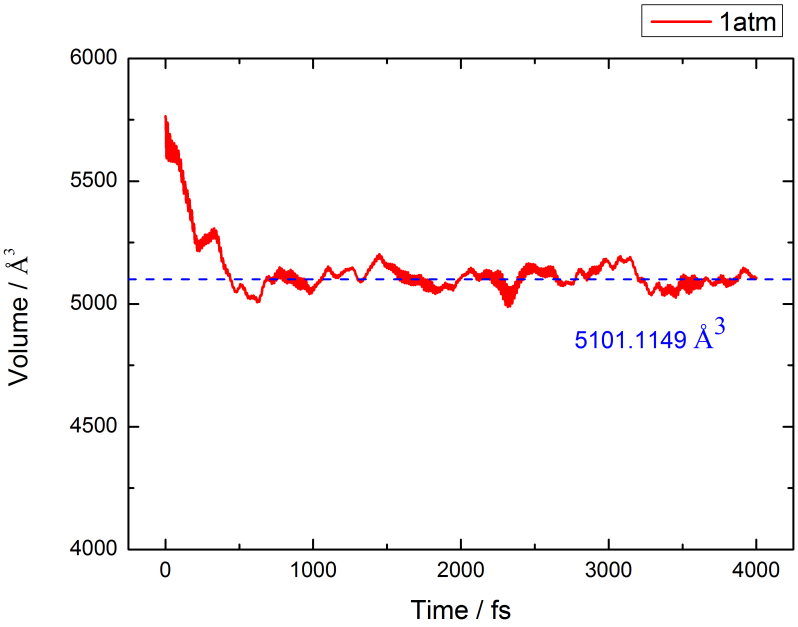

Fig. 5.2 Volume of SOD versus time at ambient pressure. The structure at first step is obtained from the geometry optimization. The final volume is averaged from last 1000 fs.

was recorded as shown in figure 5.2. The difference between the recorded volume and simulated volume (1 atm, 300K) is around 10 %. This is possibly due to a iso-symmetric change between I43m and Im3m space groups ([65]) which is going to be discussed later.

5.1.1 Pressure-induced amorphization of SOD zeolite

Many minerals can become amorphous by applying pressure. This phenomenon is known as pressure-induced amorphization (PIA). In the previous study of ZIF8, such process are proved to be reversible in between crystalline and LDA as well as LDA and HDA. In this chapter, SOD zeolites are going to be simulated under both compressing and decompressing condition to study the PIA. Volume versus time, compressibility, coordination number, radial distribution function and Vibrational density of states (VDOS) at each phase are going to be presented to support the contention that two phase transitions and their reversibility can also occur in sodalite.

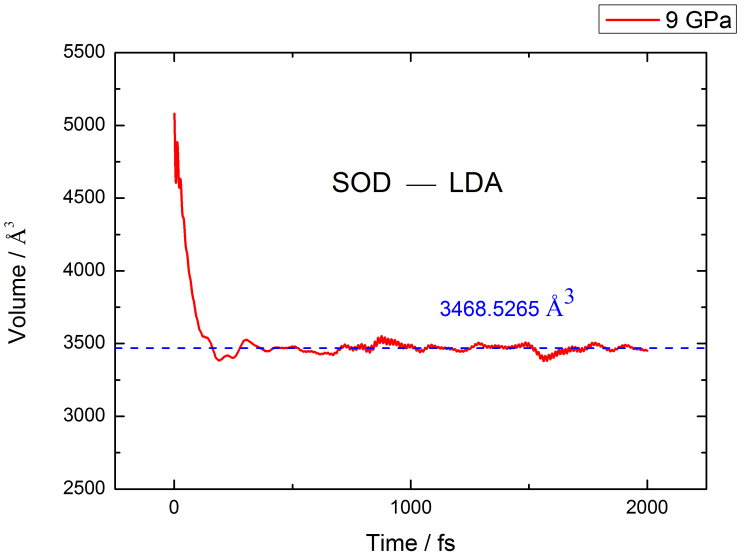

Fig. 5.3 Volume versus time of 9 GPa compression run within 2 ps. The volume decreases much more quicker compared to the ZIF8 in last chapter due to the much higher applied pressure. The final LDA volume is around 68 % of origin.

5.2 Volume versus time

During the compression, the volume continuously drops despite fluctuation comes from thermostat and barostat as shown at both 9 GPa and 13 GPa. During the compression at 9 GPa, the volume goes down and eventually flats at around 3500 Å (figure 5.3). On the other hand, during the compression at 13 GPa, the volume decreases rapidly to roughly 3100 Å at around 200 fs then stays for 100 fs. Beyond the 300 fs, the volume continues to drop down and reaches around 2750 Å at the 2 ps (figure 5.4). The two steps of volume changing 13 GPa indicates the potential existence of two possible phase transition during compression.

During the decompression, the initial pressure applied to obtained the LDA or HDA was reset to 1 atm. As shown in both HDA to LDA and LDA to SOD transition (figure 5.5 and5.6), the volume increases and eventually equilibrates at a very close number to the initial phase as shown in compression run(figure 5.3 and 5.4). These suggest that the amorphous structure is to be restored at least in the case of volume. The detail of structure and dynamics changing in reversed phase transition are going to discuss later in this chapter.

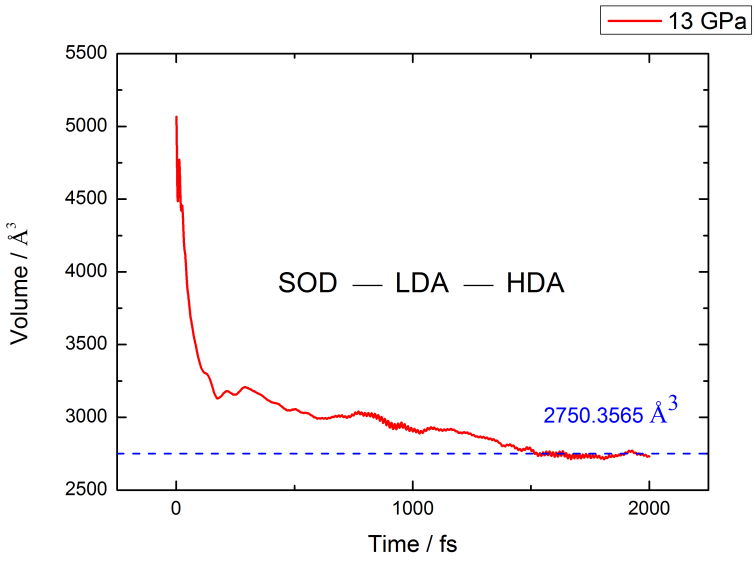

Fig. 5.4 With higher pressure 13 GPa, the volume continuously decreases passing through the LDA volume until the end around 2ps. The HDA volume is roughly 54 % of SOD phase.

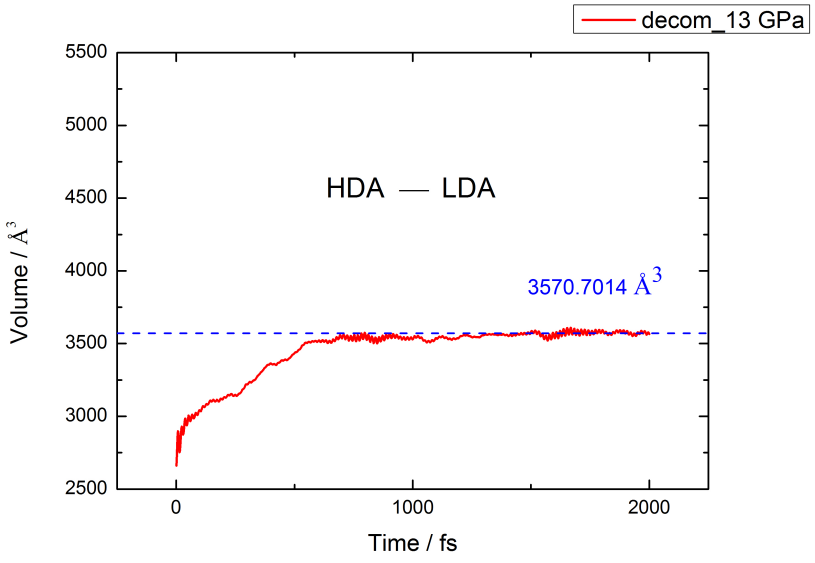

Fig. 5.5 Volume versus time during decompression at ambient pressure of HDA phase. The volume difference between restored LDA and compressed LDA is around 3 %

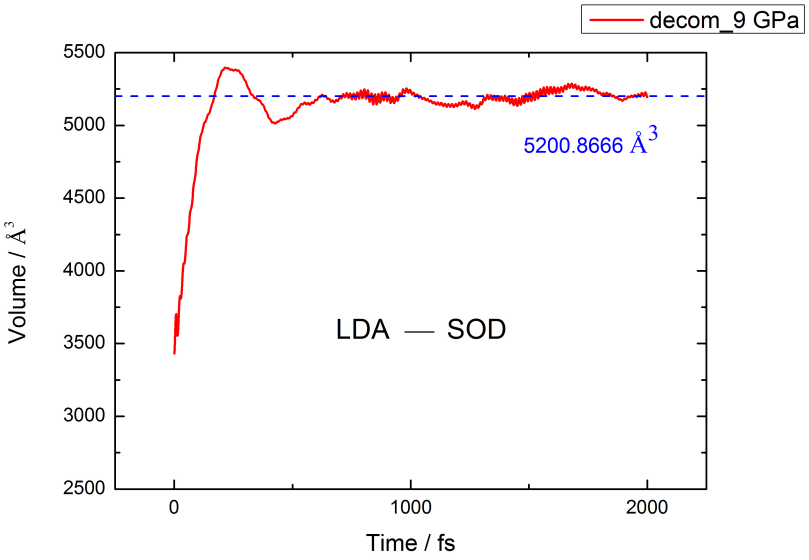

Fig. 5.6 Volume versus time during decompression at ambient pressure of LDA phase. The volume difference between restored SOD and original SOD is around 2 %

5.2.1 Compressibility

With compression to 20 GPa, the volume drops roughly monotonically (figure 5.7). This trend, however, is interrupted by two features: 9.5 GPa and 12.5 GPa. The corresponding compressibility values are plotted in figure 5.8 where the interruptions in the monotonic volume reduction can be seen as two distinct peeks. The compressibility value is considerably higher than usually reported for Im3m SOD[66] which is roughly 0.008. It should be noted that pure silica SOD is a versatile framework structure ([65]) where iso-symmetric changes between I43m and Im3m space groups often occur, depending on whether the sodalite cages are occupied or not ([65]). The difference between two space group can be observed from the Si-O-Si bond angle distribution ([67]). While Im3m has shorter range of angle distribution hence higher symmetry, the collective rotation of SiO_4 is forbidden associated with incompressibility of structure. However, even in the pure silica sodalite iso-symmetric changes can happen near ambient pressure and temperature ([67]). This is confirmed by the average bonding angle observed at 1 atm of SOD (figure 5.9). The average angle roughly 145 ° is considerably lower than the Im3m space group. Therefore it concluded that the starting point for this simulations is reasonably a compressible I43m SOD. Computational and experimental studies on SOD encapsulating ethylene glycol also indicate that with application of pressure the sodalite structure tends towards I43m. This is the crystalline

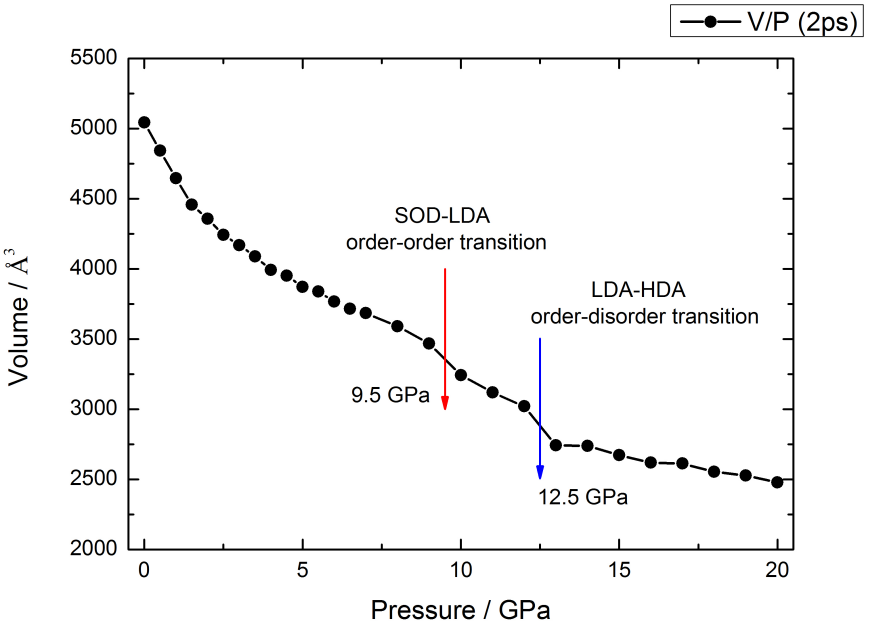

Fig. 5.7 Recorded volume around 2ps during compression with different pressure applied ranging from 1 atm to 20 GPa with an increment of 1 GPa. The volume decreases roughly monotonically while pressure increases despite two abrupt changing around 9.5 GPa and 12.5 GPa. Both turning point can be associated with phase transitions which are going to be confirmed in the changing compressibility (figure5.8).

phase which amorphized as pressure is increased further. Similar displacive phase transitions are familiar in the alpha-beta transitions in crystalline quartz at ambient pressure and elevated temperatures [68].

The following peaks at 9.5 GPa and 12.5 GPa can be attributed to collapse and amorphization respectively. Following the description of collapse and amorphization of ZIF8 (chapter 4), the peaks at 9.5 GPa and 12.5 GPa are ascribed to order-order transition between I43m sodalite and LDA sodalite, and order-disorder transition between LDA sodalite and HDA sodalite. These transitions will be confirmed later by considering the topology and ring structures (figure 5.12, 5.13, 5.14), as described earlier in considering collapse and amorphization of ZIF8.

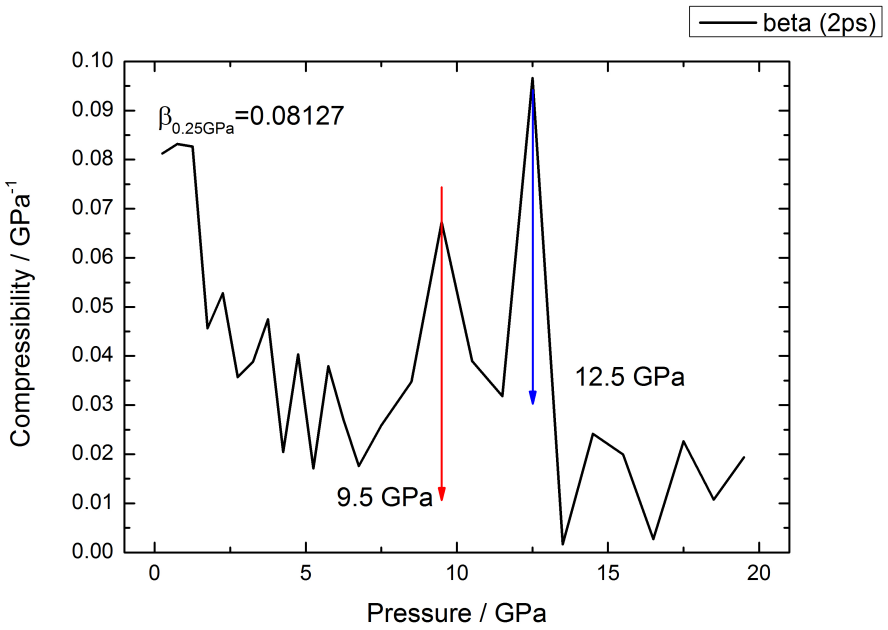

Fig. 5.8 Compressibility calculated from volume versus time. Two peaks occur around 9.5 GPa and 12.5 GPa. These are attributed to SOD to LDA, and LDA to HDA transitions respectively.

5.3 Radial distribution function

Following the consideration of the atomic structure of ZIF8 and its amorphized polytypes, the total RDF of SOD is plotted in figure (5.10). The first two sharp peaks at 1.67 Å and 2.69 Å are associated with the inter-atomic distances of the SiO_4 tetrahedra. These two features remain in the total RDF of LDA and HDA (figure 5.11). However the intensity of the peaks drop considerably suggesting increasing disorder coupled possibly with changes in coordination number of Si and O. The following weaker peak at 3.12 Å relates to Si-Si correlations across the oxygen bridging adjacent tetrahedra. Subsequent broader peaks at larger distances are made up of several interatomic distances relating mainly to Si-O and O-O correlations. As with ZIF8, these mask Si-Si correlations that define the interatomic distances within 4 fold rings and 6 fold rings, and therefore the sodalite cage topology (figure 5.1). Hence, the partial Si-Si RDF which defines this topology is shown in figure 5.12. Here the four fold rings diameter distance (4.33) can be identified along with the second and third nearest neighbour distances across the six fold rings. The changes in these distances and the occurrence

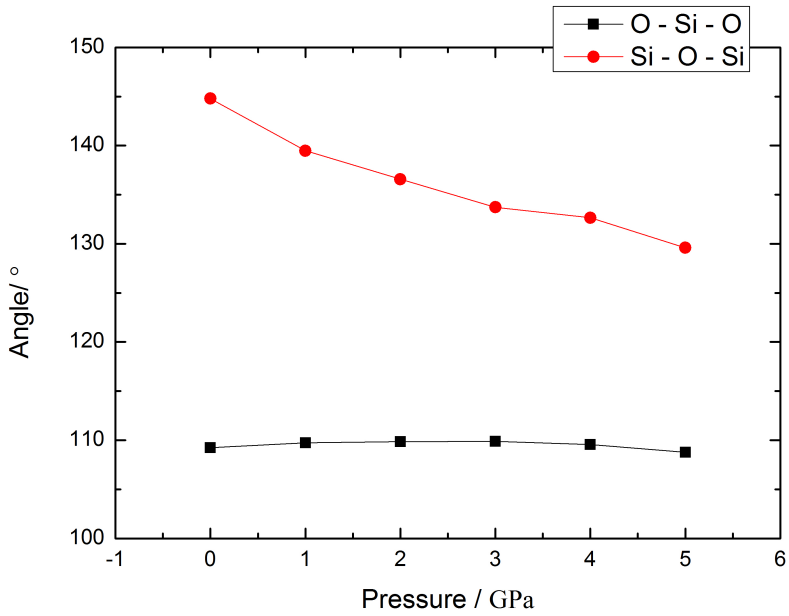

Fig. 5.9 Averaging angle recorded for different initial pressure. Si-O-Si decreases as pressure increases while O-Si-O remains almost unchanged. The values of Si-O-Si are close to what being reported for I43m SOD [67].

of peaks will be used to examine retention and disappearance of sodalite topology with the amorphization.

In the transition identified as LDA-HDA (figure 5.8), while the bridging oxygen Si-Si peak is broaden further still , virtually no other Si-Si peaks can be identified that can be attributed to the ring structure of sodalite cages. Interestingly, there is some relaxation in bridging oxygen angles (5.9) consistent with a break up of the four fold and six fold ring geometry.

Alongside the Si-Si RDFs, (figure 5.12to 5.14) projections with only Si interconnections of the structures are shown. These images identify the correlations between four and six fold rings that define the SOD structure. Although distorted, these are evident in the LDA structure, confirming the SOD-LDA transition at 9.5 GPa has been topologically invariant and therefore an order-order transition. At the higher pressure of 12.5 GPa, where the compressibility also increases and decreases dramatically, correlation between four and six fold rings disappear with the appearance of smaller and larger rings creating a dispersed topology.

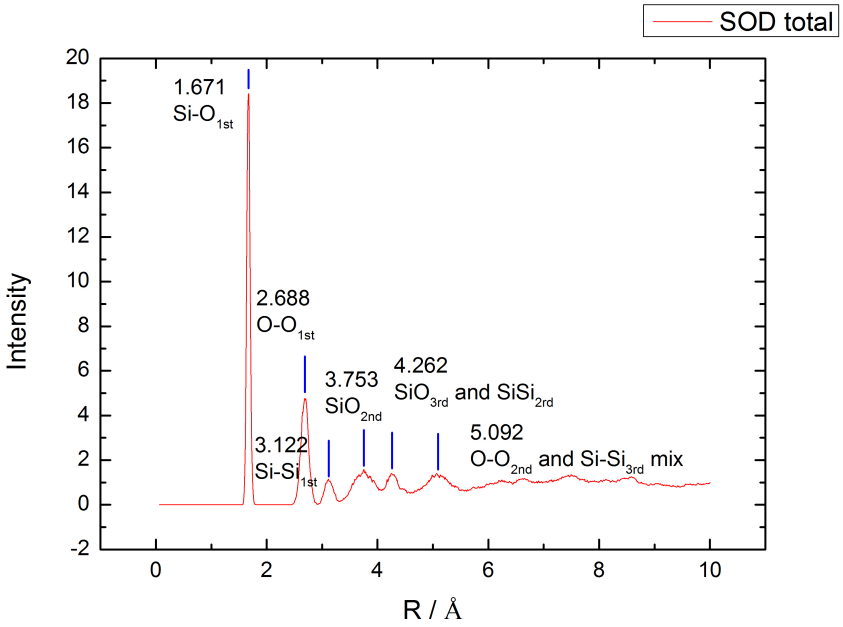

Fig. 5.10 Total radial distribution of SOD. Peaks are marked with blue vertical bars ascribed to different inter atomic distances.

Starting with the first transition, which is attributed to SOD-LDA order-order transition, (figure 5.13) the initial nearest Si-Si peak that defines the bridging oxygen angle broadens and shift to shorter distances. Subsequent peaks are much broader and weaker, indicating that sodalite cage persist but has become distorted. The decreases of distances is approximately 6 % which is insufficient to compensate for the dropping of volume (30 %) (figure 5.3,5.7). This indicates that considerable distortions are occurring in the bridging oxygen angles as well as the torsion angles, and therefore in the sodalite geometry. Figure (5.9) shows variation in the bridging oxygen angle and silicon tetrahedral angle with pressure from 1 atm to 5 GPa, where the tetrahedra remain virtually unchanged. The bridging oxygen angle, on the other hand, decreases significantly on compression, dropping to around 120 ° bridging oxygen are commensurate with the geometry of 3 fold rings, referred in the silica as tri-cluster. Figure 5.15 follows the fraction of bridging oxygens which begin to decrease from 100 % beyond 9 GPa where the SOD-LDA transition is complete. It levels out beyond 13 GPa where the LDA-HDA transition finishes. Beyond 9 GPa, significant fraction of three fold coordinates oxygens emerge. Three fold coordinate oxygens indicate bond reformation taking place. It commensurate with the bridging oxygen angle of 120 ° and three fold silica rings-tri-clusters.

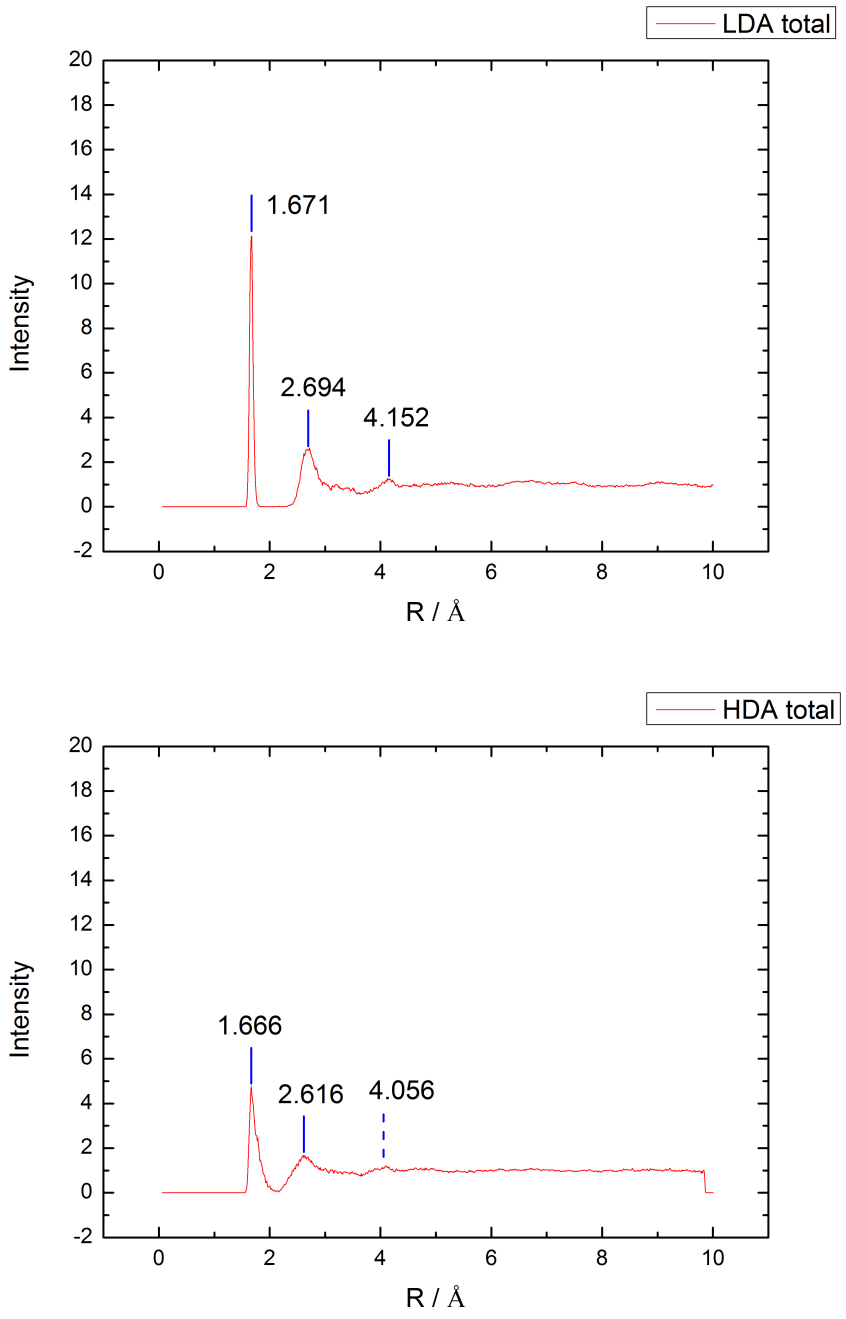

Fig. 5.11 Total radial distribution of LDA at 9 GPa and HDA at 13 GPa. The first two peaks persist through both phase transition while the intensity of peaks drop.

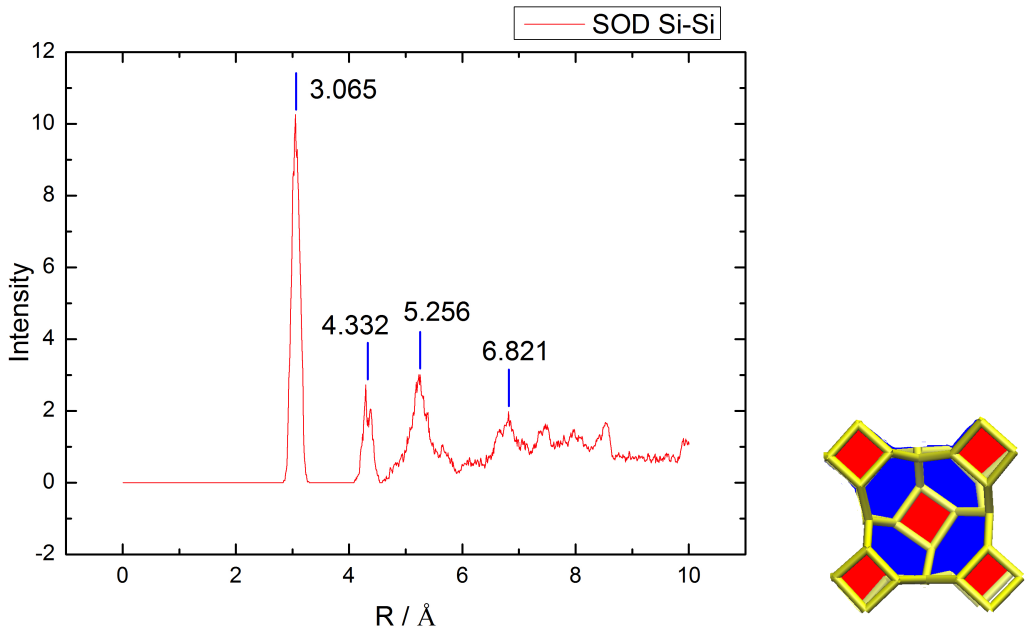

Fig. 5.12 Si-Si radial distribution function of crystalline SOD. Peaks marked by vertical bar are attributed to the 1st,2nd,3rd,4th neighbour which are close to the crystallographic distances recorded earlier this chapter (figure 5.1).

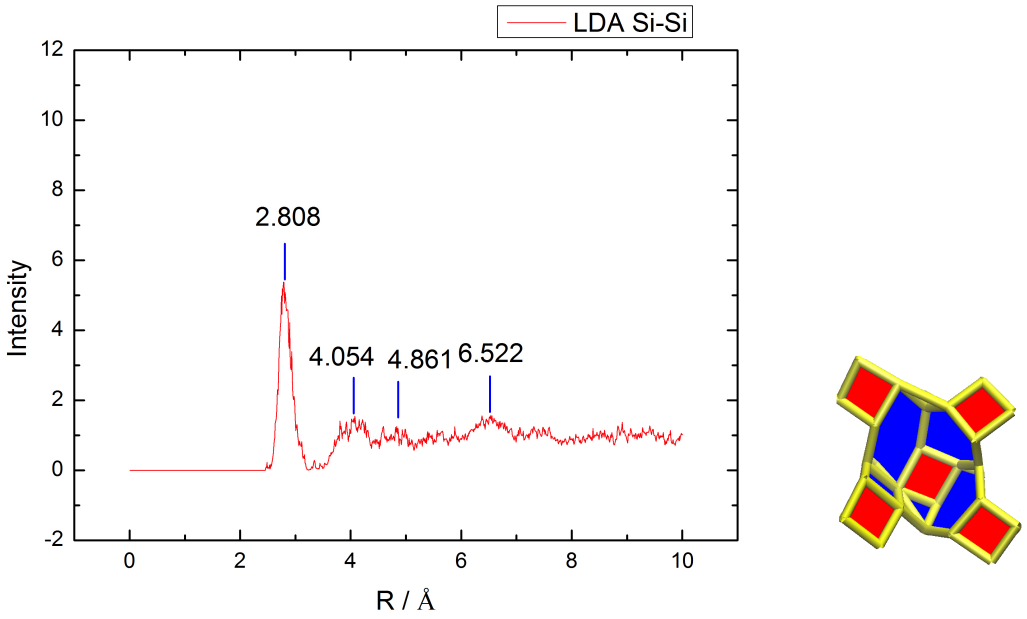

Fig. 5.13 Si-Si radial distribution function of pressure-induced amorphization phase LDA. Majority of the peaks from SOD remain while shifting slightly to the left indicating the shrinking of volume. Moreover, the deformation of rings broaden the peaks reducing the symmetry of structure as shown in snapshots figure 5.18

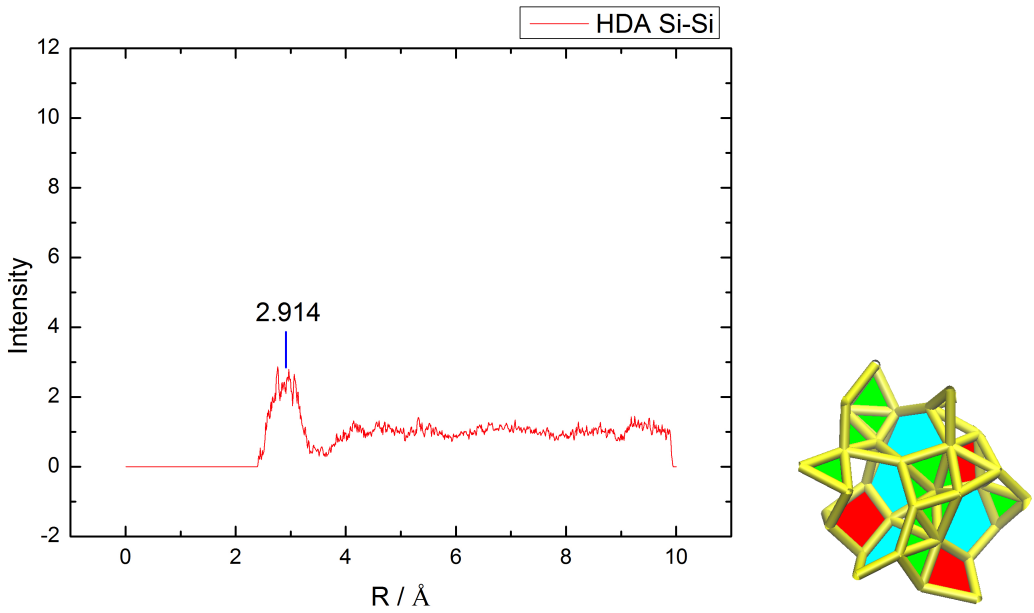

Fig. 5.14 Si-Si radial distribution function of pressure-induced amorphization phase HDA. Almost all the peaks flatten out or disappear except for the first peak corresponding to the nearest Si-Si neighbour

These changes in coordination are more dramatically seen in the coordination number of Si (figure 5.15). In particular, beyond 9 GPa the fraction of tetrahedral sites drops, decreasing even more dramatically at 13 GPa. At the same time, the 5 fold coordinated Si sites emerge at 9 GPa, rising sharply again at 13 GPa. In addition, the 6 fold coordinated Si sites appear beyond 13 GPa. The falling in the fraction of tetrahedral sites replaced by 5 then 6 fold coordinated Si sites shows even more clearly the changes in network bonding that occur through the SOD-LDA-HDA transitions. It is expected that these coordination changes will be manifest in topological changes.

As has been demonstrated previously in the ZIF8 study (chapter 4), projections of the Si network (figure 5.12,5.13,5.14) are used to explore topological changes. This uses the four (coloured red) and six (coloured blue) fold ring geometry of the sodalite network as the starting point. These rings and their configurations are retained in the LDA phase, as expected from the persistence of tetrahedral Si and bridging oxygen geometries. However, with the breaking of bonds and their reformation corresponding with falling of tetrahedral Si and two fold coordinated oxygen beyond the LDA transition (figure 5.15), the sodalite topology is completely lost. 5 fold rings (coloured cyan) and 3 fold rings (coloured green) dominate at HDA to the exclusion of 6 fold rings (figure 5.14). High pressure Brillouin scattering of silica reveals a sharp increase in Poisson's ratio levelling out by approximately 12-15 GPa ([69]). This increase has been attributed to

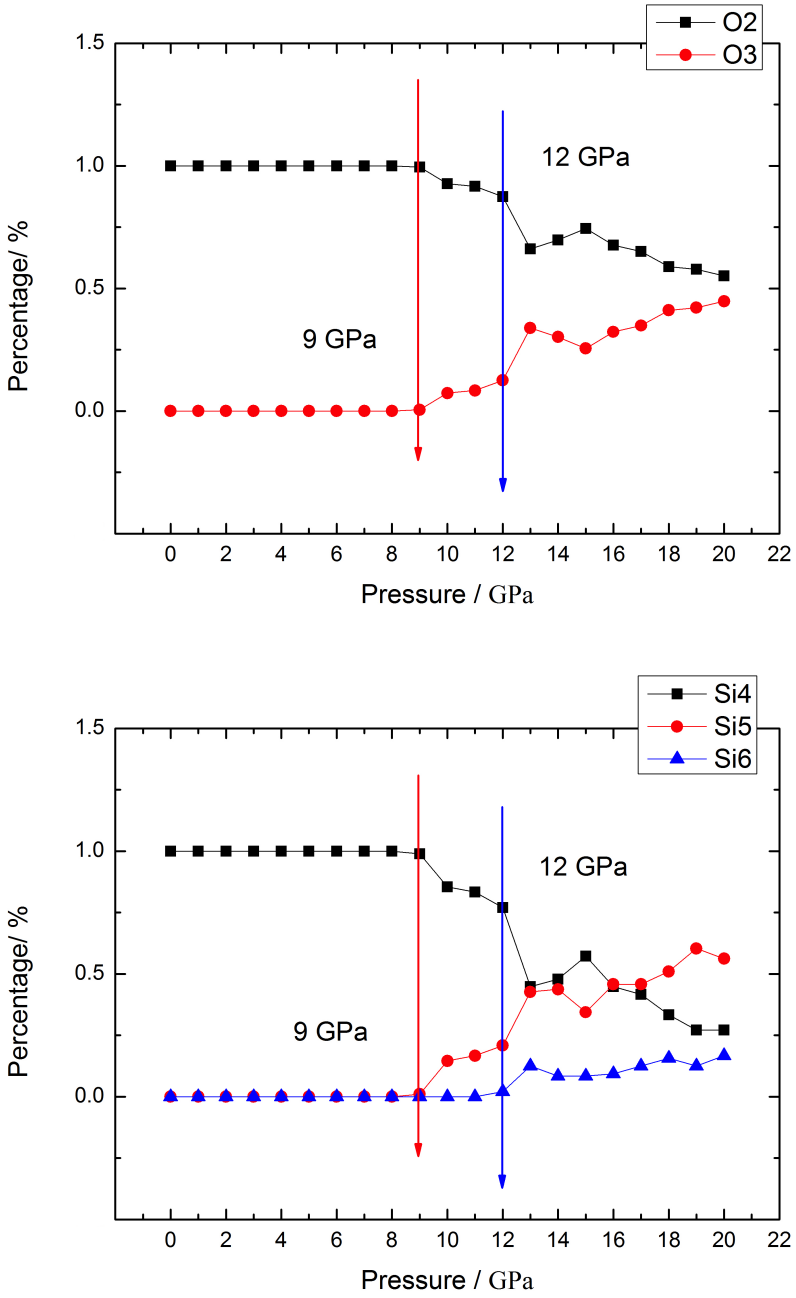

Fig. 5.15 Coordination number of compressed structure for Si and O at different initial pressure. Red arrow and blue arrow mark SOD-LDA transition and LDA-HDA transition respectively. The coordination number for both Si and O change dramatically around these two phase transition confirming topology difference between differed phases.

formation of an HDA phase [61]. It could be assumed that these high pressure phases may have similar topologies with the emergence of smaller ring sizes due to bond breaking and reformation. In the Brillouin scattering study, reversibility in the sound velocities was reported when decompressed back to ambient pressure.

5.3.1 Decompression to 1 atm

As in the ZIF8 study, the effect of decompression have also been examined starting with both HDA and LDA. Decompression to ambient pressure from HDA (figure 5.16) results in encouraging comparasion with the RDF obtained on compression. The Si-Si distances all increases commensurate with the different pressures. Nevertheless, correlation peaks are weaker and broadened. They remain defined for the four fold ring diameter (4.248) but are much weaker for second and third neighbour across six fold rings (5.053 and 7.122 respectively).

Turning to the decompression from LDA to SOD, the restoration of the sodalite structure is very convincing, with all correlation associated with four and six fold rings can be identified at almost identical positions and intensities expected at ambient pressure.

Finally, the topological changes accompanying the RDF changes (figure figure 5.17) are shown in 5.18 where they are compared with those occurring under compression. 3,4,5,6 fold rings are coloured following same scheme as earlier in compression. Restoration of LDA from HDA is not entirely complete, although the sodalite cage structure containing adjacent four and six fold rings is established. As concluded earlier considering Si-Si RDFs (5.17), the ultimate SOD structure obtained from decompressing LDA is virtually the same as the starting crystalline structure. As concluded earlier in the ZIF8 study (chapter 4), the collapse and amorphization of sodalite under pressure can be reversed when this is released.

5.4 VDOS on compression and decompression

Vibrational density of states are calculated for sodalite bcc and LDA at 9GPa and HDA at 13 GPa under compression (figures 5.19,5.21,5.22 respectively). In the plot of SOD (figure 5.19), 9 modes can be identified. Considering earlier experiments and

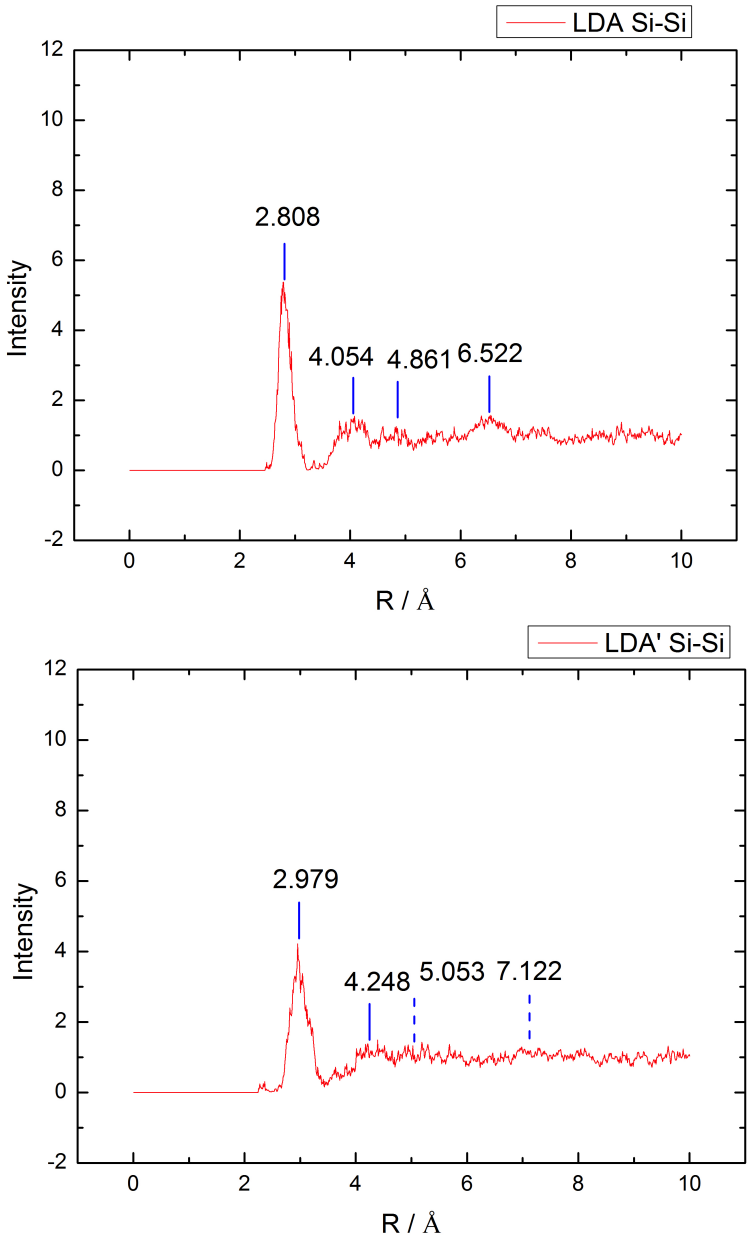

Fig. 5.16 Radial distribution function of compressed LDA and restored LDA from HDA decompressed to a pressure of 1 atm. The first and second peaks are found to be restored while third and fourth peaks become vague due to mixing with other interatomic correlation.

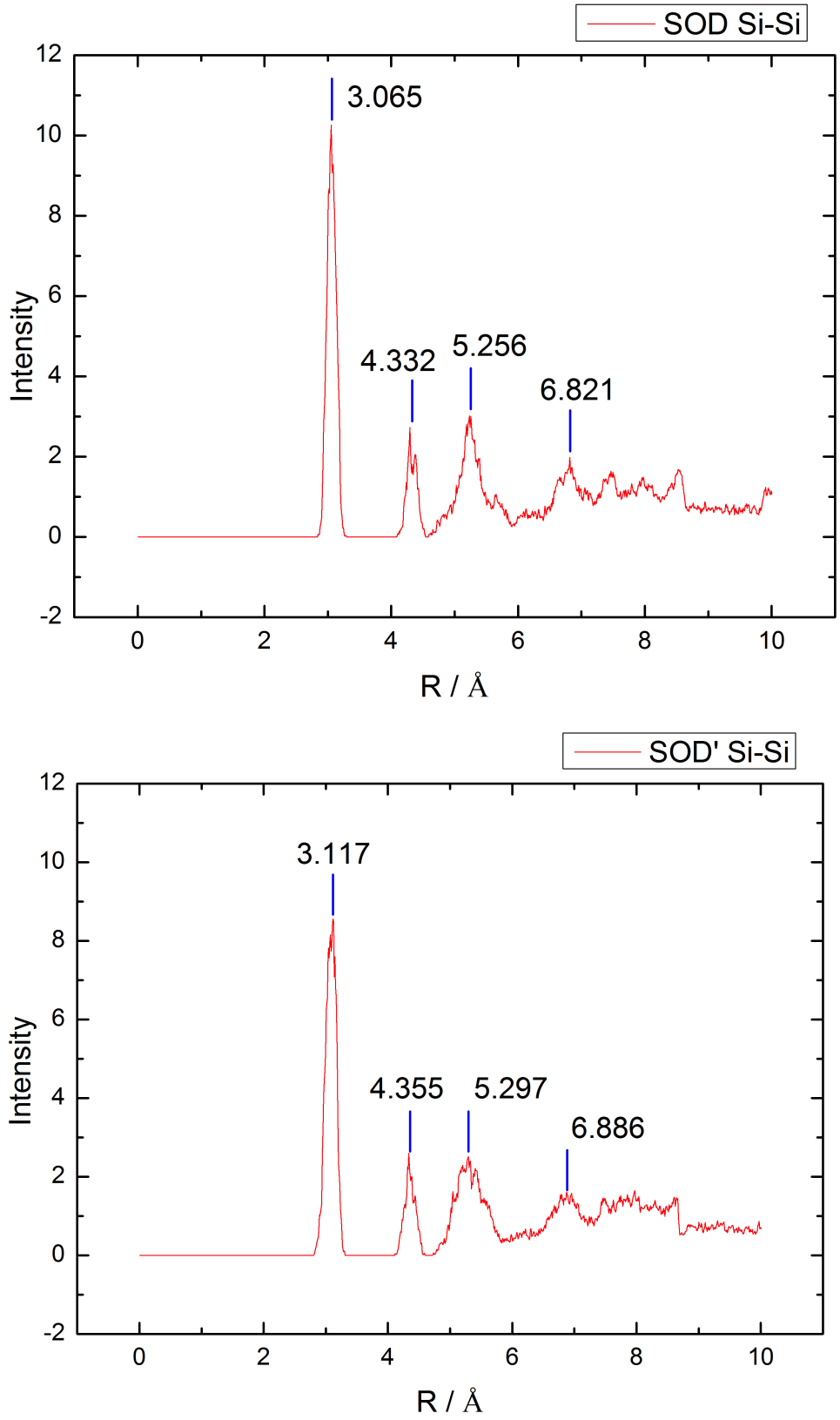

Fig. 5.17 Radial distribution function of initial crystalline SOD and restored SOD from LDA decompressed to a pressure of 1 atm. All peaks from initial structure are observed in the restored SOD in good agreement.

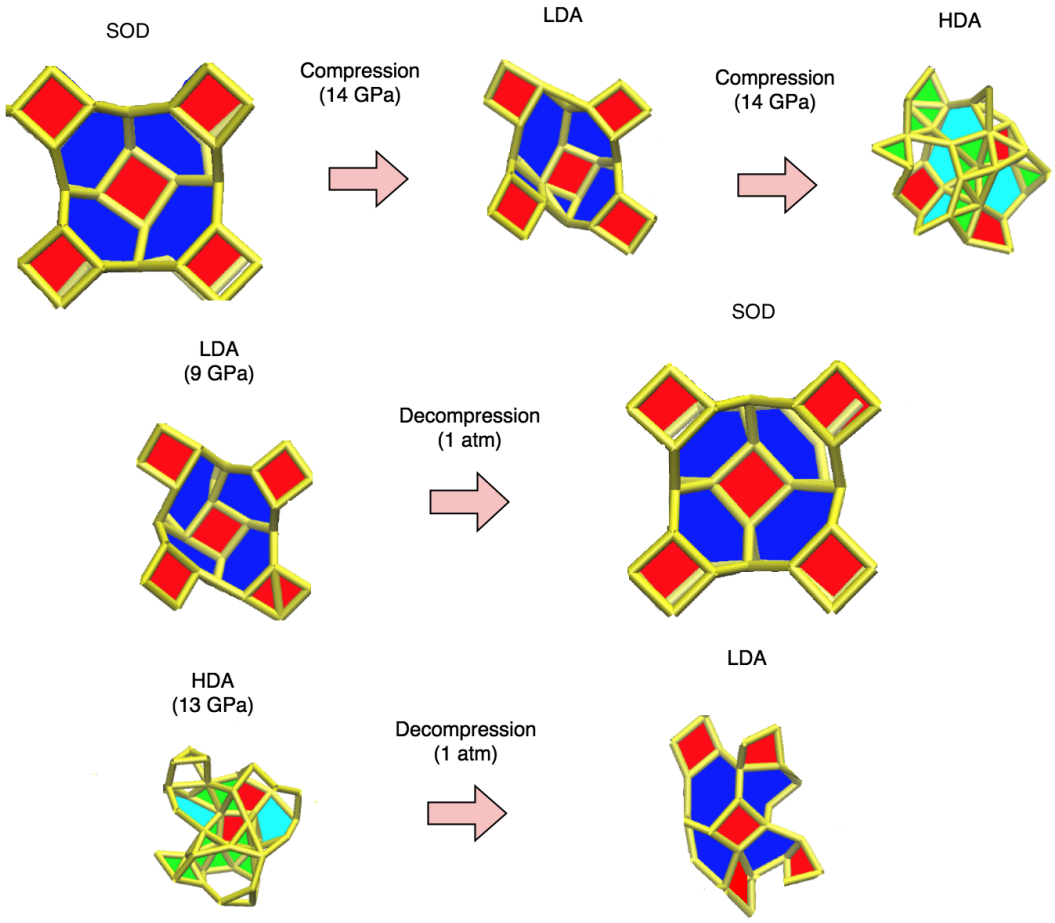

Fig. 5.18 Top: Compression of 14 GPa following phase transition SOD-LDA and LDA-HDA Middle: LDA structure decompress at 1 atm to the LDA phase Bottom: HDA structure of 13 GPa decompress at 1 atm to the LDA phase. The snapshots shows significantly change between phase especially transition between LDA and HDA. In compression, the number of four and six fold rings persistent through SOD to LDA then eventually lost in HDA. With decompression, almost identical ring structure can be restored from LDA to SOD while the restored LDA from HDA is not identical to the original LDA on compression but similar ring topology can be identified.

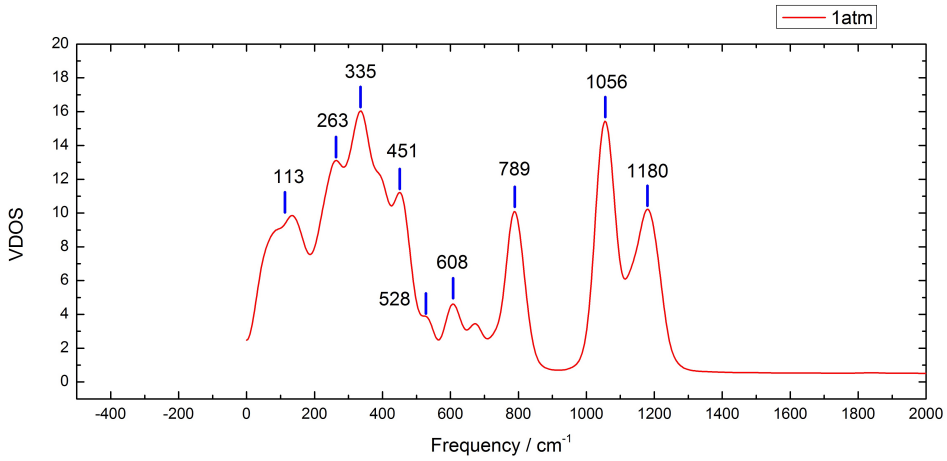

Fig. 5.19 Vibrational density of state of SOD. Peaks marked in the plot potentially can be attributed to different modes of motion. 113 cm^{-1}: Boson peak 335 cm^{-1}: oxygen rocking 451 cm^{-1}: four fold rings 528 cm^{-1}: three fold rings 608 cm^{-1} and 789 cm^{-1}: O-Si-O bending 1056 cm^{-1} and 1180 cm^{-1}: Si-O stretching vibrations (TO and LO)

calculations of silica glass [70], the two high frequency modes 1056 cm^{-1} and 1180 cm^{-1} can be ascribe to optical transverse and longitudinal Si-O stretching vibrations (TO and LO) respectively. The intermediate modes at 451 cm^{-1}, 528 and at 608 cm^{-1} occur at frequencies close to features found in VDOS of silica [70] which have been attributed to four-fold rings and three-fold rings. While four-fold rings occur in the sodalite structure, three fold rings are not present. In the present context therefore the feature at 608 cm^{-1} might be interpreted as a transverse O-Si-O bending vibration complimenting the 789 cm^{-1} mode interpreted as longitudinal O-Si-O bending. The features at 451 and 528 cm^{-1} may be attributed to a splitting of four fold ring modes around 500 cm^{-1}. This I43m crystalline phase was recorded as less rigid than Im3m due to the increased flexibility of Si-O-Si bonding. The major peak at 335 cm^{-1} which is present in the vibrational density of states of silica glass can be interpreted as the rocking of oxygens around tetrahedral Si [70]. For bcc SOD the mode at 283 cm^{-1} may due to the scissoring of oxygen pairs considering the less rigidity of bonding of bridging oxygen. Finally, the lowest frequency mode at 113 aligns approximately with the boson peak feature found in silica glass, ascribed to collective liberations between adjacent tetrahedra sharing common bridging oxygens [71].

Individual VDOS of Si and O is shown in figure 5.20. It is clear that the intermediate modes within the range of 500 cm^{-1}-1000cm^{-1} are mainly contributed by the motion of Si. This commensurate with conclusion being made for attributing the intermediate modes to Si bending motion (figure 5.19). This contrasts with the VDOS for ZIF8

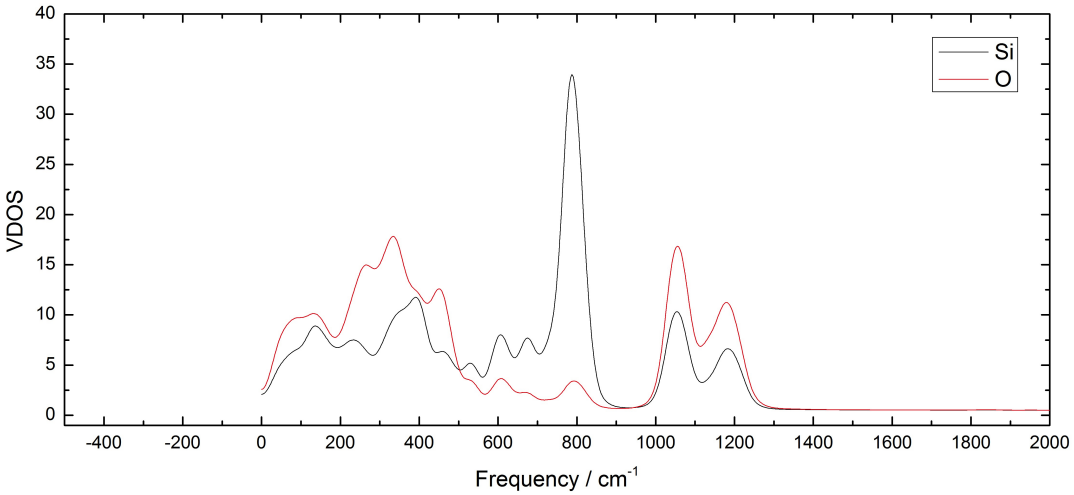

Fig. 5.20 VDOS for individual atom species of SOD at ambient pressure. The intermediate frequency modes between 500 cm^{-1} and 1000 cm^{-1} is mainly contributed by Si while O is stronger in lower frequency band as well as the splitting dual peaks at around 1050 cm^{-1} and 2000 cm^{-1}. black: Si red: O

where most of the features relate to the imidazolate linkage, which is equivalent to oxygen in SOD. However, in silicates oxygen is a less rigid linkage than imidazolate group in hybrid materials. It means that inter-tetrahedral correlations are weaker for SOD (5.12,5.13, 5.14) than for ZIF8. This is also reflected in the response time evident in the change of volume with time for a given applied pressure - compare 5.4 with (figure 4.4, chapter 4). On average it is 100 to 200 % faster to reach the equivalent volume for the amorphous phases LDA and HDA for SOD than for ZIF8. At the same time the pressures to achieve these transformations are 4 or 5 times larger for SOD than for ZIF8, suggesting that SOD and its amorphous phases have far more torsional rigidity than ZIF8 and its polymorphs.

Figure 5.21 shows the VDOS of compressed LDA. Although the intensities of peaks become weaker, most of the major peaks in SOD retains through order-order phase transition with minor shifting in frequency. Additionally, the peak at 232 cm^{-1} become more prominent. Attributed to oxygen scissor motion , this suggests that the LDA phase includes more distortion around bridging oxygens than SOD.

Figure 5.22 shows the VDOS of compressed HDA. Most of the modes observed disappear except for the rocking mode at 411 cm^{-1}, the intermediate Si-O-Si bending mode at 711 cm^{-1} and the combined optical mode for Si-O stretching. The RDF of restored LDA from decompression the HDA at 1atm (figure 5.16) shows that the transition of topology between LDA and HDA is reversible. Additionally, reappearing of certain

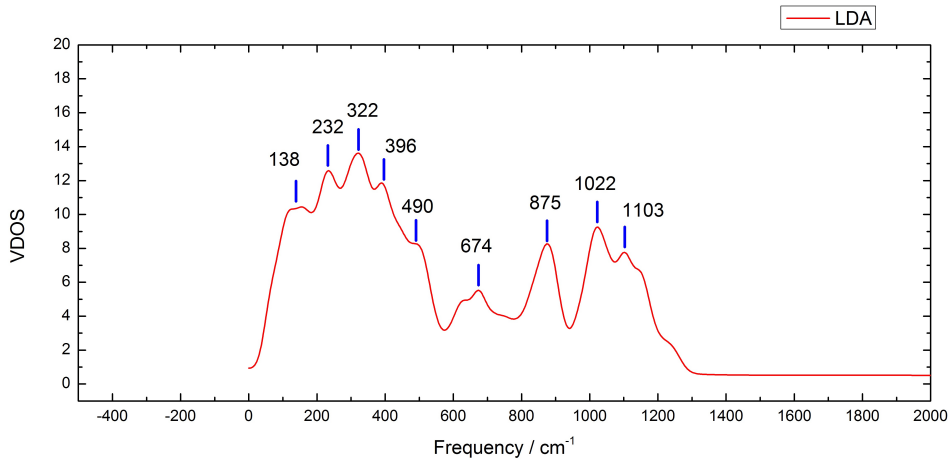

Fig. 5.21 VDOS of LDA at 9 GPa. 8 modes, except for the one at 232 cm^{-1}, similar to what observed at ambient pressure are marked.

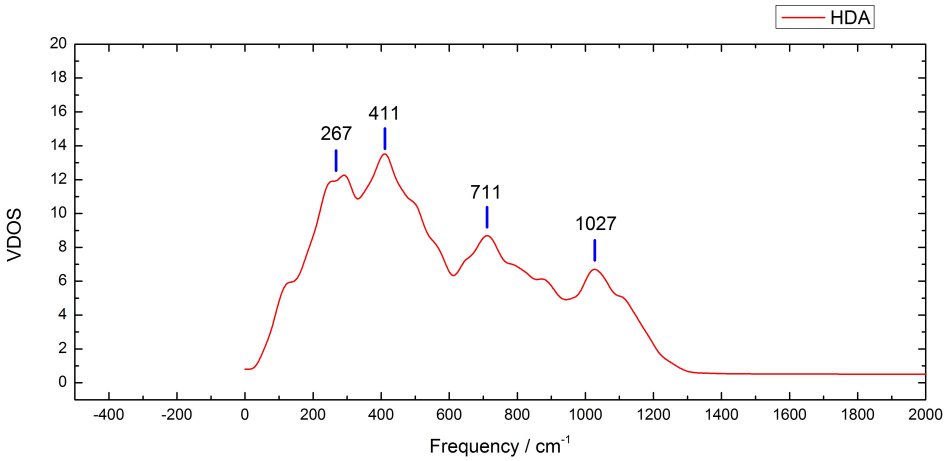

Fig. 5.22 VDOS of HDA at 13 GPa. Most of peaks disappear due to the lost of SOD ring topology in HDA phase.

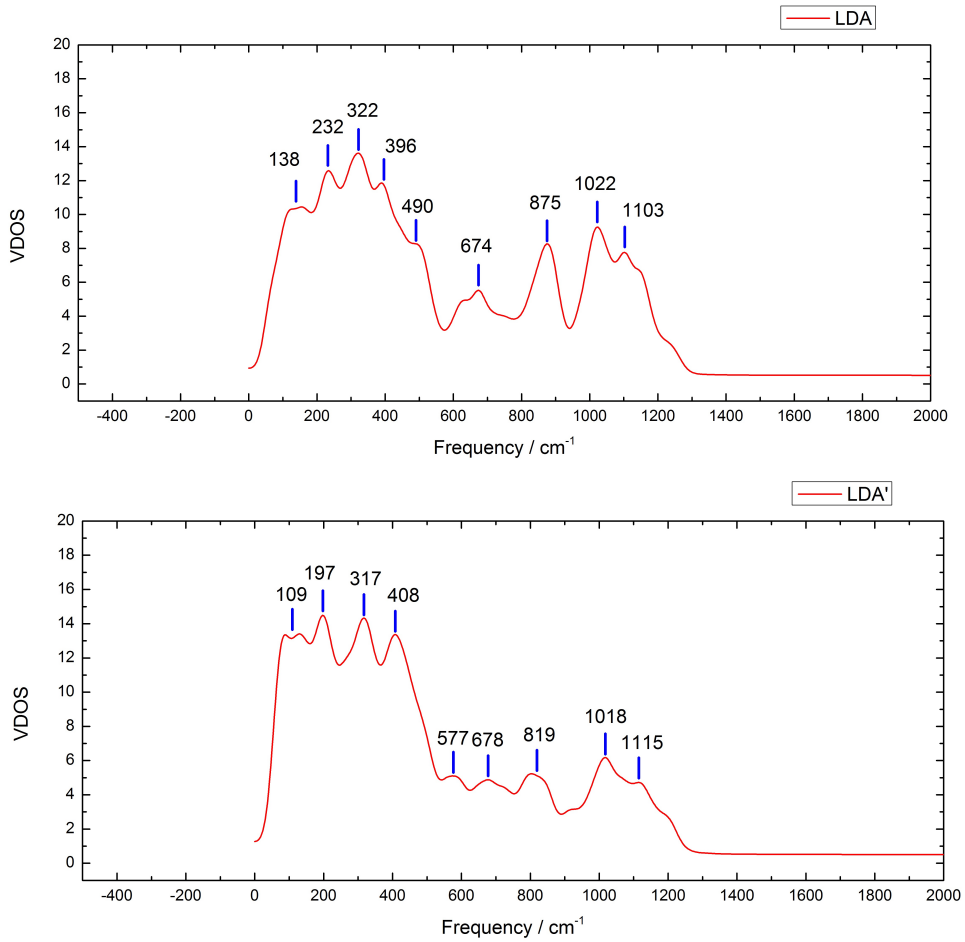

Fig. 5.23 VDOS of compressed LDA and restored LDA from HDA decompressed at 1 atm. Similar modes can be observed for restored LDA with varied intensity.

modes in the VDOS of restored LDA (figure 5.23) indicates that the restoration of the motions of oxygen rocking (335 cm^{-1}), O-Si-O bending (819 cm^{-1}), Si-O stretching (1018 cm^{-1} and 1115 cm^{-1}) can also be obtained.

Figure 5.24 shows the VDOS of restored SOD from LDA to 1atm. All of the peaks recorded for SOD can be found with small deviation in peak frequency within the error range. This indicates a great reversibility of phase transition between SOD and LDA. Together with the RDF of restored SOD (figure 5.17), it can be concluded that the restored structure is close to the highly compressible bcc SOD structure belonging to I43m space group.

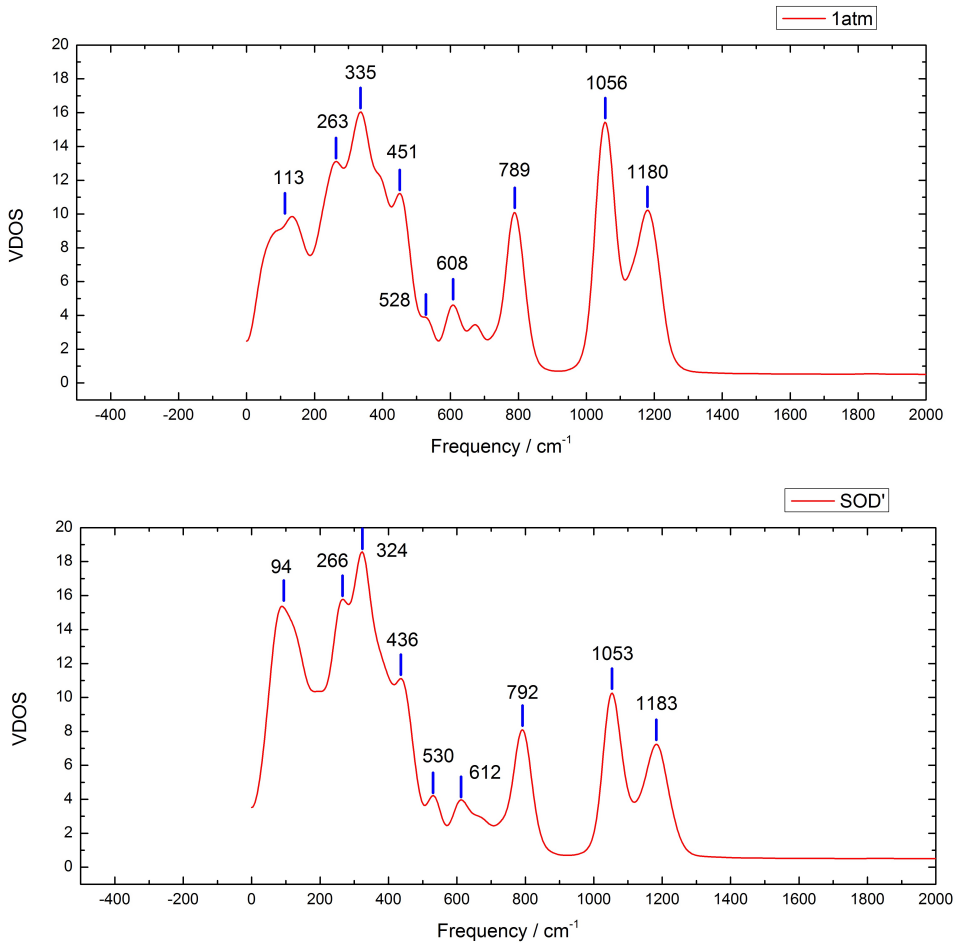

Fig. 5.24 VDOS of initial SOD and restored SOD from LDA decompressed at 1 atm. Almost identical spectrum is observed indicating the similarly between restored SOD and initial crystalline SOD.

CHAPTER 6

CONCLUSION AND FUTURE WORK

6.1 Conclusion

The research presented here has involved the application of classical molecular dynamics and ab initio DFT to examine the structure and dynamics of glasses, melts and the amorphization of network nano-porous crystals. Specifically work has concentrated on oxide alumino-silicates based around nepheline composition ($KNa_3Si_4Al_4O_{16}$). In addition to the structure of melt-quenching glasses formed with these compositions, simulations have also been made of ion diffusivity and viscosity for the first time in the multi-cation alumino-silicates. Two nano-porous crystalline systems have also been examined under amorphization conditions using increasing and also decreasing pressure: zeolitic imidazolate framework 8 (ZIF8) and pure silica sodalite (SOD). Both the hybrid ZIF8 and the inorganic SOD crystals share the same structure (β-cage). These study have revealed similar phase transitions from the crystalline to the fully amorphous phase but at very different pressures. These transitions are reversed when the pressure is removed. Conclusion on each of these three areas will now be presented, then a discussion of future work will follow.

6.1.1 Nepheline

1. A model of nepheline based on classical interatomic potential was successfully constructed. A combined potential based on two BKS potential [48][47] with partial charges was chosen for the inter-atomic interaction of molecular dynamics simulation. Alumino-silicates including nepheline and its variations have been simulated to obtain the structure of the melts and glasses. Verification at ambient temperature confirmed that model successfully replicate the crystallographic structure with a slight difference of volume (3.4 %).

2. Radial distribution functions including total RDF and partial RDFs were calculated to explore the atomic structure of these alumino-silicate glasses. With evidences from RDF, Lowenstein's Rule shown to be violated through out. The Al-O-Al bonds appear to be around 30 % of the total T-O-T bonds.

3. Snapshots confirmed the clustering of mobile ions at all alkali concentrations in nepheline. The percolation threshold of alkalis within the accessible free volume is reached at 68 %. In this study, 75 % and 100 % K corresponds to structures for which percolation threshold is exceeded.

3. Diffusion constant and viscosity were calculated. The results derived from Eyring relation closely match the viscosity values predicted by a fitting model based on Adam-Gibbs theory (modelled by Charles Lelosq, Australian National University). Again, sharp increases of viscosity were observed beyond 75 % K in agreement with the experiment result at much lower temperature close to the glass transition. This suggests that the existence of percolation channels modifies the framework atoms which influences the rising viscosity.

4. Vibrational density of states was calculated for various compositions. Modes ascribed with different motions within glasses structures were observed. These modes are similar to ones observed in Raman spectroscopy, ranging from the low frequency mode at 100 cm^{-1} ascribed to the boson peak to the high frequency mode at 1000 cm^{-1} ascribed to T-O stretching.

6.1.2 ZIF8

1. A classical model based on pre-described empirical potentials for ZIF8 was constructed from an early study[57]. Compression using different pressures (from 1 atm to 1.2 GPa) on such a system were successfully performed. To demonstrate this, some realistic MD shots based on simulated compressed structure were produced for a research on hybrid glasses[57]. Due to the bonding term existing in most of the potentials used in the literature, higher pressures of compression proved to be impractical in simulations performed because of the inconsistency of simulation cell.

2. To overcome the limitation of classical methods, DFT was used instead for modelling the ZIF8 with the codes of CP2K. The MD shots of similar super cell to the classical calculations, the molar volume and radial distribution function from ZIF8

at ambient conditions were obtained. A good agreement with the previous MD study was achieved. Also it successfully reproduced the experimental observed pressure (1.2 GPa) for the onset of the amorphization. Besides that, higher pressures of compression were carried out and as a result a fully amorphous phase of ZIF8 was achieved.

3. During the compression of ZIF8, two phase transitions can be spotted from the volume-time relations with different applied pressures. Furthermore, the equilibrated volume, extracted from all the runs, decreases monotonically with increasing pressure, except for two major non-linear variations. Those non-linear changes can be associated with changes in compressibility where two peaks representing phase transitions are observed: crystalline ZIF8 to low density amorphous phase (LDA) and low density amorphous phase (LDA) to high density amorphous phase (HDA). For clarification in extracting the MD snapshot of three phases, a simplification has been made to the structure that only Zn-Zn connections are considered. Accordingly, the peaks observed in RDFs can be associated with the distances between different pair of neighbouring Zn within four fold rings and six fold rings. Projections of this simplified structure reveal the similarity in ring topology between ZIF8 and LDA, with a sharp increase in disorder when the HDA phase equilibrates.

4. Decompression from HDA phase to LDA phase, and LDA phase to crystalline phase have been observed when the pressure was reset to 1 atm. The results including RDF, VDOS spectrum and MD shots confirm the existence of the intermediate phase LDA being topologically very close to the ZIF8 crystalline phase. Furthermore, the reversibility of both phase transitions have been proved possible depending on the initial pressure applied for compression. These observations suggest a possible way of producing special LDA glasses of ZIF8 with high porosity.

6.1.3 Sodalite

1. Crystal of pure-silica sodalite (SOD) has been simulated using DFT methods. A starting simulation at ambient pressure shows that volume of crystalline SOD is 10 % lower than crystallographic SOD belonging to Im3m space group. Evidences support the contention that SOD near starting point of these simulations belongs to the considerably compressible I43m space group, rather than highly symmetrical Im3m.

2. Two phase transitions, including SOD to LDA and LDA to HDA, were observed, similar to two phases in ZIF8 under pressure. Compared to ZIF8, sodalite has a more

rigid structure associating with the higher initial pressure required for phase transition (9.5 GPa). Compressibility plot based on equilibrated volume with different initial pressure was obtained. Two peaks were observed at 9.5 GPa and 12.5 GPa ascribing to phase transitions, I43m SOD to LDA and LDA to HDA respectively.

4. Angle distribution and coordination number were calculated. The angle distribution confirms that the starting point of SOD crystal belongs to the compressible I43m space group. The coordination number, in which the number of four coordinated Si largely become first five coordinated above 9.5 GPa then six coordinated above 12.5 GPa. These coordination changes mirror the changes in compressibility.

5. Radial distribution function, including total RDF and Si-Si RDF, were calculated for exploring the topological difference between the three phases. In particular, like with ZIF8 and Zn-Zn RDFs, the peaks of Si-Si RDFs can be associated with different neighbouring pairs between Si within the 4 fold rings and 6 fold rings. MD shots including the central sodalite cage were plotted to demonstrate these topological changes in both compression and decompression.

6. Vibrational density states, together with RDF distribution function obtained at 1 atm for decompression support the contention that both phase transitions (SOD to LDA, LDA to HDA) are reversible. Modes, including boson peak, rocking, bending, stretching vibrations, were observed to be similar to the vibrational density of states of silica.

6.2 Future work

Although this study successfully solved the problems of immediate interest in aluminosilicate glasses and melts and predicted entirely new phase transitions in pressure-induced amorphization of hybrid and inorganic sodalite structures, there are inevitably improvements that would be possible in the future.

Technically, with increased HPC capacity, larger simulation box or ab initio simulations can be anticipated as outlined below. On the other hand, alternative methods of obtaining same physical properties, including viscosity and elastic constant, will be possibles.

6.2.1 Nepheline

1. A compromise was made in the cell size to 1512 atoms with a maximum number of 64 CPU cores being used. This was trying to obtain the structure and dynamics given the available resources initially of *Holly* cluster in the department and subsequently of HPC Wales. With a larger simulation box, average statistic structure would have been better defined in terms of peaks in pair distribution function. In addition, it would have given access to larger number of rings with a larger simulation cell. However, to calculate the dynamics with the computational sources available at HPCWales, a larger cell would have been extremely restrictive in the number of steps available for calculating the Mean Squared Displacement (MSD) and Velocity Autocorrelation Function (VAF). Given the real time performance of 1 hour per ns, in order to run each composition for more than 50ns, runs exceeding 50 hours were prohibited by the time limit of a single job.

2. If ab initio methods were used in place of classical MD, this is likely that closer agreement with experiments would have been possible. This is because the reliance on empirical inter-atomic potentials in classical MD requires adjustments such as the pressure 0.3 GPa needed to converge on the crystalline structure. This can lead to uncertainty in important dynamics, such as viscosity and vibrational density of states. At the same time, because ab initio methods are based on quantum behaviour of electrons, structure and dynamics may be better predicted. The price for this though is the limitation of atomic numbers and simulation time. Additionally much smaller simulation cell would restrict the lowest frequency in VDOS, for example, as larger rings sizes would be excluded.

3. Two empirical relations were used for deriving the viscosity - Brownian motion relation (3.4) and Eyring relation (3.6) which are both classical. An alternative and well regarded method would be the Green-Kubo relation [72][73] based on the velocity autocorrelation function combining with the pressure autocorrelation function. This converges on the viscosity directly without working through the two empirical relations. In particular, the assumption made in this study, that the total diffusivity and viscosity are the average over individual atom dynamics scaled by the numbers of each species, would no longer be necessary.

6.2.2 ZIF8

1. The resolution of VDOS can be improved by extending the simulation time. This can possibly increase the accuracy of attributing the peaks to certain motion of bending, stretching and wagging. With the knowledge of peak-motion relation, tracking the influence of amorphization on rings motion and deformation can become easier and more detailed than at this stage.

2. The topology of LDA phase has similar features to the re-entrant topology of negative Poisson ratio materials reported. Confirmation can be attempted by calculating the Poisson ration directly from the stiffness matrix based on strain-energy method.

6.2.3 Sodalite

1. The compressibility of the starting point is considerably higher to what is reported in other research [66]. Evidences in this study show that this is possibly due to the changing of SOD structure between Im3m and I43m at pressures close to 1 atm. If an alternative scheme of DFT was developed that restricted the Si-O-Si bound angle, it might be possible to obtain a equilibrated structure of Im3m SOD at ambient pressure.

2. As with ZIF8, if stiffness matrix was derived for SOD and its amorphous phases, auxetic (negative Poisson ratio) properties could be explored. Furthermore, the pressure dependence of sodalite could be contrasted with the pressure dependence of silica glass- both share the same compositions, but differ in ambient pressure density.

REFERENCES

[1] G Neville Greaves and Kia L Ngai. Reconciling ionic-transport properties with atomic structure in oxide glasses. *Physical Review B*, 52(9):6358, 1995.

[2] Picture of snow flake. http://photography.nationalgeographic.com/wallpaper/photography/photos/patterns-snow-ice/sectored-snowflake/. Accessed: 2015-12-20.

[3] Bravis lattices of cubic system. https://en.wikipedia.org/wiki/Bravais_lattice. Accessed: 2015-12-20.

[4] Norman Neill Greenwood and Alan Earnshaw. *Chemistry of the Elements*. Elsevier, 2012.

[5] Gérard Férey. Hybrid porous solids: past, present, future. *Chemical Society Reviews*, 37(1):191–214, 2008.

[6] Ch. Baerlocher and L.B. McCusker. Database of zeolite structures. http://www.iza-structure.org/databases/, 1996.

[7] Sung Keun Lee and Jonathan F Stebbins. The degree of aluminum avoidance in aluminosilicate glasses. *American Mineralogist*, 84(5-6):937–945, 1999.

[8] Henk Van Koningsveld. *Compendium of Zeolite Framework Types: Building Schemes and Type Characteristics*. Elsevier, 2007.

[9] TB Reed and DW Breck. Crystalline zeolites. ii. crystal structure of synthetic zeolite, type a. *Journal of the American Chemical Society*, 78(23):5972–5977, 1956.

[10] Joseph O Hirschfelder, Charles F Curtiss, Robert Byron Bird, and Maria Goeppert Mayer. *Molecular theory of gases and liquids*, volume 26. Wiley New York, 1954.

[11] BF Hoskins and Richard Robson. Design and construction of a new class of scaffolding-like materials comprising infinite polymeric frameworks of 3d-linked molecular rods. a reappraisal of the zinc cyanide and cadmium cyanide structures and the synthesis and structure of the diamond-related frameworks [n (ch3)

4][cuiznii (cn) 4] and cui [4, 4', 4", 4"'-tetracyanotetraphenylmethane] bf4. xc6h5no2. *Journal of the American Chemical Society*, 112(4):1546–1554, 1990.

[12] Bernard F Hoskins and Richard Robson. Infinite polymeric frameworks consisting of three dimensionally linked rod-like segments. *Journal of the American Chemical Society*, 111(15):5962–5964, 1989.

[13] Gérard Férey, Christian Serre, Caroline Mellot-Draznieks, Franck Millange, Suzy Surblé, Julien Dutour, and Irène Margiolaki. A hybrid solid with giant pores prepared by a combination of targeted chemistry, simulation, and powder diffraction. *Angewandte Chemie*, 116(46):6456–6461, 2004.

[14] Hiroyasu Furukawa, Kyle E Cordova, Michael O'Keeffe, and Omar M Yaghi. The chemistry and applications of metal-organic frameworks. *Science*, 341(6149):1230444, 2013.

[15] Jin Chong Tan and Anthony K Cheetham. Mechanical properties of hybrid inorganic–organic framework materials: establishing fundamental structure–property relationships. *Chemical Society Reviews*, 40(2):1059–1080, 2011.

[16] GN Greaves and S Sen. Inorganic glasses, glass-forming liquids and amorphizing solids. *Advances in Physics*, 56(1):1–166, 2007.

[17] C Austen Angell. Formation of glasses from liquids and biopolymers. *Science*, 267(5206):1924, 1995.

[18] R Böhmer, CA Angell, R Richert, and A Blumen. Disorder effects on relaxational processes. *Springer-Verlag, Berlin*, page 11, 1994.

[19] William Houlder Zachariasen. The atomic arrangement in glass. *Journal of the American Chemical Society*, 54(10):3841–3851, 1932.

[20] B Vessal, G Neville Greaves, PT Marten, Alan V Chadwick, R Mole, and Susan Houde-Walter. Cation microsegregation and ionic mobility in mixed alkali glasses. 1992.

[21] Byeongwon Park, Hong Li, and L René Corrales. Molecular dynamics simulation of la 2 o 3–na 2 o–sio 2 glasses. i. the structural role of la 3+ cations. *Journal of non-crystalline solids*, 297(2):220–238, 2002.

[22] GN Greaves. Exafs and the structure of glass. *Journal of Non-Crystalline Solids*, 71(1):203–217, 1985.

[23] CT Moynihan, NS Saad, DC Tran, and AV Lesikar. Mixed-alkali effect in the dilute foreign-alkali region. failure of the strong electrolyte/cationic interaction model. *Journal of the American Ceramic Society*, 63(7-8):458–464, 1980.

[24] RJ Hemley, AP Jephcoat, HK Mao, LC Ming, and MH Manghnani. Pressure-induced amorphization of crystalline silica. *Nature*, 334(6177):52–54, 1988.

[25] Berni J Alder and TE Wainwright. Studies in molecular dynamics. i. general method. *The Journal of Chemical Physics*, 31(2):459–466, 1959.

[26] David A Fletcher, Robert F McMeeking, and Donald Parkin. The united kingdom chemical database service. *Journal of Chemical Information and Computer Sciences*, 36(4):746–749, 1996.

[27] Loup Verlet. Computer" experiments" on classical fluids. i. thermodynamical properties of lennard-jones molecules. *Physical review*, 159(1):98, 1967.

[28] G Dahlquist and A Bjork. Numerical methods, 573, 1974.

[29] Simon Duane, Anthony D Kennedy, Brian J Pendleton, and Duncan Roweth. Hybrid monte carlo. *Physics letters B*, 195(2):216–222, 1987.

[30] James C Phillips, Rosemary Braun, Wei Wang, James Gumbart, Emad Tajkhorshid, Elizabeth Villa, Christophe Chipot, Robert D Skeel, Laxmikant Kale, and Klaus Schulten. Scalable molecular dynamics with namd. *Journal of computational chemistry*, 26(16):1781–1802, 2005.

[31] Paul Peter Ewald. Die berechnung optischer und elektrostatischer gitterpotentiale. *Annalen der Physik*, 369(3):253–287, 1921.

[32] Herman JC Berendsen, JPM van Postma, Wilfred F van Gunsteren, ARHJ DiNola, and JR Haak. Molecular dynamics with coupling to an external bath. *The Journal of chemical physics*, 81(8):3684–3690, 1984.

[33] Llewellyn H Thomas. The calculation of atomic fields. In *Mathematical Proceedings of the Cambridge Philosophical Society*, volume 23, pages 542–548. Cambridge Univ Press, 1927.

[34] Enrico Fermi. Un metodo statistico per la determinazione di alcune priorieta dell'atome. *Rend. Accad. Naz. Lincei*, 6(602-607):32, 1927.

[35] Jean-Pierre Hansen and Ian R McDonald. *Theory of simple liquids*. Elsevier, 1990.

[36] JM Dickey and Arthur Paskin. Computer simulation of the lattice dynamics of solids. *Physical Review*, 188(3):1407, 1969.

[37] P Kapitza. Viscosity of liquid helium below the l-point. *Nature*, 141(3558):74, 1938.

[38] S Chakraborty. Diffusion in silicate melts. *Reviews in Mineralogy and Geochemistry*, 32(1):411–503, 1995.

[39] Linus Pauling. The principles determining the structure of complex ionic crystals. *Journal of the american chemical society*, 51(4):1010–1026, 1929.

[40] GN Greaves, A Fontaine, P Lagarde, D Raoux, and SJ Gurman. Local structure of silicate glasses. *Nature*, 293:611–616, 1981.

[41] GN Greaves. Exafs, glass structure and diffusion. *Philosophical Magazine B*, 60(6):793–800, 1989.

[42] A Meyer, J Horbach, W Kob, F Kargl, and H Schober. Channel formation and intermediate range order in sodium silicate melts and glasses. *Physical review letters*, 93(2):027801, 2004.

[43] F Kargl and A Meyer. Na-relaxation and intermediate range structure in sodium–potassium silicate melts. *Chemical Geology*, 256(3):278–285, 2008.

[44] Walter Loewenstein. The distribution of aluminum in the tetrahedra of silicates and aluminates. *American Mineralogist*, 39(1-2):92–96, 1954.

[45] Ilian T Todorov, William Smith, Kostya Trachenko, and Martin T Dove. Dl_poly_3: new dimensions in molecular dynamics simulations via massive parallelism. *Journal of Materials Chemistry*, 16(20):1911–1918, 2006.

[46] GJ Kramer, NP Farragher, BWH Van Beest, and RA Van Santen. Interatomic force fields for silicas, aluminophosphates, and zeolites: Derivation based on ab initio calculations. *Physical Review B*, 43(6):5068, 1991.

[47] Jincheng Du. Molecular dynamics simulations of the structure and properties of low silica yttrium aluminosilicate glasses. *Journal of the American Ceramic Society*, 92(1):87–95, 2009.

[48] Jincheng Du and L René Corrales. Compositional dependence of the first sharp diffraction peaks in alkali silicate glasses: A molecular dynamics study. *Journal of non-crystalline solids*, 352(30):3255–3269, 2006.

[49] Theodor Hahn and MJ Buerger. The detailed structure of nepheline, kna3al4si4o16. *Zeitschrift für Kristallographie-Crystalline Materials*, 106(1-6):308–338, 1954.

[50] S Torquato. Effect of dimensionality on the continuum percolation of overlapping hyperspheres and hypercubes. *The Journal of chemical physics*, 136(5):054106, 2012.

[51] Charles Le Losq and Daniel R Neuville. Effect of the na/k mixing on the structure and the rheology of tectosilicate silica-rich melts. *Chemical Geology*, 346:57–71, 2013.

[52] JC Mikkelsen and FL Galeener. Thermal equilibration of raman active defects in vitreous silica. *Journal of Non-Crystalline Solids*, 37(1):71–84, 1980.

[53] Stephen A Moggach, Thomas D Bennett, and Anthony K Cheetham. The effect of pressure on zif-8: Increasing pore size with pressure and the formation of a high-pressure phase at 1.47 gpa. *Angewandte Chemie*, 121(38):7221–7223, 2009.

[54] Inmaculada Peral and Jorge Íñiguez. Amorphization induced by pressure: results for zeolites and general implications. *Physical review letters*, 97(22):225502, 2006.

[55] LB Vessal, M Leslie, and CRA Catlow. Molecular dynamics simulation of silica glass. *Molecular Simulation*, 3(1-3):123–136, 1989.

[56] Zhongqiao Hu, Liling Zhang, and Jianwen Jiang. Development of a force field for zeolitic imidazolate framework-8 with structural flexibility. *The Journal of chemical physics*, 136(24):244703, 2012.

[57] Thomas D Bennett, Jin-Chong Tan, Yuanzheng Yue, Emma Baxter, Caterina Ducati, Nick J Terrill, Hamish H-M Yeung, Zhongfu Zhou, Wenlin Chen, Sebastian Henke, et al. Hybrid glasses from strong and fragile metal-organic framework liquids. *Nature communications*, 6, 2015.

[58] Karena W Chapman, Gregory J Halder, and Peter J Chupas. Pressure-induced amorphization and porosity modification in a metal- organic framework. *Journal of the American Chemical Society*, 131(48):17546–17547, 2009.

[59] S Goedecker, M Teter, and Jürg Hutter. Separable dual-space gaussian pseudopotentials. *Physical Review B*, 54(3):1703, 1996.

[60] C Hartwigsen, Sephen Gœdecker, and Jürg Hutter. Relativistic separable dual-space gaussian pseudopotentials from h to rn. *Physical Review B*, 58(7):3641, 1998.

[61] George Neville Greaves, AL Greer, RS Lakes, and T Rouxel. Poisson's ratio and modern materials. *Nature materials*, 10(11):823–837, 2011.

[62] Paul F McMillan, Mark Wilson, Martin C Wilding, Dominik Daisenberger, Mohamed Mezouar, and G Neville Greaves. Polyamorphism and liquid–liquid phase transitions: challenges for experiment and theorythis paper is presented as a contribution to the conference on 'current challenges in liquid and glass science'held in abingdon, uk, january 10–12, 2007 in honour of spencer howells. *Journal of Physics: Condensed Matter*, 19(41):415101, 2007.

[63] Yue Hu, Hossein Kazemian, Sohrab Rohani, Yining Huang, and Yang Song. In situ high pressure study of zif-8 by ftir spectroscopy. *Chemical Communications*, 47(47):12694–12696, 2011.

[64] Gayatri Kumari, Kolleboyina Jayaramulu, Tapas Kumar Maji, and Chandrabhas Narayana. Temperature induced structural transformations and gas adsorption in the zeolitic imidazolate framework zif-8: A raman study. *The Journal of Physical Chemistry A*, 117(43):11006–11012, 2013.

[65] Wulf Depmeier. The sodalite family–a simple but versatile framework structure. *Reviews in mineralogy and geochemistry*, 57(1):203–240, 2005.

[66] DM Teter, GV Gibbs, MB Boisen Jr, DC Allan, and MP Teter. First-principles study of several hypothetical silica framework structures. *Physical Review B*, 52(11):8064, 1995.

[67] R Astala, Scott M Auerbach, and PA Monson. Density functional theory study of silica zeolite structures: Stabilities and mechanical properties of sod, lta, cha, mor, and mfi. *The Journal of Physical Chemistry B*, 108(26):9208–9215, 2004.

[68] MB Boisen Jr and GV Gibbs. A modeling of the structure and compressibility of quartz with a molecular potential and its transferability to cristobalite and coesite. *Physics and Chemistry of Minerals*, 20(2):123–135, 1993.

[69] Chang-sheng Zha, Russell J Hemley, Ho-kwang Mao, Thomas S Duffy, and Charles Meade. Acoustic velocities and refractive index of sio 2 glass to 57.5 gpa by brillouin scattering. *Physical Review B*, 50(18):13105, 1994.

[70] Magali Benoit and Walter Kob. The vibrational dynamics of vitreous silica: Classical force fields vs. first principles. *EPL (Europhysics Letters)*, 60(2):269, 2002.

[71] U Buchenau, M Prager, N Nücker, AJ Dianoux, N Ahmad, and WA Phillips. Low-frequency modes in vitreous silica. *Physical Review B*, 34(8):5665, 1986.

[72] Melville S Green. Markoff random processes and the statistical mechanics of time-dependent phenomena. ii. irreversible processes in fluids. *The Journal of Chemical Physics*, 22(3):398–413, 1954.

[73] Ryogo Kubo. Statistical-mechanical theory of irreversible processes. i. general theory and simple applications to magnetic and conduction problems. *Journal of the Physical Society of Japan*, 12(6):570–586, 1957.